JAGIELLONIAN UNIVERSITY
INSTITUTE OF PHYSICS
DEPARTMENT OF ATOMIC OPTICS

Metastability Exchange Optical Pumping (MEOP) of ^{3}He in situ

Guilhem Collier

PhD thesis conducted under the direction of
prof. Dr hab. Tomasz Dohnalik

KRAKÓW, 2011

Dedicated to my parents

Metastability Exchange Optical Pumping (MEOP) of ^{3}He in situ

Abstract: Polarized helium-3 is used as a contrast agent for lungs magnetic resonance imaging that has recently reached the pre-clinical applications. One method to hyperpolarize ^{3}He is the metastability exchange optical pumping (MEOP). Optical pumping is performed in standard conditions at low pressure (≈ 1 mbar) and low magnetic field (≈ 1 Gauss). In this work, the complete update of a low field polarizer dedicated to small animal lungs imaging is presented. The implementation of a new 10 W laser, new peristaltic compressor and others components resulted in a production of 3-4 scc/min for a polarization between 30 to 40%. Images of rat lungs made with better resolution and a new dynamic radial sequence are presented as a validation of the system. Since few years, MEOP has also been studied at higher pressures and higher magnetic fields in small sealed cells. It showed that, thanks to hyperfine decoupling effect induced by high magnetic field, it was also possible to efficiently polarize at higher pressure (67 mbar). Experiments done at 4.7 and 1.5 T are reported in this work. The first ones show a benefic (higher polarization values) and a negative effect (lower production rates) of the magnetic field. The seconds highlight the advantage of using an annular beam shape of the laser that matches the distribution of 2^3S state atoms at higher pressure. Nuclear polarization values of 66.4% at 32 mbar and 31% at 267 mbar were obtained in 20 mL sealed cells and a 10 times increase in the production rate compare to best standard conditions. These promising results were the first motivation for building a high-field polarizer working inside MRI scanner in hospital. The design and the construction of such a polarizer are described in detail in the last part of the dissertation. The polarizer produces hyperpolarize ^{3}He at 30-40% with a 4 times higher flow than the low field polarizer (10-15 scc/min). The first good quality human lungs images made in Poland with healthy volunteers are the main result of this work.

Keywords: Helium-3, MEOP, metastability exchange, hyperpolarized gas, polarizer, optical pumping, nuclear polarization, 1083 nm, hyperfine decoupling, MRI, lungs imaging

Acknowledgements:

I acknowledge my supervisor prof. dr hab. Tomasz Dohnalik for having given to me the opportunity to do my PhD in his group. He has always been available, helpful and very kind to me during these 4 years.

I also would like to express my gratitude to Pierre-Jean Nacher from which I learned a lot about MEOP and without whom most of the results presented in this work would have never been achieved.

Mateusz Suchanek is also someone who helped me to get acquainted with the polarizer at the beginning and whose good mood and motivation for doing experiments even with almost nothing always gave me strength to leave my computer for the laboratory.

I would never thank enough Anna Nikiel for her kindness and considerable assistance and help in any aspect of everyday life.

Genevieve Tastevin deserves also a great respect from me for the considerable work made on the MEOP model elaboration and the fruitful exchanges during data analysis of the systematic studies performed at high magnetic field.

Katarzyna Cieslar, although she had already left the group before my arrival, always answered to my questions related to MRI and collaborating with her on small animal lungs imaging was a pleasure.

I want to address a special thank to the workshop of our department in which Józef Flaga and Stanislaw Pajka work. I don’t remember any situation during these 4 years where I have left their office without getting any answer or problem solved even when the polish language was not yet that easy for me. I wish to Józef Flaga a good retirement with his bees.

I need to thank Tadeusz Palasz for his knowledge in electronics, laser and his help during the construction of the polarizers gas handling systems.

Zbigniew Olejniczak deserves my gratitude for his fruitful advices.

I also want to pay homage to the people involved at some points in the construction of these polarizers and with who I collaborated sometimes closely: Piotr Klocek, Jerzy Olejniczak, Roman Wiertek, Pan Napiórkowski.

I acknowledge my colleagues, Bartosz Glowacz and Anna Wojna and wish them to finish their PhD in the best conditions.

I had the great opportunity to travel to different partners during this Marie Curie fellowship and I would like to thank Xavier Maître from Orsay group for having welcoming me for more than one month in his lab.

Julien Rivoire provided me intensive course on Siemens scanner and without him, I would have never been able to program sequences and get them work in such a short period.

And finally I would like to thank all the great people from Poland or

elsewhere that I met in Krakow and who made these four years unforgettable for me. Among them, I am specially thinking about my partner Dorota.

Contents

List of Symbols

A_i	i = 1 to 6, symbols of the six 2^3S_1 magnetic sublevels
a_i	Relative populations of sublevels A_i
A	Absorptance of the probe laser
A^+	Absorbance of the probe σ^+ component
A^-	Absorbance of the probe σ^- component
α	Fine structure constant
B	Magnetic field
B_j	j = 1 to 18, symbols of the eighteen 2^3P magnetic sublevels
b_i	Relative populations of sublevels B_i
$1/\beta$	Spin temperature
C	Fluid conductance
c	Speed of light
D	Free diffusion coefficient of ^{3}He
d_t	Diameter of the capillary
Δ	Doppler width
η	Photon efficiency
f	Oscillator strength of the 2^3S-2^3P transition
F	Total angular momentum
g_I	Nucleus g-factor
g_L	Electron orbital g-factor
g_S	Electron spin g-factor
$\Gamma'/2$	Total damping rate of the optical coherence between the 2^3S and 2^3P states
Γ_b	Build-up rate of nuclear polarization at the beginning of OP
Γ_{decay}	Decay rate of nuclear polarization in the presence of rf discharge and the absence of optical pumping
Γ_{dd}	Nuclear spin relaxation rate due to the magnetic dipole interaction between the ^{3}He nuclear spins
Γ_{dis}	Nuclear spin relaxation rate due to collisions with ions in the discharge plasma
Γ_e	ME collision rate for 1^1S atoms
Γ_L	Laser-induced relaxation rate
Γ_g	Intrinsic ground state relaxation rate
Γ_{mag}	Nuclear spin relaxation rate due to magnetic field inhomogeneities
Γ_w	Wall relaxation of spin polarized ^{3}He
γ	Radiative decay rate of the 2^3P state
γ_0	Gyromagnetic ratio of ^{3}He

γ_e	ME collision rate for 2^3S_1 atoms
γ_r^S	Relaxation rate in the 2^3S state
γ_r^P	Relaxation rate in the 2^3P state
γ_{ij}	Optical transition rate from A_i to B_j sublevels
H	Total Hamiltonian of the system
H_f	Hamiltonian describing the fine interaction
H_{hf}	Hamiltonian describing the hyperfine interaction
H_z	Hamiltonian describing the Zeeman interaction
$\hbar$	Planck constant
I	Nuclear spin angular momentum
I_{las}	Light intensity
I_{Voigt}	Voigt integral (see definitions in equations (3.17))
J	Total electronic angular momentum
$<J^*_z>$	Mean z-component of electronic angular momentum in 2^3S
k_B	Boltzmann constant
L	Orbital angular momentum
L_c	Capillary length
L_{cell}	Length of the OP cell
L_{path}	distance done by the probe laser in the OP cell
λ	Mean free path
M	Nuclear polarization of the ground state
M_m	Molar mass
M^*	Nuclear polarization of the metastable state
M_{ap}	Apparent nuclear polarization of the baseline-corrected peak heights analysis
m_{at}	Atomic mass
M_{eq}	Steady state polarization
ME	Metastability exchange
m_e	Mass of the electron
m_F	Total angular momentum quantum number
m_I	Nuclear angular momentum quantum number
m_L	Total electronic angular momentum quantum number
m_S	Angular momentum quantum number associated to the spin of the electron
μ	Nuclear magnetic moment of ^3He
$N^\uparrow$	Number densities of the nuclear spin states $m_I = + ½$
$N^\downarrow$	Number densities of the nuclear spin states $m_I = - ½$
N_g	Total number density of the ground state
n_m	Total number density of the metastable state 2^3S_1
$\tilde{n}$	Prefactor of the formula for n_m calculation (see definition in equation (3.12))
ω	Light angular frequency
ω_{ij}	Angular frequency of the $A_i \rightarrow B_j$ atomic transition

P	Pressure
P_{abs}	Power absorptance of the probe at the beginning of OP when M = 0
P_{las}	Laser power
Q	Flow of polarized ^{3}He expressed in scc/min
R	Production rate
R_e	Number of Reynolds
R_8	Ratio of relative absorbance signals r^+ and r^- for the C_8 transition
r_{theo}	Theoretical ratio of the two transition matrix elements $T_{2\rightarrow9}$ and $T_{1\rightarrow10}$ of the σ^+ probe doublet at high magnetic field
r^i_{exp}	Experimental ratio of the ith recorded doublet during multiscan acquisition. This ratio is calculated by the Fortran program: fitpeaksHib.exe
r^+	Relative σ^+ absorbance signal
r^-	Relative σ^- absorbance signal
ρ	Mass density
S	Electronic spin angular momentum
$S^i_{m_F}$	Peak amplitude of the $T_{2\rightarrow9}$ (m_F = -1/2) or $T_{1\rightarrow10}$ (m_F = -3/2) transition of the ith recorded doublet during multiscan acquisition
σ^+	Right-handed circular light polarization parallel to the magnetic field
σ^-	Left-handed circular light polarization parallel to the magnetic field
σ_e	Cross section of the ME collisions
T_1	Longitudinal relaxation time of nuclear polarization
t_{ac}	Acquisition time for a MRI sequence
t^i_{av}	Average time of the ith recorded doublet during multiscan acquisition
T_{decay}	Time constant of the exponential decay of the polarization in systematic studies after switching off the pump laser
$t^i_{m_F}$	Time of recorded $S^i_{m_F}$ peak amplitude
TR	Repetition time for a MRI sequence
T_{ra}	Transmission of the probe laser
t_B	Build-up time constant of polarization during OP
T_{ij}	2^3S - 2^3P transition matrix element between A_i and B_j
$\theta_\pm$	Mixing parameters of electronic and nuclear angular momenta
u	Average velocity of helium during constant flow
u_{ij}	Frequency detuning of laser light (see equation (3.13))
V	Volume
υ	Atomic velocity of colliding atom
$\overline{\upsilon}$	Average velocity
w_G	FWHM of Doppler width
w_L	FWHM of Lorentz width
z_0	Characteristic absorption length of the probe laser

Abbreviations

COPD	Chronic Obstructive Pulmonary Disease
CT	Computed tomography
DBR	Distributed Bragg Reflector
FT	Fourier Transformation
FID	Free Induction Decay
FLASH	Fast Low Angle Shot
FWHM	Full Width at Half Maximum
FOV	Field Of View
GHS	Gas Handling System
HP	Hyperpolarized
LIA	Lock-In Amplifier
ME	Metastability Exchange
MEOP	Metastability Exchange Optical Pumping
MRI	Magnetic Resonance Imaging
NMR	Nuclear Magnetic Resonance
OP	Optical Pumping
PBS	Polarizing Beam Splitter
PET	Positron Emission Tomography
rf	Radio frequency
scc	Standard Cubic Centimeter. It corresponds to the number of atoms included in one mL (cubic centimeter) for a gas at atmospheric pressure (1013.25 mbar) and normal temperature (273.15 K).
SEOP	Spin Exchange Optical Pumping
SNR	Signal to Noise Ratio
SPGR	Spoiled Recalled Gradient Acquisition
ST	Spin Temperature
TMP	Turbomolecular Pump
US	Ultra Sound

Introduction

The main principle of Optical Pumping (OP) was first theoretically suggested in 1950 by Alfred Kastler [Kas50] and consists in changing the distribution of atoms among the energy sublevels of the ground state by resonant absorption of polarized light. A little more than ten years later [Col63, Wal62], the first experiments demonstrating the possibility to hyperpolarize a stable isotope of helium, ^{3}He, were successfully performed and a new technique was discovered: Metastability Exchange Optical Pumping (MEOP). In this method, optical pumping is firstly performed on the metastable state 2^3S of ^{3}He atoms and in a second step, the nuclear orientation is transferred through metastability exchange collisions to the ground state.

So far, MEOP has exclusively been applied to ^{3}He and polarization near 90 % could be obtained for pressures on the order of 1 mbar [Bat05, Bat11b, Big92, Gen93]. Recent laser developments dedicated to optical pumping [Gen03, Mue01, Tas04] and ameliorations of experimental conditions [Gen93, Sto96, Wol04] increased the efficiency of the method. Nevertheless, limitations in the higher pressure domain ($P > 10$ mbar) have never been fully understood and different methods of non-relaxing compression of ^{3}He had to be developed [And05, Bat05, Eck92, Gen01, Hus05, Nac99, Wol04] to obtain polarized gas samples on the order of atmospheric pressure, which is required in most applications.

In fact hyperpolarized ^{3}He has many applications in many branches of physics. In nuclear physics it is being used for neutrons spin filters [Bat05, Bec98, Hut11, Iof11, Jon00, Sur97] and as polarized target to study the neutron structure [Ant93, Bec99, Mey94]. It can also be used for NMR measurements of gas diffusion in porous media [Tas05], for building magnetometer [Mor97] and for magnetic resonance imaging (MRI) of the lungs in animals [Via99] and in humans [Bee04]. Since the first images of excised rat lungs in 1994 in Nature [Alb94] and in-vivo human lungs shortly after [Ebe96, Fal96], the technique has made such significant progress that it is now providing unsurpassed images of gas ventilation and has demonstrated great potential in wide a range of chest diseases such as asthma [Dri07], cystic fibrosis [Ban10, Kou05], COPD [Swi05], lung transplant [Gas03] and lung cancer [Ire07].

Interest in lungs MRI imaging using hyperpolarized (HP) gas has become more and more important since nowadays lung diseases are a huge cause of mortality in the world. For example chronic obstructive pulmonary disease (COPD) is the fourth leading cause of chronic morbidity and mortality in the United States and is projected to rank fifth in 2020 in burden of disease worldwide [Rab07] whereas cystic fibrosis is the most frequent lethal genetic pediatric disease in the Caucasian population [Ban10]. Translation of HP-^{3}He MRI into the clinical area has been accomplished [Kau09] but it still remains an emerging technique compared to the other modalities such as Chest Radiography, lung scintigraphy, Positron Emission Tomography (PET) and of course the standard modality that is chest Computed Tomography (CT). Nevertheless, the main advantage of MRI compare to CT is that it is a non-invasive technique, which is very convenient when it comes to repeatedly examining for asthma or cystic fibrosis in children.

^{3}He is not the only gas that can be optically polarized. It is possible to obtain hyperpolarized ^{3}He and ^{129}Xe with a different technique called Spin Exchange Optical Pumping (SEOP). This was also discovered in the early 60's [Bou60]. In SEOP, optical pumping is firstly performed on an alkali atom and the polarization is then transferred to the ground state of the noble gas atoms via spin-exchange collisions [Wal97, Wal11]. The main advantage of SEOP is that optical pumping is performed directly at several bars and thus does not require any additional compression but the transfer of polarization to ^{3}He or ^{129}Xe is a long process that can take several hours and polarization is usually lower than in MEOP [Wal97]. It is good to notice though a recent significant work [Her08] where a ^{129}Xe production of 0.3 L/hour was reached with 64 % polarization. Due to its lower gyromagnetic ratio, ^{129}Xe has a lower signal in lung imaging compare to ^{3}He but it is much cheaper and its solubility to the blood is well suited for functionality and perfusion studies. That is why ^{129}Xe stays a good alternative and can also be a complement to MEOP. A recent study on imaging a mixture of xenon and helium [Aco04] proved the complementary of both methods.

The present work will focus on the possible improvements of MEOP and the implementation of new polarizers in the clinical environment for lungs MRI. Apart from the recent redhibitory price of ^{3}He, due to a global shortage [Cho09], the main drawback of MEOP is the compression required afterwards. It leads to design dedicated compressors that are in any case responsible for an additional relaxation. Moreover, it also limits the production rate that can be achieved in a compact polarizer suited for a clinical environment. That is why it is of great importance for MEOP to understand its current limitations at relatively high pressures ($P > 10$ mbar) and to try to find experimental conditions for which the compression step would be eased. Preliminary works of MEOP in high field ($B > 0.1$ T) showed dramatic increase of steady state polarization and extended the range of operating pressure to several tens of mbar [Nac02, Abb04, Abb05b, Nik07]. Systematic studies of MEOP were then conducted in collaboration between Krakow and Kastler Brossel Laboratory (LKB) in Paris to explore influence of laser shape and intensity, magnetic field, ^{3}He pumping pressure and density of metastable state [Nik10]. A comprehensive update of the theoretical model of MEOP has even recently been extended to higher pressures domain although discrepancies still exist between experimental results and theoretical values of steady state polarization due to an unknown relaxation during OP [Bat11a].

The motivation of this work is to concretely transpose these promising results obtained in sealed cells to a new high field polarizer that would work directly inside the most commonly used scanner at 1.5 T. The manuscript is organized in the following way:

- In the first chapter, the theory and basic aspects of MEOP required for a good comprehension of this work will be described.
- In the second part, a complete update of a low field polarizer is presented leading to some lung imaging applications both in voluntary human and small animals.
- My contribution to the systematic studies performed in high field (1.5 and 4.7 T) with sealed cells is summarized in the third chapter.
- A last, preliminary tests and construction of a high field polarizer is described and discussed.

Before going on, I would like to introduce the notion of absorption that will be used in the following of this dissertation. When a laser is tuned to an atomic transition of ^{3}He, a part of the laser light is absorbed and a part is going out of the cell containing the gas. The quantity remaining that can be monitored on a photodiode is called transmittance T. A = 1 – T, is called here the absorptance and the useful quantity for polarization and density of metastable state measurement is the absorbance: - ln (T). In this dissertation, most of the figures show a quantity called absorption, which is obtained by dividing the signal after demodulation by a lock-in amplifier by the integrated transmittance (see § 3.2.2). This quantity is directly proportional to the absorbance and this is the one used for the measurement.

Chapter 1

MEOP Theory:

In this chapter the main features of MEOP will be described in order to ease the comprehension of the physical processes involved. After a reminder of the basic notion of polarization, the 3-steps general scheme of MEOP will be presented together with the main results obtained in the standard conditions, which means low magnetic field (~ 10 G) and low pressure (~ 1 mbar). The main factors limiting the process at higher pressure will be recalled and the effects of magnetic field on ^{3}He levels structure and MEOP results summarized. Finally, important parameters used in the different MEOP models proposed these last years will be introduced before their utilization in the results part of chapter 3.

1.1. Concept of polarization:

The ground state 1^1S_0 of ^{3}He is a singlet state with an orbital angular momentum L = 0. Its total electronic angular moment J is then also null and its total angular momentum is purely nuclear F = I = ½. 1^1S_0 is composed of two sublevels characterized by their quantum number m_I = ± ½ and the nuclear polarization M is defined as the difference of populations between these two nuclear spin states:

$$M = \frac{N^{\uparrow} - N^{\downarrow}}{N^{\uparrow} + N^{\downarrow}} = \frac{N^{\uparrow} - N^{\downarrow}}{N_g} \tag{1.1}$$

where $N^{\uparrow}$ and $N^{\downarrow}$ are respectively the number densities of nuclear spin states m_I = ½ and m_I = - ½ and N_g is the total number density of ground state atoms.

In a magnetic field B, at normal room temperature and in the thermodynamic equilibrium, number densities follow the Boltzmann distribution and M can be written:

$$M = \frac{\exp(\frac{2\mu B}{k_B T}) - 1}{\exp(\frac{2\mu B}{k_B T}) + 1} \approx \frac{\mu B}{k_B T} \approx \frac{\gamma_0 \hbar B}{2 k_B T} \tag{1.2}$$

with nuclear magnetic moment μ, Boltzmann constant k_B, gyromagnetic ratio of ^{3}He γ_0 and Planck constant $\hbar$. At T = 300 K and B = 1.5 T, this gives a polarization of 3.89×10^{-6}. In conventional MRI, the signal is coming from the magnetization of protons in H_2O contained inside tissues. The polarization of water in the same field and temperature conditions is only 1.31 times larger due to a difference in gyromagnetic ratio. The reason why it is possible to image protons in the case of water and not for ^{3}He is due to the difference of density. In pure water and at 37 °C, proton density is around 6.7×10^{22} atoms/cm^3 when it is only 2.3×10^{19} for a gas at 1 atm [Con97]. It results in a difference of signal by a factor of approximately 3800. Some attempts to perform MRI with thermally polarized ^{3}He have been done at 2.35 T in small animals [Kob99] but the quality of picture, duration of apnea and sequence make it not feasible in human.

With optical pumping, SEOP or MEOP for the concern of this work, polarization on the order of 30 to 80 % can be achieved and the difference of density is easily compensated by the resulting magnetization.

1.2. MEOP in standard conditions:

The main idea of optical pumping by exchange of metastability was found in early 60's [Col63] and does not depend of the field and pressure conditions it is being performed. It is schematically described on Fig. 1.1 and its principle can be divided in three steps.

- Direct pumping from the ground state like in SEOP with rubidium atoms is not possible due to a too high energy difference (≈ 20 eV) and forbidden transition between 1^1S_0 and 2^3S_1 states. That is why a weak radio frequency (rf) discharge is sustained inside the optical pumping cell to populate higher states of ^{3}He. After a radiative cascade, a small fraction of the atoms is falling into the metastable state 2^3S_1 that is playing the role of ground state for OP. Due to the angular momentum conservation rule and the forbidden transition between triplet and singlet states, it cannot decay via photon emission. Its lifetime is thus only limited by some collision process (see § 1.5.4). The number density n_m of atoms in the metastable state is much lower than the ground state number density N_g. Typically n_m/N_g = 1 ppm.
- In a second step, OP is performed with a circularly polarized light tuned at 1083 nm on one of the available transition between 2^3S_1 and 2^3P sublevels. From the 2^3P state, an isotropic radiative de-excitation happens and atoms come back to the metastable state (Fig. 1.2). After few cycles of optical pumping, the population densities of low hyperfine quantum number m_F in the case of σ^+, are depleted in

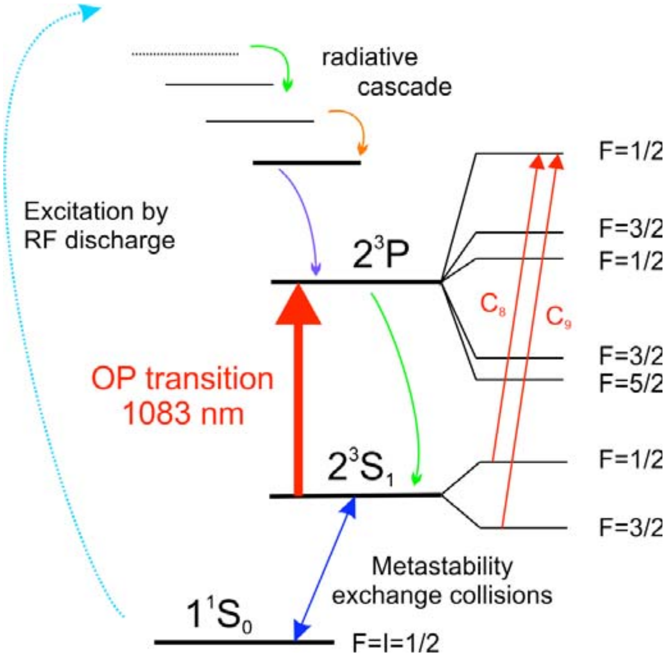

Fig. 1.1. Scheme of metastability exchange optical pumping (see text). The singlet ground state 1^1S_0 and the two first triplet state 2^3S (metastable state) and 2^3P are the ones involved in the process. They have been subdivided into hyperfine sublevels prior to their total angular momentum number F. The most efficient transition used in low field C_8 and C_9 are displayed.

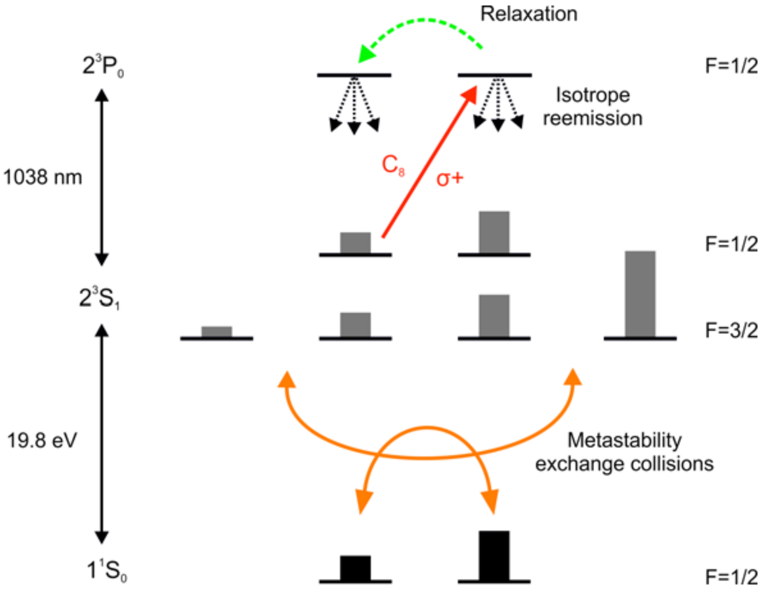

Fig. 1.2. Population diagram of the 1^1S_0, 2^3S_1 and 2^3P_1 and main processes involved during an OP performed on C_8. The other sublevels of 2^3P are not presented for the sake of clarity. The black and grey bars represent the modified density of populations in the sublevels due to OP.

favor to those of high m_F and the optical orientation of the electronic angular momentum is enforced. Due to an efficient hyperfine coupling between the electrons and the nucleus of the 2^3S_1 atoms, this electronic optical orientation induces nuclear orientation as well.

- The last step occurs during metastability exchange (ME) collisions between ground state atoms and nuclearly polarized metastable atoms ${}^3He^*_\uparrow$. ME collisions are fast processes where the colliding 2^3S and 1^1S^0 atoms just exchange electronic excitations with no change of nuclear orientations. They induce no global loss of angular momentum. The result of this last step is a net transfer of nuclear orientation from the metastable state to the much more populated ground state.

$$ {}^3He + {}^3He^*_\uparrow \rightarrow {}^3He^* + {}^3He_\uparrow \tag{1.3}$$

The hyperfine level structure involved in the optical pumping transition at 1083 nm have been already completely described in [Nac85] and [Cou02] and is displayed in Fig. 1.3. We will keep the same notation of sublevels as in [Cou02] and recall the main results. The metastable state 2^3S_1 has two hyperfine levels F = 3/2 and F = 1/2 well resolved in low field (split by 6.74 GHz) and six sublevels A_1 to A_6 (population density a_1 to a_6) labeled by their increasing order of energy. These levels can be written using a decoupled basis states $\left|m_S, m_I\right\rangle$.

$$\begin{aligned}
A_1 &= \left|-1,-\right\rangle \\
A_2 &= \cos\theta_-\left|-1,+\right\rangle + \sin\theta_-\left|0,-\right\rangle \\
A_3 &= \cos\theta_+\left|0,+\right\rangle + \sin\theta_+\left|1,-\right\rangle \\
A_4 &= \left|1,+\right\rangle \\
A_5 &= \cos\theta_-\left|0,-\right\rangle - \sin\theta_-\left|-1,+\right\rangle \\
A_6 &= \cos\theta_+\left|1,-\right\rangle - \sin\theta_+\left|0,+\right\rangle
\end{aligned} \tag{1.4}$$

A_1 and A_4 are pure states whereas the other ones involve large mixing parameters θ_+ and θ_- (see appendix of [Cou02]). At zero magnetic field, maximal mixing of electronic and nuclear momenta occurs with $\sin^2\theta_+ = 1/3$ and $\sin^2\theta_- = 2/3$. The metastable state 2^3P has two hyperfine levels F = 1/2, two levels F = 3/2 and one level F = 5/2. This gives 18 sublevels B_1 to B_{18} (population density b_1 to b_{18}).

An absorption spectrum at 1 mT generated by a Fortran program made by Pierre-Jean Nacher from Kastler Brossel laboratory is displayed on Fig 1.4. The spectrum is computed from the amplitudes of the transition matrix elements T_{ij} of the fine and hyperfine line components assuming pure Doppler broadening. The transition probabilities T_{ij} of all components of the 1083 nm line were evaluated in [Cou02] and can be found in more detail in appendix A of [Bat11b]. At this field, differences between absorption spectrum of left-handed σ^- and right-handed σ^+ circularly polarized light parallel to the magnetic field axis are negligible. Nine components are allowed between 2^3S and 2^3P levels but due to Doppler

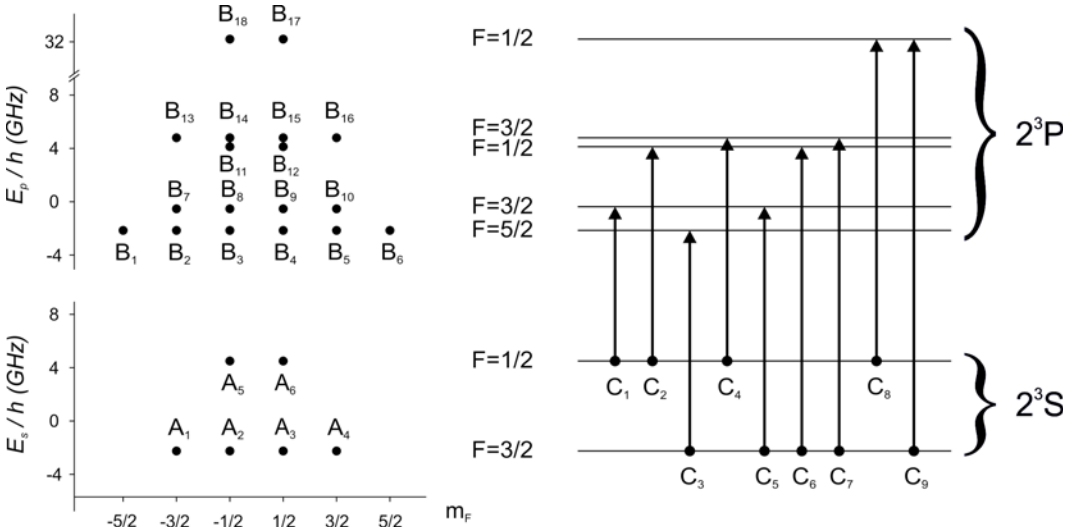

Fig. 1.3. Hyperfine structure of the 2^3S and 2^3P states. Left: diagram showing energetic positions at low magnetic field (≈ 1 mT) of the 6 and 18 sublevels of 2^3S and 2^3P states respectively as a function of their angular momentum projection m_F. Right: visualization of the nine allowed optical transitions at 1083 nm.

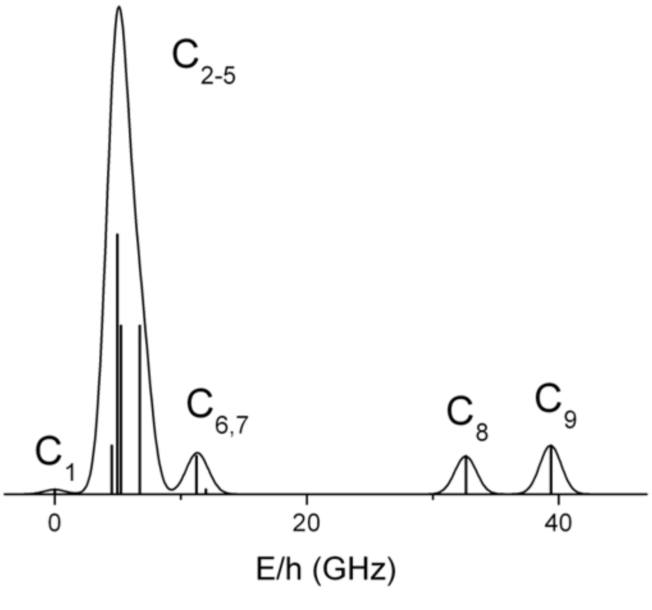

Fig. 1.4. 1083 nm absorption spectrum at low magnetic field. The spectrum was computed assuming a pure Doppler broadening width of 1.2 GHz at 300K. The vertical bars represent the transition matrix elements T_{ij} of the available components. Optical transition frequencies are referenced to that of the C_1 line in zero magnetic field like in [Cou02].

broadening only 5 peaks are resolved in the absorption spectrum. The well-resolve C_8 and C_9 components are the most commonly used transitions for MEOP at low field in pure ^{3}He gas. The choice depends on the ^{3}He pressure. For pressure lower than 1 mbar, the laser is tuned on C_8 and for pressure of the order of 1 mbar or higher, pumping on C_9 gives a higher steady state polarization.

Nuclear polarizations of the order of 0.8 are obtained [Bat05, Big92, Gen93] thanks to the recent development of dedicated laser [Gen03, Tas04]. Efficiency and production rates depend mainly of the laser and the rf discharge intensities [Gen93, Wol04].

1.3. Pressure limitation of MEOP:

When polarizing ^{3}He at higher pressure (P > 5 mbar), the steady state nuclear polarization obtained is much lower (see Fig. 1.5). Values decrease progressively with pressure and polarization is only about a few percents at 40 mbar and higher. This tendency could be mainly due to two collision processes. The ionizing Penning collisions described in equation (1.5) shorten the lifetime of atoms in the 2^3S metastable state [Sch69]. Thus, this non linear process could affect the efficiency of MEOP by inducing an unfavorable ratio between metastable and ground state atoms.

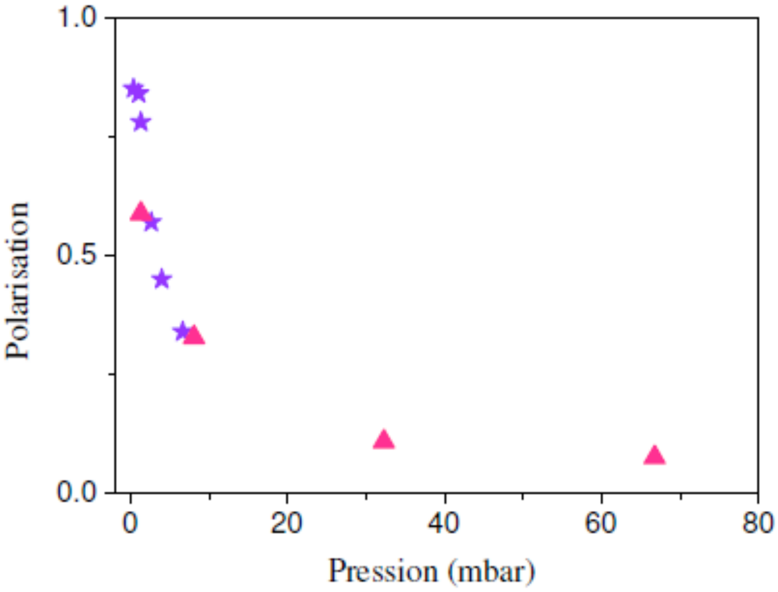

Fig. 1.5. Steady-state polarization obtained by MEOP at low magnetic field as a function of the ^{3}He pressure. This figure is taken from § 1.3.2 of Marie Abboud's thesis [Abb05a]. Stars: results published in [Gen03] from OP on C_9 with a 4.5 W laser. Triangles: Abboud's results with a 2 W laser tuned on C_9. A more detailed and recent figure can be found in Marion Batz thesis ([Bat11b], Fig 6.49). The results are similar and show the same tendency.

$$He^{*} + He^{*} \rightarrow He + He^{+} + e^{-} \quad (1.5)$$

In addition, an increase in frequency of 3-body collisions with conversion into a metastable helium molecule (equation (1.6)) could also be an additional relaxation channel occurring at higher pressure. The rate of creation of these molecules is enhanced with a P^2 dependence and their diffusion lifetime linearly increase with P [Nac02]. Collisions between $^3He_2$ molecules and polarized atoms could be similar as metastability exchange collisions and nuclear angular momentum could be dissipated in the numerous rotational states of the molecule by spin-orbit coupling (see § 2.2.2 of [Cou01]).

$$He^{*} + 2He \rightarrow He_2^{*} + He \quad (1.6)$$

Recent works have confirmed the existence of these molecules [Glo11] but their role to this additional relaxation has not been precisely defined yet.

1.4. Magnetic field dependence of MEOP:

Detailed calculations were performed in [Cou02] to obtain dependence of ^{3}He atomic structure with magnetic field. It is determined by finding the eigenvalues of the total Hamiltonian H of the system:

$$H = H_f + H_{hf} + H_z \quad (1.7)$$

where H_f and H_{hf} are the Hamiltonians describing fine and hyperfine interactions and where H_z is the Hamiltonian taking into account the interaction between electronic and nuclear spins with magnetic field. If μ_B and μ_N are the Bohr and nuclear magneton, g_L, g_S and g_I the g-factors of electronic orbital, electronic spin and nuclear spin angular momentum L, S and I respectively, H_{hf} can be written:

$$H_z = \left[\mu_B (g_L L + g_S S) + \mu_N g_I I\right] \cdot B \quad (1.8)$$

In standard conditions ($B \approx 1$ mT), the magnetic field is used only for preventing a fast relaxation of nuclear polarization and has negligible influence on the structure of the atomic states. Interactions between electronic and nuclear spins with magnetic field are much lower than fine and hyperfine interactions. That is why σ^+ and σ^- spectrum look similar and a special care has to be taken to obtain pure circular polarization of laser light during optical pumping. But when Zeeman energy exceeds the fine and hyperfine structure energy scales, the structure of 2^3S and 2^3P levels and transitions between them are deeply modified.

On Fig 1.6, the evolution of eigenvalues of the total Hamiltonian characterizing the energies of the Zeeman sublevels of 2^3S and 2^3P eigenstates are represented as a function of magnetic field until 4.7 T. At this field strength, only a weak state mixing remains in the 2^3S metastable state. For $B > 1$ T, the

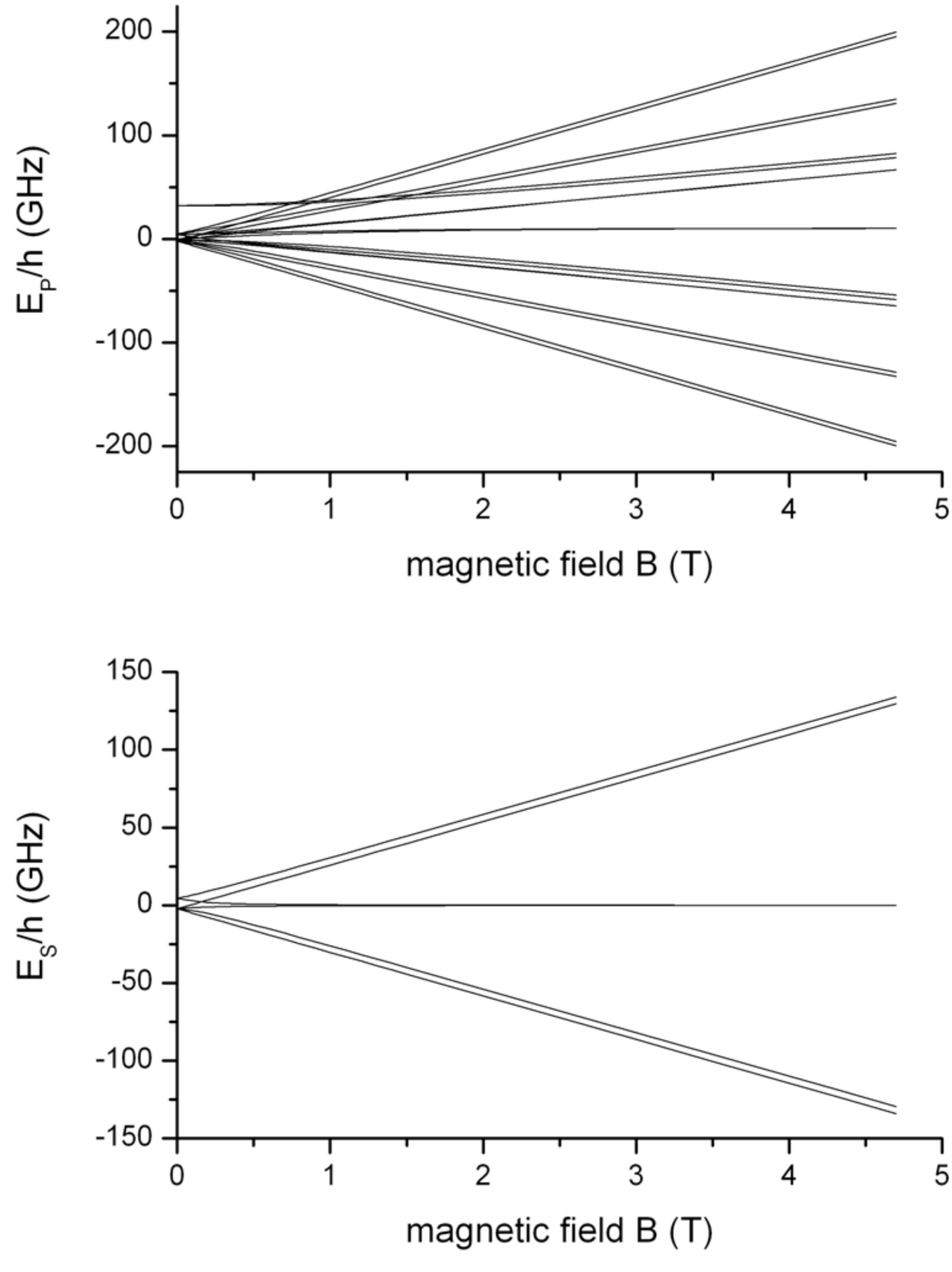

Fig. 1.6. Energy splits between sublevels in the metastable state 2^3S_1 (bottom) and first excited state 2^3P (top) as a function of the magnetic field B. The sublevels A_1 to A_6 and B_1 to B_{18} are labeled by their increasing order of energy and their energetic positions are defined so that their sum equals 0.

following approximation can be made [Abb05a]:

$$\sin^2\theta_{\pm} \approx 0.012/B^2 \tag{1.9}$$

Variations of sinθ_+ and sinθ_- are displayed in Fig 1.7. When increasing the magnetic field, a first energy crossing of eigenstates appears between A_4 and A_5 at 0.1602 T (Fig 1.6) and at higher B, A_5 becomes the eigenstate $|1,+\rangle$ with $m_F = 3/2$. The Hamiltonian in excited state 2^3P cannot be resolved analytically due to its complexity but a numerical computation was made in [Cou02] and a precision of the order of MHz for sublevels energies was obtained.

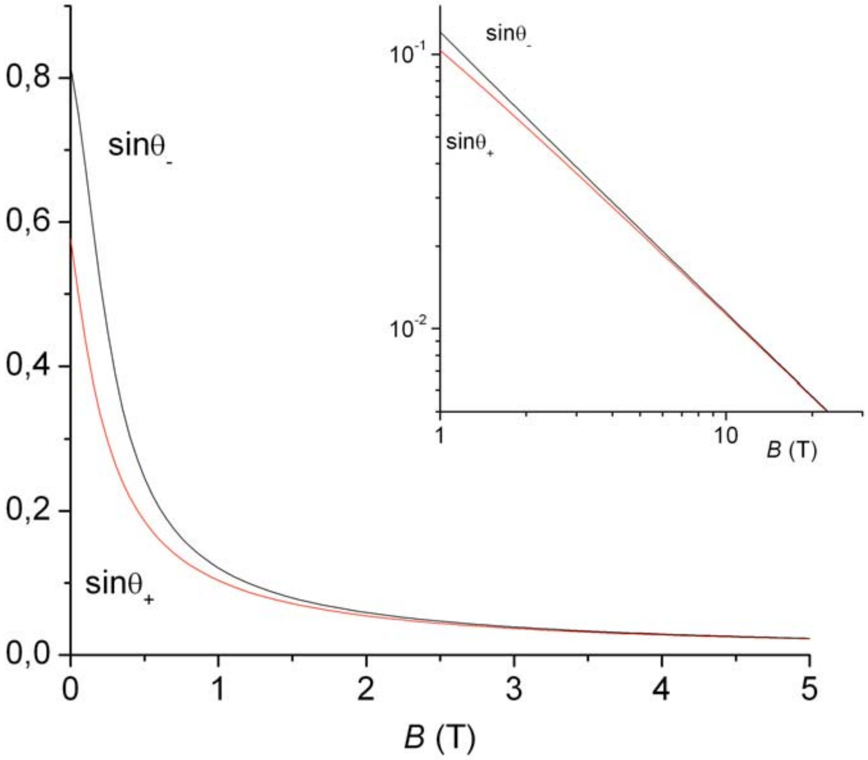

Fig. 1.7. Mixing parameters of electronic and nuclear angular momenta sinθ_+ and sinθ_- as a function of the magnetic field. At 1.5 T, sinθ_+ = 0.07128 and sinθ_- = 0.07697.

All Zeeman sublevels for the magnetic fields B = 1.5 and 4.7 T at which experiments were made are displayed on figure 1.8. In the 2^3S state, the six Zeeman sublevels are organized in three pairs of states in which the level energy is mostly determined by the common dominant value of m_S. The same phenomenon is present for the 2^3P state with 9 pairs of sublevels whose energies are also mostly determined by m_S and m_L. At high magnetic field, F is thus not the good quantum number anymore. However, the relation $m_F = m_L + m_I + m_S$ being always fulfilled, m_F is kept for the representation in Fig. 1.8.

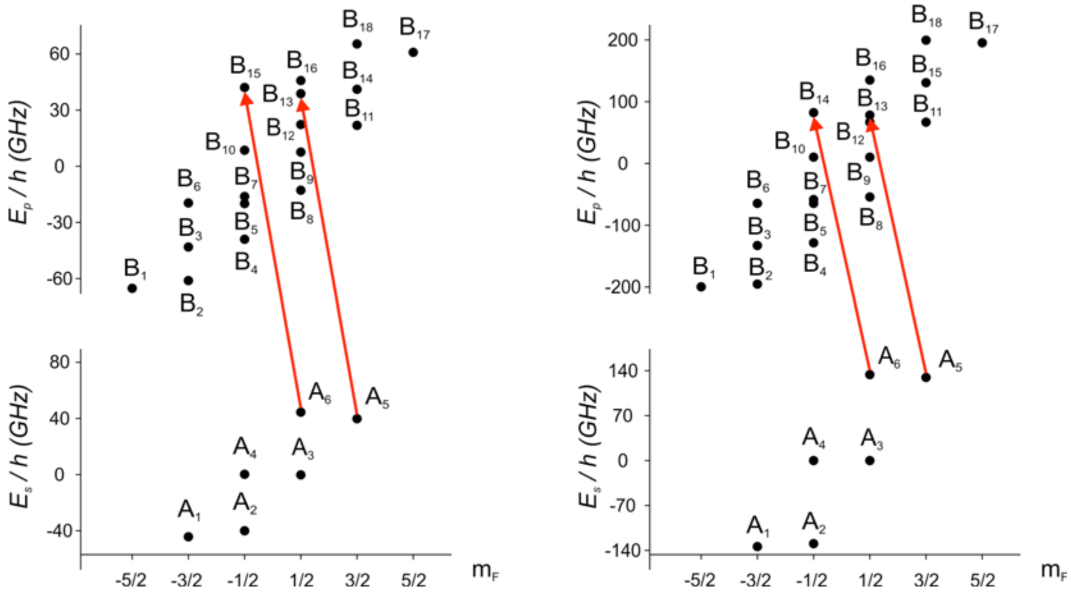

Fig. 1.8. Energies E_s/h and E_p/h in frequency units and angular momentum m_F of the sublevels of the 2^3S and 2^3P states of ^{3}He at 1.5 T (left) and 4.7 T (right). Energy references and state labeling are identical to those of [Cou02]. Arrows represent the two unresolved transitions of the most efficient component for MEOP in high field: f^{2-}.

Similar absorption spectra as Fig 1.4 and also generated by the same Fortran program are presented in Fig 1.9 for 1.5 T and 4.7 T. Spectra are different depending on the considered light polarization (σ^+, σ^- or pi). This is a first benefic effect of hyperfine decoupling in high field, as it is not anymore mandatory to use an extremely pure circular polarization of the light due to a well resolved spectrum between σ^+ and σ^- polarizations. These spectra extend other 170 GHz at 1.5 T and 530 GHz at 4.7 T compared to 40 GHz at low field. The optical transition energies E/h and intensities T_{ij} at 1.5 T are given in tables 2.1 and 2.2 of [Abb05a]. For a given polarization, the spectrum is composed of six main components appearing in one pair ($f^{2\pm}$) and one quartet ($f^{4\pm}$) unresolved at room temperature (Fig 1.9).

The first experiments of MEOP at high magnetic field were performed in 2001 [Cou01] at 0.1 T and already showed an increase by a factor of two in the achievable polarization at 40 mbar. After the first attempts to explain this improvement in high field [Nac02], the experiments were reproduced and polarization improved at 1.5 T [Abb04] and f^{2-} component was found to be giving the highest polarization [Abb05b]. The optical detection was then updated [Suc07] and results were extended to 2 T at 67 mbar for a nuclear polarization of 51 % [Nik07]. The main reason of this spectacular improvement is the hyperfine decoupling effect happening at high magnetic field. In standard conditions, a strong entanglement of electronic and nuclear spin states (hyperfine coupling) occurs. In other words, a transfer of orientation between nuclear to electronic spin and orbital is eased and this orientation can be lost through emission of polarized

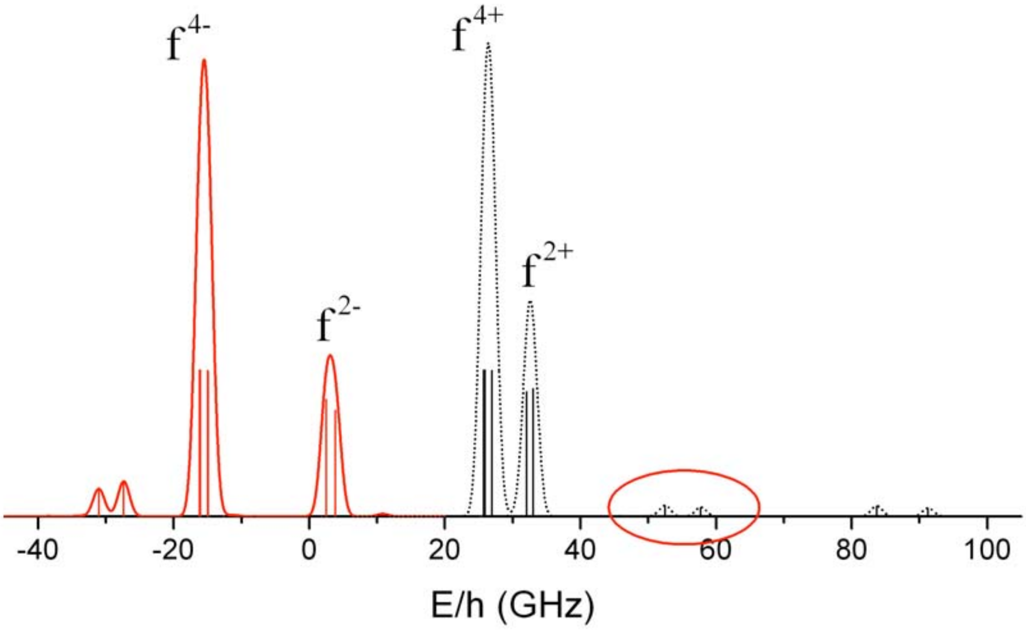

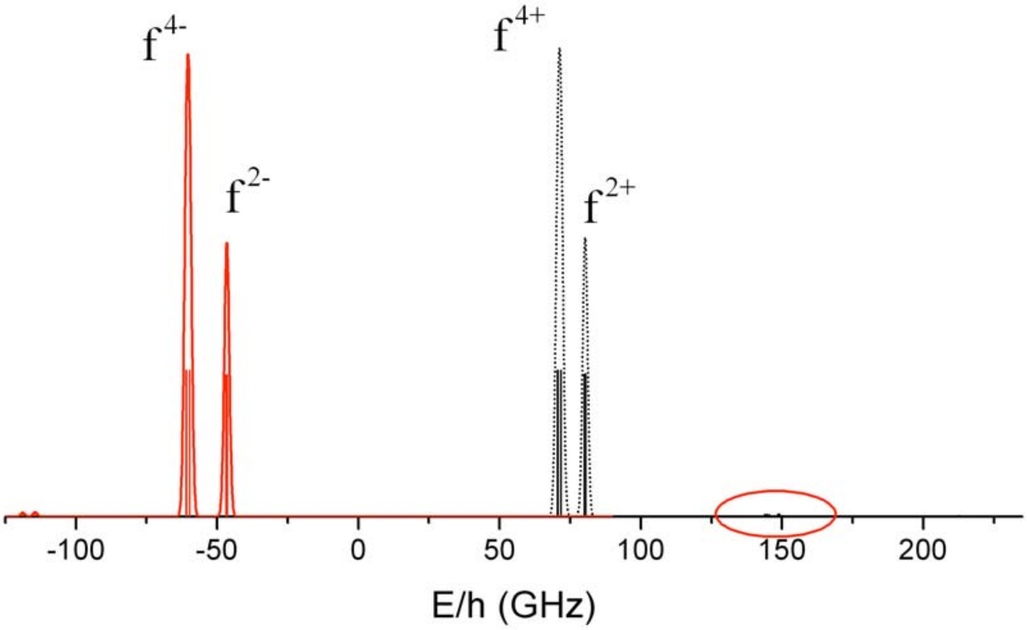

Fig. 1.9. Main parts of the 1083 nm absorption spectra at 1.5 T (top) and 4.7 T (bottom) for the circular light polarization σ^+ (dotted line) and σ^- (solid line). Spectra were computed assuming a pure Doppler broadening width of 1.2 GHz at 300K. The vertical bars represent the transition matrix elements T_{ij} of the available components. Optical transition frequencies are referenced to that of the C_1 line in zero magnetic field like in [Cou02]. Probe lines used for pumping experiment on f^{2-} (see chapter 3) are highlighted.

light in the higher excited states created by the rf discharge. Therefore, due to decoupling effect at higher magnetic field, angular momentum loss is reduced in the cascade and subsequent reduced nuclear relaxation is expected to yield higher optical pumping performances.

The reduced loss of nuclear polarization in the presence of the discharge is experimentally clearly visible at high magnetic field in the decreasing of the polarization decay rate in the absence of optical pumping: Γ_{decay}. A negative aspect of hyperfine decoupling is that the polarization build up time t_B is also longer in high field. Thus the efficiency of MEOP at low pressure can be actually lower than in low field. To characterize the efficiency of MEOP, the following volume-independent production rate is defined:

$$R = \frac{M \times P}{t_B} \tag{1.10}$$

where M is the nuclear polarization and P the pressure. If the production rate is lower at low pressure compare to low field, the fact that it is possible to reach high polarizations at higher pressures makes MEOP much more efficient in high field than in standard conditions. The weaker coupling in high field is then compensated by the increase of Metastability Exchange (ME) collisions rate at high pressures. In the best standard conditions, the maximum production rate is around 0.16 mbar/s when it was found to be 0.32 mbar/s at 67 mbar and 2 T [Nik07]. In other terms, it means that the same production of magnetization can be reached in a two times lower volume at high magnetic field. This is a major concern knowing that the production facility in Mainz [Bat05, Wol04] uses 36 L of optical pumping cell in a 4 m long system. In practice, the two main values someone has to maximize when trying to build a polarizer is the polarization M and the production rate R and the rest of this work will focus in particular on these two parameters.

1.5. Main features of MEOP model:

The aim of this section is not to establish a new model of MEOP. This work is already performed elsewhere by Pierre-Jean Nacher's group in Kastler Brossel Laboratory. A first detailed model was given in [Nac85] for low field and low pressure conditions that could predict the value of nuclear polarization achievable for different laser intensities and discharge conditions. This model is based on rate equations of the populations of the 2^3S and 2^3P states and takes into account the effects of OP, ME collisions and relaxations. This model was extended to ^3He-^4He gas mixtures in [Lar91] and after the first successful experiments of MEOP at 0.1 T [Cou01], the levels energies were derived [Cou02] and effects due to higher magnetic field discussed [Abb05a]. Recently, a comprehensive improvement of this model that tries to implement the advances in MEOP at high laser powers, high gas pressures and high magnetic field is being tested [Bat11a, Bat11b].

Unfortunately, some discrepancies between computed M values and experimental results are systematically obtained and lead to the conclusion that an additional laser induced relaxation should be taken into consideration. Details can be found in the given references and will not be discussed here. In this section, only the main features of MEOP and corresponding crude equations will be recalled in order to illustrate and give an easier understanding to the reader of the processes involved.

1.5.1. Metastability Exchange collisions

The relative populations of sublevels A_i (i = 1 to 6) in the metastable state are written a_i such that $\sum_{i=1}^{6} a_i = 1$. If n_m is the total density of atoms in 2^3S state, the density of atoms in A_i is then $n_m a_i$. For convenience, the relative populations b_j in the 2^3P state are defined so that the density of atoms in B_j sublevels is $n_m b_j$. As described already earlier in equation (1.3), negligible depolarization occurs during metastable exchange collisions and the colliding atoms only exchange their electronic excitation. In the formalism using the density matrices introduced in [Nac85], and if we define the ME collisions rate $\gamma_e = N_g \overline{\sigma_e \upsilon}$ (cross section of ME collisions: σ_e, atomic velocity of colliding atom: υ and where $\overline{\sigma_e \upsilon}$ represents the average over the thermal distribution of the velocity), the time evolution of the relative populations can be written:

$$\left.\frac{da_i}{dt}\right|_{ME} = \gamma_e \left(\sum_{k=1}^{6} a_k (E_{ik} + MF_{ik}) - a_i \right) \qquad (1.11)$$

The field dependent matrices E and F involve the mixing parameter $\theta_\pm$ and can be found in appendix of [Cou02]. γ_e is proportional to the pressure of ^{3}He and was found to be $3.75 \times 10^6 s^{-1} mbar^{-1}$ in [Dup71] at room temperature. The increase at higher pressures compensates for the decreasing values inside the matrices due to decoupling at high magnetic field. The ME collisions lead to a common evolution of the relative populations a_i and the nuclear polarization M described by the following equation:

$$\left.\frac{dM}{dt}\right|_{ME} = \Gamma_e \left(M^* - M \right) \qquad (1.12)$$

where M^* is the nuclear polarization in the metastable state and Γ_e the ME collision rate for atoms in the ground state 1^1S ($\Gamma_e = \frac{N_g}{n_m} \gamma_e$).

1.5.2. Spin temperature distribution

The notion of spin temperature distribution plays an important role under the conditions that OP and relaxation processes have negligible effect on populations. In practice, these conditions are fulfilled in absence of optical pumping. In these circumstances, it was proposed in [And59] that the relative populations of the 2^3S sublevels should follow a Boltzmann-like distribution in angular momentum. This is valid at all field strengths and in pure ^{3}He as well as in ^{3}He-^{4}He gas mixtures. Under the effect of ME collisions, the nuclear polarization M enforces a spin temperature distribution of the 2^3S sublevels populations. Defining the temperature distribution 1/β by:

$$e^{\beta}=\frac{N^{\uparrow}}{N^{\downarrow}}=\frac{1+M}{1-M} \tag{1.13}$$

it can be written that [Cou02]:

$$a_i=\frac{e^{\beta\cdot m_F}}{e^{3\beta/2}+2e^{\beta/2}+2e^{-\beta/2}+e^{-3\beta/2}} \tag{1.14}$$

The notion of spin temperature (ST) is the basis of the optical detection of polarization methods implemented in the experiments of § 2.1.7 and chapter 3. The ST distribution is affected by optical pumping and relaxation processes.

1.5.3. Optical pumping

In the case of monochromatic excitation between A_i and B_j sublevels the average over Maxwell velocities distribution at thermal equilibrium of optical transition rate was given in [Cou02]:

$$\overline{\gamma_{ij}}=\frac{4\pi\alpha f}{m_e\omega\Gamma'}\frac{T_{ij}I_{las}}{\overline{\upsilon}\sqrt{\pi}}\int_{-\infty}^{\infty}\frac{(\Gamma'/2)^2e^{-(\upsilon/\overline{\upsilon})^2}\,d\upsilon}{(\Gamma'/2)^2+\left(\omega-\omega_{ij}-\omega_{ij}\upsilon/c\right)^2} \tag{1.15}$$

where α is the fine structure constant, f the oscillator strength of the transition, m_e the electron mass, I_{las} the light intensity, υ the atom velocity, $\overline{\upsilon}$ the average speed, ω and ω_{ij} the angular frequencies of the light and of the atomic transition, $\Gamma'/2$ the total damping rate and c the speed of light.

The effect of OP can then be modeled by the following equations:

$$\left.\frac{da_i}{dt}\right|_{OP}=\gamma\sum_{j=1}^{18}T_{ij}b_j+\sum_{j=1}^{18}\gamma_{ij}\left(b_j-a_i\right) \tag{1.16}$$

$$\left.\frac{db_j}{dt}\right|_{OP}=-\gamma b_j+\sum_{i=1}^{6}\gamma_{ij}\left(a_i-b_j\right) \tag{1.17}$$

where $\gamma=1.022\times10^7 s^{-1}$ is the radiative decay of the 2^3P state [Bat11a]. The first parts of equations (1.16) and (1.17) describe the contribution of spontaneous emission of light from 2^3P sublevels when the second part represents the competing effects between the 2^3S atoms excitation and stimulated emission by 2^3P atoms. In the case of a broadband laser and at low pressure ($\Gamma'/2 << 2\pi\Delta$, Δ: Doppler width) the integral in equation (1.15) can be easily computed and result is given in equation (2.16) of [Bat11b]. It can be used in practice for the single component C_8 in low field and at low pressure. At high magnetic field, MEOP is performed on multi-components absorption lines $f^{2\pm}$ or $f^{4\pm}$ and thus gives higher optical rate. As it will be discussed in chapter 3, collisional broadening has to be taken into account at higher pressures and the computation of $\overline{\gamma_{ij}}$ yields Voigt profiles that significantly differ from the Gaussian Doppler profile.

1.5.4. Relaxation processes

Relaxation refers to all the processes that couple the atoms of the various Zeeman sublevels. For simplicity, the contributions of all processes involved are taking into account in the [Bat11b] model through simple rate equations that correspond to uniform redistributions with a single relaxation rate for each state: γ_r^S, γ_r^P and Γ_g for 2^3S, 2^3P and 1^1S states respectively. The different relaxations are briefly described below.

As evoked earlier in § 1.2, atoms in 2^3S state cannot decay via photon emission due to the angular momentum conservation rule. It can, in practice, only decay through collision processes. Two of them, the ionizing Penning and 3-body collisions were already described in equations (1.5) and (1.6). Additional collision processes during ^{3}He diffusion to the cell wall and excitation quenching by gas impurities are responsible for an angular momentum loss [Nac02]. Equation (1.18) summarizes all these effects using the single rate γ_r^S that tends to equalize all the relative populations of 2^3S sublevels to 1/6. Depending on pressure, cell dimensions, gas purity, etc., γ_r^S is typically of order 10^3 s^{-1} [Bat11a].

$$\left.\frac{da_i}{dt}\right|_r = \gamma_r^S\left(\frac{1}{6} - a_i\right) \tag{1.18}$$

A similar equation (1.19) is used for the 2^3P state but the J-changing collisions occur at a much higher rate. γ_r^P is of the order 10^7 s^{-1} at low pressure (1 mbar) and 10^9 s^{-1} at 50 mbar [Abb05a]. In this relatively high pressures regime, γ_r^P is much higher than the radiative decay in the 2^3P state γ, and a total redistribution of the atoms in the B_j sublevels can be assumed.

$$\left.\frac{db_j}{dt}\right|_r = \gamma_r^P\left(\frac{1}{18}\sum_{k=1}^{18} b_k - b_j\right) \tag{1.19}$$

Finally, the relaxation in the ground state in the presence of discharge is modeled as follow:

$$\left.\frac{dM}{dt}\right|_r = -\Gamma_g M \tag{1.20}$$

with:

$$\Gamma_g = \Gamma_{dis} + \Gamma_{dd} + \Gamma_w + \Gamma_{mag} \tag{1.21}$$

Different processes are taken into account. Γ_{dd} is the nuclear spin relaxation rate due to the magnetic dipole interaction between the ^{3}He nuclear spins. The decay time was found to be several years [New93] and Γ_{dd} can be easily neglected. Γ_{w} is the wall relaxation rate of spin polarized ^{3}He. It was also already fully studied in [Den06, Sch06a, Sch06b] and can be neglected too in the conditions of the systematic studies of chapter 3. Γ_{mag} represents the relaxation rate due to magnetic field inhomogeneities. A special care has to be taken to limit the field gradients in the location of the OP cell. In the case of the low field polarizer of chapter 2, numerical computation was done to reduce the inhomogeneities (see § 2.1.1). For systematic studies (chapter 3) and high field polarizer (chapter 4) the field maps of the scanners (made for MRI experiments) are much better than the homogeneity required for OP. Finally, Γ_{dis} is the nuclear spin relaxation rate due to the presence of the plasma discharge (collisions with ions, etc).

The generic equation of the variation of nuclear polarization can be thus be written as the sum of the ME collisions and relaxations contributions:

$$\frac{dM}{dt} = \Gamma_e\left(M^* - M\right) - \Gamma_g M \tag{1.22}$$

Practically, it will be shown in the results part of chapter 3 that a laser induced relaxation is missing in this crude model, and that it is responsible of the main relaxation during OP experiments.

Chapter 2

Low Field Polarizer:

As seen in previous section, in the most favorable conditions, usually obtained in sealed cells, the achieved nuclear polarization can exceed 85 % [Bat05, Bat11b, Gen93]. In practice, achieving a good polarization level and production rate of ^{3}He usable in MRI is far from being straightforward. Regarding MEOP technique, different strategies of gas production have been established. A global and central massive production has been chosen in Mainz [Bat05, Wol04], coupled with long storage relaxation systems for shipment to different partners [Bee03]. This group has designed an advanced bulky polarizer reaching an efficient gas production of 20 or 60 scc/min* for a nuclear polarization of 75 % and 60 % respectively, depending on the ^{3}He working pressure inside the optical pumping cells. This polarizer has even been successfully duplicated in Laue-Langevin institute in Grenoble for the production of spin-filter cells for polarizing neutron beams [And05]. The disadvantages however, are the high price due to the non-magnetic titanium alloy piston compressor [Bec94] driven by a hydraulic system, the big size of the polarizer containing five optical pumping cells of 2.4 m for a total volume of 36 L, as well as difficulties in adjusting to user demands with regard to gas shipment over large distances.

Another approach is to design smaller polarizers, easy to handle, storable and placed close to the MRI system or other facilities for on-site production. The key element of such polarizer is always the compressor responsible mainly for the depolarization during compression to atmospheric pressure or higher inside the storage cell. Some attempts to build a more compact polarizer for ^{3}He-^{4}He gas mixtures working with a modified diaphragm pump [Gen01] and an aluminium piston compressor [Hus05] have been successful in the United States. A table-top polarizer have also been designed in Paris using a peristaltic compressor [Nac99] and duplicated in Orsay [Cho03]. In general, such compact polarizer has the

*scc is an acronym for Standard Cubic Centimeter, corresponding to the number of atoms included in one mL (cubic centimeter) for a gas at atmospheric pressure and normal temperature.

advantage of having lower cost and less constrains but usually only allows to reach lower polarization level and much lower throughput than the system in Mainz. Typically, the polarized ^{3}He production rate in all these systems is around 3 to 5 scc/min for a polarization varying between 30 to 55 %.

A similar table-top polarizer was designed few years ago by our group [Suc05a] but had typical throughput of only 0.4 scc/min for an estimated final polarization of only few percents when extracted into a syringe for small animal lungs MRI. During the 2 first years of this thesis, the polarizer underwent an extensive upgrade, whose main novelties are a new 10W laser and a new design of a peristaltic compressor. In this chapter, all the different modifications of the polarizer are described as well as the MRI facilities used for our applications. At last, results are presented and discussed.

2.1. Upgrade of the polarizer:

In Fig. 2.1 the general design of our table-top polarizer is schematically described and a picture of it is presented in Fig. 2.2. The main framework and the coils frame were copied from the Protlab polarizer made in Paris [Cho03, Nac99].

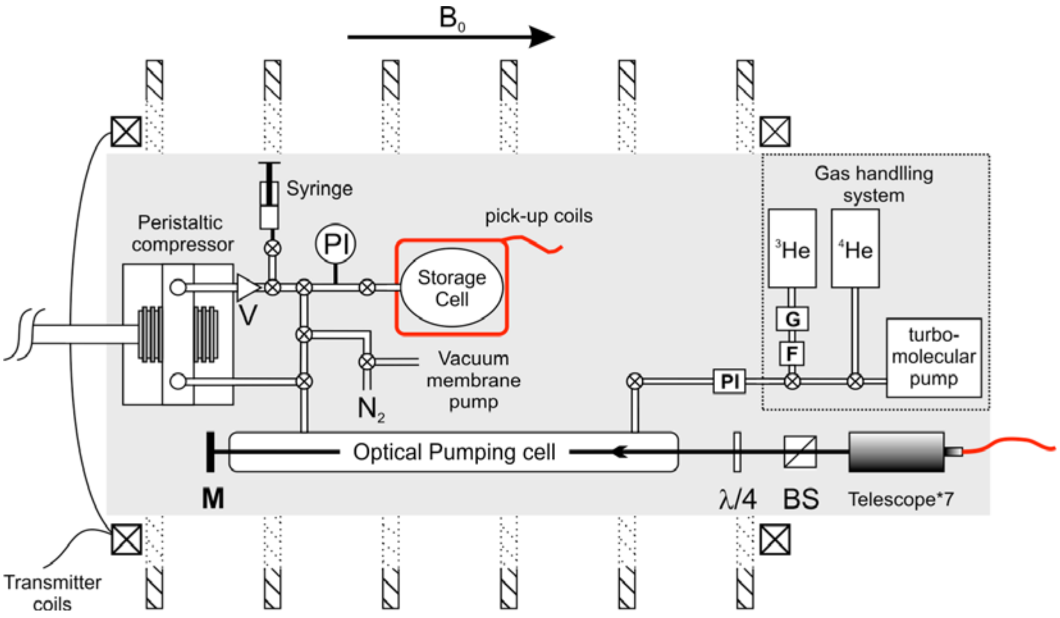

Fig. 2.1. Scheme of the table top-polarizer (see text). Six coils (cross section) produce a homogeneous magnetic field. A gas handling system located under a 12 mm aluminium plate (G: Getter, F: 50 µm filter) delivers gas to the optical pumping cell where it is being polarized by a laser tuned at 1083nm (BS: Polarizing beam splitter). A mirror (M) is reflecting back the beam to double the efficiency. The gas is then compressed to a storage cell (V: one-way valve, PI: Pressure sensor) with a peristaltic compressor. The same gas can be compressed a second time to atmospheric pressure inside a syringe for rat lung experiment using a bypass between input and output of the compressor.

Fig. 2.2. Picture of the low field polarizer.

The supporting frame is made of fifteen 6 cm width square aluminium profiles inside which a main 12 mm thick aluminium plate is mounted. Wheels were added on the bottom of the framework, allowing an easy handling and transportation of the polarizer. The gas handling system was built inside a separate rectangular cuboid frame made of aluminium and plexiglas. MEOP efficiency being strongly dependent of the gas purity, a particular care was taken to keep all the system airtight. All necessary needle valves (4172G6Y/MM by Hoke, Spartanburg, SC, USA) were helium airtight certified, and connections between the different elements were made using a 6 mm OD electropolished non-magnetic 316/316L stainless steel tube (Swagelok, Solon, Ohio, USA). The gas handling system is composed of a turbomolecular pump that can achieve a vacuum of 10^{-8} mbar and a bottle of ^{4}He for cleaning purposes of the optical pumping cell. The 1 L ^{3}He bottle at a pressure of 15 bar (Spectragases, Stewartsville, New Jersey, USA) has a purity of 99.999 % but for further cleaning, the gas passes through a PS2-GC50 SAES (Lainate, Italy) getter, and an additional mechanical porous 0.5 µm filter. A pressure sensor (24PC, Honeywell, Morristown, New Jersey, USA) was mounted at the output of it to control the pressure inside the optical pumping cell. Connection between gas handling system and the optical pumping cell is made using a flexible pipe from the CT convoluted metal tubing series and a glass metal connection (G304-4-GM3, Cajon, Solon, Ohio, USA). All the gas handling system fits inside a 40*60*90 cage that can be placed under the main plate of the polarizer. The actual dimensions of the main framework plus gas handling system are 70*160*170 and make it easily transportable to any MRI facility.

2.1.1. Guiding field

A guiding field of 16.4 Gauss is produced by 3 pairs of square coils of 20 cm side. The frame of the coils is made of 2 mm thick aluminium whose cross section has an open square shape. Grooves of the 2 inner pairs of coils have a 14 mm thickness and 22 mm for the external ones. Positions and number of turns for each coil were optimized by a Matlab program, taking into account the different filling height of the groove depending on the number of turns of a 0.8 mm diameter copper wire. To be more realistic, the filled groove was not assimilated to one loop of current but discretized into nine equally spaced loops centered around the center of the groove.

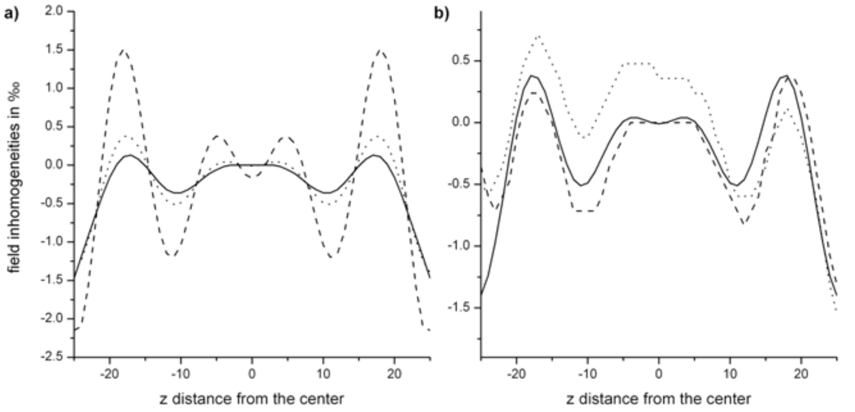

Fig. 2.3. Computation and experimental data of the magnetic guiding field deviation (1000*ΔB/B) inside the set of 6 square coils. The magnetic field is along the z direction. a) Matlab computation of our magnetic field inhomogeneities for three different distances from the symmetric axis of the square frames (solid line, dotted line and dashed line respectively 0, 3.5 and 7 cm from the axis on the diagonal direction of the square frame). b) Comparison between computed (solid line) and experimental values (dotted and dashed lines) measured with a Bartington magnetometer. The dotted line corresponds to the left side of the axis where the 48 cm long optical pumping cell is lying and the dashed line to the right side where the NMR and the 100 mL, 5 cm long storage cell is located.

An optimized configuration was found to be 85, 100 and 225 turns respectively for the 6, 19.1 and 36.8 cm distances from the center of symmetry of the system (see Fig. 2.3). The simulations were experimentally verified with a three axis MAG-03 MS fluxgate magnetometer (Bartington Instruments, Witney, Oxfordshire, United Kingdom). The power supply of the probe was home made and gave a precision of 0.1‰. The probe was mounted on a Plexiglas structure that allowed investigation of a matrix of 3.5 cm steps along transverse direction and it was manually moved with a step of 1 cm along the magnetic field direction. The experimental results gave a good agreement with the simulation and a final homogeneity of 1.5‰ was obtained in the location of a cylindrical optical pumping cell 48 cm long, 0.1‰ for a 100 mL storage cell which serves to perform the NMR measurement, and 0.6‰ for the second NMR system dedicated to a 1.1 L storage cell.

2.1.2. Laser

The 50 mW DBR diode laser was replaced by a new ytterbium 10 W fiber laser (2.1 GHz FWHM, Keopsys CUS-BT-YFL-1083-HE-100-COL, Lanion, France) with the same wavelength of 1083 nm. An APC collimator (model F220APC, Thorlabs, Newton, New Jersey, USA), coated for 1064 nm with a focus length of 11.17 mm was mounted directly on the output of the fiber. To improve efficiency of optical pumping inside the 5 cm diameter optical pumping cell, the beam was expanded by a Kepler-like telescope (magnification 7x, Eksma Optics, Vilnius, Lituania). The final FWHM of the Gaussian beam profile was 4.9 mm. The beam was circularly polarized with a 5 cm cube polarizing beamsplitter and a multiple order plate with $\lambda/4$ retardation. The beam was back-reflected by a dielectric mirror after first passage through the cell to double the efficiency.

2.1.3. Optical pumping cell

Thanks to the new guiding field, a new longer Pyrex optical pumping cell of 48 cm length, 5 cm diameter with optical windows have been implemented. Apiezon L grease was used for lubrication of input and output valves. Some 5 cm glass capillaries of 1.8 mm diameter were located at the input and output of the cell to constraint the gas flowing in one direction only and keep impurities out of the storage cell and gas handling system. The cell was located 3.5 cm off center of the coils symmetry axis.

2.1.4. Storage Cell and gas transportation

To store the polarized ^{3}He gas after compression, three different storage cells were used. A small 100 mL Pyrex cell was dedicated to short rat lung imaging experiments in our 0.088 T permanent magnet based system and optical calibration of the NMR signal. This cell was previously demagnetized in Mainz [Thi07]. Following this procedure, a longitudinal ^{3}He relaxation time of 54 min was measured by NMR. A 500 mL quartz cell with a longer decay time of 4 h was used to store larger quantities of helium for longer experiments. Thanks to a bypass system implemented between the output and the input of the peristaltic compressor (see Fig. 2.1) a portion of the gas can be compressed a second time to atmospheric pressure into a 12 mL syringe. This latter is used to transfer ^{3}He from the low field polarizer to the low-field MRI system located 10 meters away in our laboratory. Previously, polarized ^{3}He was mixed in the storage cell with a buffer gas (^{4}He or N_2) to reach a pressure higher than 1 atm and only a small amount of ^{3}He was retrieved by distending the mixture inside a plastic syringe. This new process of extracting helium avoids gas dilution and, as a result, increases the total magnetization inside the syringe by a factor of 3. Losses due to the first and the second compression inside the peristaltic compressor and also during transportation in presence of a non homogeneous magnetic-field are difficult to accurately assess but the relaxation time of ^{3}He inside the syringe in the low-field MRI system was measured to be longer than 3 min (see Fig. 2.4).

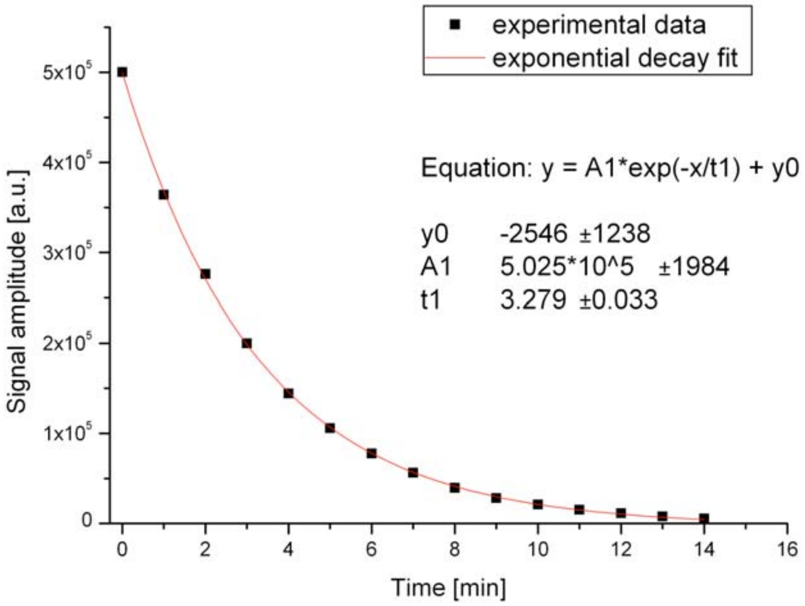

Fig. 2.4. Relaxation of magnetization inside a 12 mL polypropylene/polyethylene syringe in our 0.088T permanent magnet. Plastic syringe was used to transport polarized ^{3}He from the storage cell to the scanner and to inflate lungs of the tracheotomised rat. Time before application was reduced as much as possible and kept below 20 s, which is equivalent to a total magnetization loss lower than 10 %.

For human lung experiments, storage cells of 1.1 L volume were bought together with a magnetic transport box (Fig. 2.5) from Arbeitsgruppe Helium-3, Institut fur Physik, Universitat Mainz [Bee03, Hie10]. As it was shown in [Sch06b] that short relaxation times could be attributed to ferromagnetic contaminants, the vessels were made by Schott AG (Mainz, Germany) from a special aluminosilicate-glass containing a minimum of these paramagnetic centers and the best flask was certified to have a 150 h wall relaxation time. In practice, our gas handling system at the output of the compressor being not as clean as it is at the input of the OP cell, an additional bulk relaxation due to impurities shortened this time. The NMR measurement gave a decay time of polarization inside the cell of 6 h. To store and keep the vessels inside a magnetic homogeneous guiding field, permanent magnets produce a field of 10 Gauss and the transport box is magnetically shielded with pieces of mu-metal leading to relative gradients lower than 10^{-3}/cm. This gives a relaxation time due to gradient inhomogeneities close to 150 h at 1 bar. Once in the hospital and the preliminary calibrations on patient executed, the transport box was placed close to the end of the fringe field of the scanner. A special care was taken to have the same orientation of the fringe field of the scanner and the transport box. After opening the box, gas was extracted into a 1 L Tedlar gas sampling bag (model GST001S-0707, Jensen Inert products, Coral Springs, Florida, USA) using a similar design of the peristaltic compressor as the one used in the table-top polarizer. The sample bag was pre-filled with 100 mL of nitrogen to avoid a too fast relaxation with its inner surface during the beginning of helium compression. After a first rinse of the lungs with nitrogen, gas mixture was directly administrated to the volunteer through the sample bag. Delay between the end of ^{3}He polarization and the time of the scan was approximately 1.5 h, including 45 min of transportation.

Fig. 2.5. Transport box and vessels from Mainz Univeristy group for ^{3}He storage during journey to hospital.

2.1.5. Peristaltic compressor

To replace the peristaltic compressor borrowed from the Kastler-Brossel laboratory [Nac03], a new transparent design was developed, tested and experimentally approved (see Fig. 2.6). The transparent feature eases the diagnosis of possible problem with peristaltic tube. The compressor is build of the following fixed elements: the main body is made of polycarbonate, two Plexiglas lids with bearing shells, Plexiglas pressing bar, radiators, peristaltic tube and Plexiglas oil chamber. The rotor of the compressor is made of polyamide and rotates around a non-magnetic steel axis. The pressing polyamide rollers also rotating on non-magnetic axis play the role of the compressor's valves. The main motivation for this new design was to ease the replacement of the inner peristaltic tube. The replacement procedure was then shortened from 30 min to 15 min. To lengthen the lifetime of the tube, inorganic oil was inserted inside the compressor and two radiators were mounted on both side of the main body to dissipate the heat energy released during friction. To improve the flow circulation, a vacuum of the order of few mbar was maintained by a rotary pump inside the body of the compressor, while operating. This vacuum prevents the tube from shrinking under atmospheric pressure while compressing helium that is polarized in the optical pumping cell at 2-3 mbar. A small gas reservoir is located between the compressor and the vacuum chamber to keep the oil inside the main body. Several peristaltic tubes from Masterflex (Cole-Parmer, Vernon Hills, Illinois, USA), models C-FLEX (50 A), Pharmed BPT, Norprene (A 60 G) and BioPharm Plus silicone have been tested out of which only the first two showed satisfactory parameters to be used inside the compressor. NMR measurements on the storage cell showed that both of them gave similar and reproducible polarization levels but for mechanical considerations the Pharmed tube was chosen due to a more rigid property, allowing for a longer lifetime up to 20 h. Compressors of two different sizes were produced. The first one with a similar core diameter of 8 cm as the older compressor was built to work with the Pharmed BPT tube model 06508-17, inside diameter of 6.4 mm. A larger model, core diameter of 9.5 cm and 12.7 mm 06508-82 tube model, was also tested to increase the production of polarized ^{3}He.

Fig. 2.6. Picture of the new peristaltic compressor design.

2.1.6. NMR

Although Nuclear Magnetic Resonance induces polarization losses at each measurement of ^{3}He nuclear magnetization, it is the most suited technique to deduce the polarization in the storage cell where no discharge is sustained, which explains why optical methods cannot be used. Another method relying on the detection of the static magnetic field produced by the spin-polarized ^{3}He was developed in Mainz [Wil97] with the use of a similar fluxgate magnetometer as the one described in paragraph 2.1.1 but dense samples are required and NMR has a higher sensitivity.

The NMR system was completely rebuilt (see Fig. 2.7). New square Helmholtz transmitter coils, of 107 cm radius, 20 turns each, were mounted on the main aluminium frame to give a homogeneous B_1 field over the storage cells volume and an easy access to the different elements. They have been tuned to 55 kHz (inductance L = 3.85 mH, resistance R = 12.63 Ω). Radio-frequency pulse at the frequency of 53.3 kHz is produced by a generator (GW Instek GFG 3015), whose external trigger option allows a precise control of the number of oscillations, and amplified with a 100 W DMOS audio amplifier (model TDA 7294). Concerning the pick-up coils, two different systems were built. The first one consists of two circular coils of 40 turns, 30 mm apart from each other (R = 24 Ω, L = 1.55 mH) and whose diameter (72 mm) was chosen to fit the size of the 1.1 L storage cell. A smaller one is dedicated to the 5 cm long and 5 cm diameter storage cell and is made of two rectangular coils of 120 turns each (R = 50 Ω, L = 3.76 mH). Litz wire was used for both pick-coils and each of them has their own tuning and matching circuits. A similar Q factor of 20-25 was achieved in both coils.

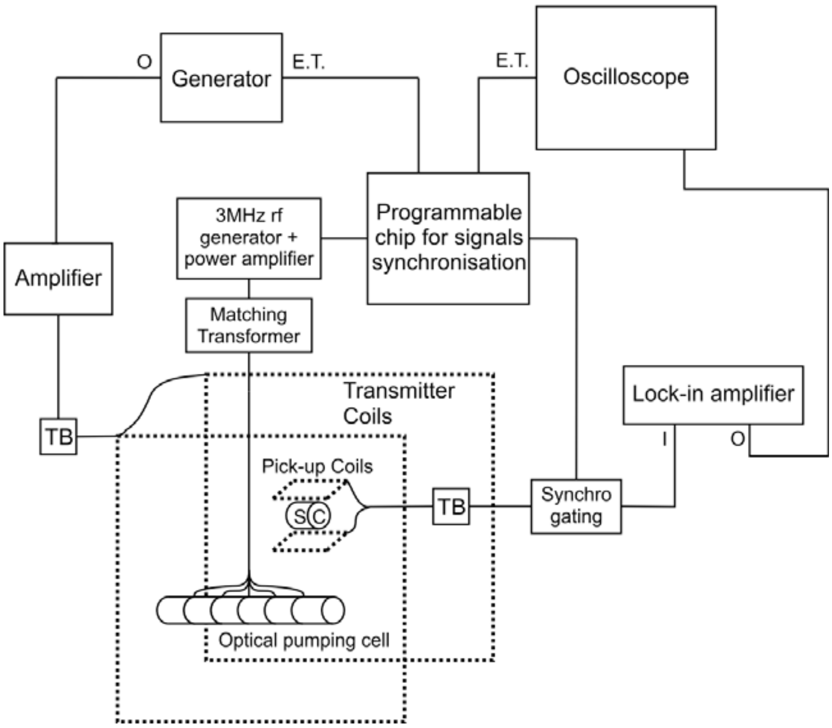

Fig. 2.7. Scheme of the NMR acquisition (see text). (TB: Tuning and matching circuit, I: Input, O: Output, S.C.: Storage Cell, E.T.: External Trigger). A microprocessor at the center of the NMR system is used to control the different elements.

During NMR experiment a chosen pulse is sent through transmitter coils that causes free precession of the storage cell's magnetization. This free induction decay (FID) signal at 53.3 kHz is then detected by the pick-up coils and a digital lock-in amplifier (LIA, SR 830, Stanford Research systems, Sunnywale, California, USA) applies synchronous detection. The output of the lock-in amplifier is recorded on a numerical oscilloscope that had the possibility to transfer recorded waveforms from its memory to a personal computer via USB connector. The free induction decay is revealed by the LIA using its internal clock a little off resonance to get a sufficient number of oscillations during the decay. Data analysis can be performed on a standalone PC, using a peak to peak analysis of the oscillations and fitting these values to retrieve the initial amplitude of the FID. A proper gating circuit protects the LIA at the time of the rf pulse and turns off the discharge during data acquisition to minimize the noise. The key element of the NMR system is a programmable microprocessor (Atmega 8, Atmel, San Jose, California, USA), which is synchronizing all the different elements together.

Four output signals are delivered by the microprocessor:

- one switches off the radio-frequency discharge inside the OP cell just before the rf pulse,
- a second signal is sent to the external trigger of the generator and commands the NMR pulse length,
- an opto-isolator coupled to flip flop diodes opens the gate and let the signal go through to the LIA after the ringing time of the transmitter coils,
- a last logic signal triggers the acquisition of the oscilloscope.

It is possible to program the length of the pulse, the delay between two pulses, the ringing off time after the pulse and the acquisition time through a simple interface with display (LCD panel). This home made device therefore offers an easy control of all the parameters and facilitates the NMR acquisition.

2.1.7. NMR calibration

At last, NMR was calibrated against an optical method with the use of a sealed cell filled with helium-3 at the pressure of 1.6 Torr. This cell was chosen because it had the exact same shape and dimensions, 5 cm in length and 5 cm in diameter, as the small storage cell used for rat lung experiments. In this case and for the same position inside the pick-up coils, the filling factor can be assumed to be the same. Different optical methods have been developed to measure accurately the nuclear polarization of ^{3}He in the presence of a rf discharge. Polarimetry of the visible fluorescence light emitted by the plasma at 667.8 nm [Big92, Lor93, Sto96a, Sto96b] and 587.5 nm [Sto96b] is one of them but the ratio of the circular polarization of the emitted light over the nuclear polarization is pressure and magnetic field dependent and needs also a calibration. A second family of polarization measurement relying on light absorption [Cou02] of a transversal (perpendicular to the magnetic field) [Big92, Tal11] or longitudinal probe [Bat11b, Tal11] presents the advantage of not requiring any calibration and not being pressure dependent. It can also potentially be operated at all field strengths. The choice of the longitudinal scheme was made because it had a higher sensitivity at low polarization, could be performed both on C_8 and C_9 lines and was easier to implement on the framework of the polarizer.

Absorbances A^+ = -ln T^+ and A^- = -ln T^- (where T+ and T- are the transmittances of the σ^+ and σ^- components of a weak laser tuned on one of these two lines) give information about the populations of the probed metastable states sublevels. In the absence of pump laser, the distribution of populations between hyperfine 2^3S sublevels is strongly coupled to that of the 1^1S state by metastability exchange collisions, which tend to enforce a spin-temperature distribution, ruled by the nuclear polarization M (see § 2.8.1 of [Bat11b]). In this spin-temperature limit, the ratio of relative populations of two adjacent m_F sublevels follows the following relation:

$$\frac{a_2}{a_1}=\frac{a_3}{a_2}=\frac{a_4}{a_3}=\frac{a_6}{a_5}=e^{\beta}=\frac{1+M}{1-M}. \tag{2.1}$$

The relative absorbances $r^+=\dfrac{A^+(M)}{A^+(M=0)}$ and $r^-=\dfrac{A^-(M)}{A^-(M=0)}$ of the respectively σ^+ and σ^- components of a weak probe laser is then directly related to the nuclear polarization (see Fig. 2.8 for C_9 line). In the case of the single-component line C_8 one can even simply derived the following relation between M and the relative ratio of absorbances R_8 [Tal11]:

$$M=\frac{1-R_8}{1+R_8} \text{ with } R_8=\frac{A_8^+(M)\times A_8^-(0)}{A_8^+(0)\times A_8^-(M)}=\frac{a_5(M)}{a_6(M)}=\frac{1}{e^{\beta}(C_8)}. \tag{2.2}$$

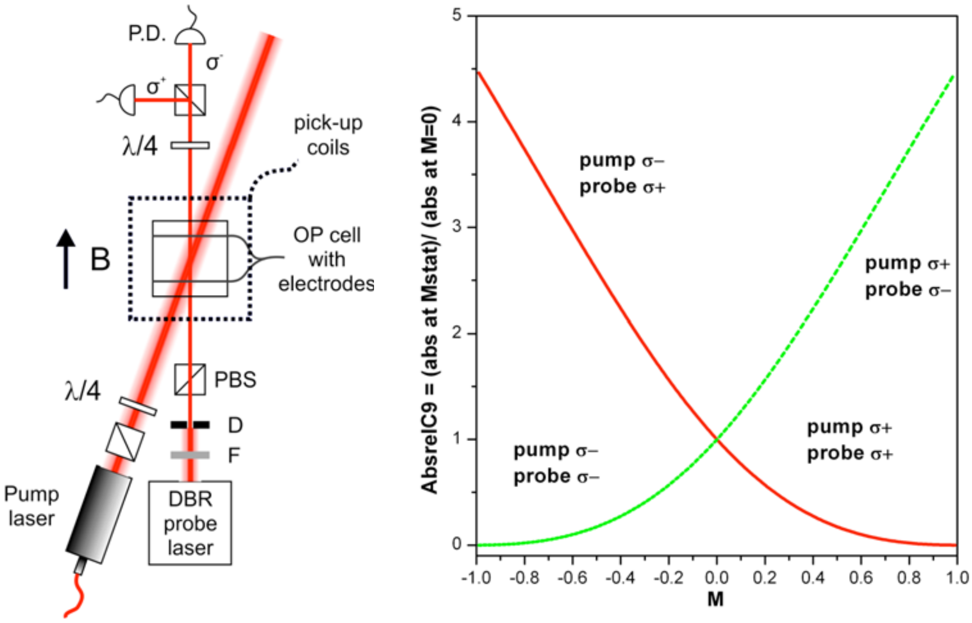

Fig. 2.8. Left: Schematic of the optical setup used for NMR calibration, see text (P.D.: Photodiode, PBS: Polarizing Beam Splitter, D: Diaphragm, F: Filter, λ/4: quarterwave plate). Right: relative σ^+ and σ^- absorbances of a weak probe laser beam tuned on C_9 line as a function of the nuclear polarization M.

The setup is described on Fig. 2.8. The sealed cell is located in the centre of the pick-up coils dedicated to the small storage cell of the same dimensions. A weak rf discharge at approximately 1 MHz is maintained by 2 electrodes wrapped around the cell. A 500 mW pump laser (see § 2.1.2), circularly polarized σ^+ and tuned on C_9 line is used to optically pump the ^{3}He contained inside the OP cell. The longitudinal probe consists of a DBR laser. A filter attenuates the level of the light intensity to the order of 20 μW/cm^2 to be in the linear regime of absorptance and to avoid significant distortion of the 2^3S population in the metastable state [Tal11]. The probe light power is also reduced with the use of a diaphragm. The beam is linearly polarized by passing through a polarizing beam splitter (PBS). After the OP cell the two components σ^+ and σ^+ of the beam are separated by a quarterwave plate and a second PBS. Both photodiode signals are recorded on the channels of an oscilloscope.

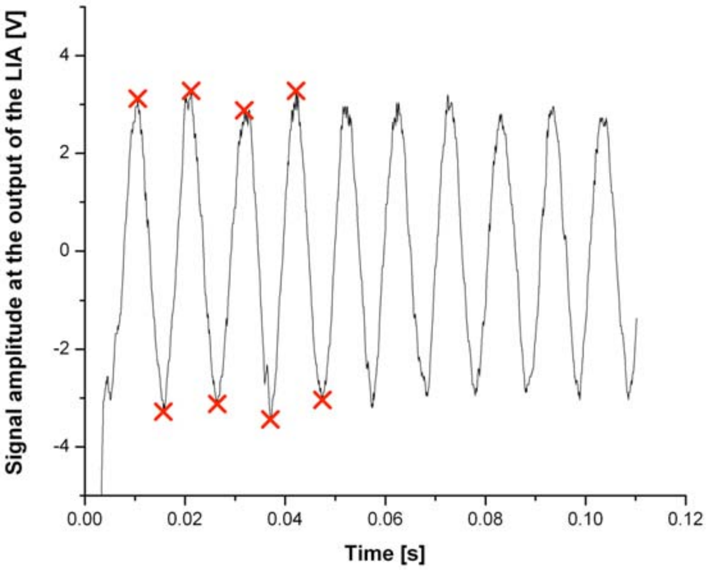

Fig. 2.9. FID signal recorded by the lock-in amplifier after the 90° pulse. At 1.6 Torr, the exponential decay time T_2^* is about 660 ms. The starting amplitude was deduced by averaging the amplitudes of the 4 first oscillations found by a peak to peak analysis of the data (red crosses).

Once the steady state polarization M_{eq} is reached, the pump is switched off to record the absorbance values $A^+(M_{eq})$ and $A^-(M_{eq})$ in the absence of the pump laser. A 90° NMR pulse then tilts the corresponding magnetization into the transversal plane and a corresponding free induction decay (FID) signal is detected in the pick up coils (see Fig. 2.9). The absorbances after the NMR pulse, $A^+(0)$ and $A^-(0)$, are also measured and corresponds to a null nuclear polarization. The pump is then switched on again and the measurement can be repeated. To increase the accuracy of the measurement, it was performed 5 times with the probe tuned on C_8 and the same amount of time with the probe tuned on C_9. Ten additional FID signals were recorded and the starting amplitude of the 20 FIDs were averaged. For C_8 line, a consistent polarization of 30.6 % was found by using the equation (2.2) and for C_9, a value of 33.5 % was deduced on the graph of the Fig. 2.8 with the measured relative absorbance ratio. This polarization of 32.1 ± 0.1 % corresponds to a starting amplitude of the FID signal of 147.6 ± 1.5 μV.

This optical method gives an accurate way to calibrate the pick-up coils of the small storage cell. Once this calibration was done, few compression experiments were performed inside the storage cell and polarization was deduced for different flows, optical pumping pressures and rotation speed of compressor. By keeping the same experiment conditions but compressing into the two other storage cells (§ 2.1.4), the second dedicated pick-up coils was also calibrated, assuming that the same magnetization was produced.

2.2. MRI facilities:

2.2.1. Low field (0.088T) scanner

Rat lungs imaging was performed at a low field MRI scanner described in details elsewhere [Suc05b]. It was specially designed for small animal lung imaging using polarized ^{3}He gas. The scanner is based on a 0.088 T permanent magnet (AMAG, Poland) equipped with a biplanar actively shielded gradient coils (30 mT/m, NRC, Winnipeg, Canada) controlled by a commercial MR Research System (previously SIMS, Surrey, Great Britain) MR4200 Narrow Band console. Dual-frequency 2.84 MHz for ^{3}He (alternatively 3.73 MHz for ^{1}H) solenoid coil was used for NMR signal detection.

For *in vivo* animal study three adult rats (race: Wistar, 400 g) were used. All experiments using animals were approved by national research ethics committees and conducted in accordance with Polish regulations and animal protection law. Each animal was anesthetized by intraperitoneal injection of chloral hydrate (40 mg/100 g body weight) and afterwards tracheotomized to simplify ^{3}He gas injection. After each hour one third of the anesthetic dose was injected again to prevent the animal to wake up. The animals were placed in a supine position on a home-build holder in the centre of the rf coil. Just before imaging the volume of 7 mL of polarized ^{3}He gas was introduced to the rats lung directly from the syringe via the trachea catheter.

For image acquisition we employed standard FLASH sequence and an additional radial sequence that was developed for both static and dynamic imaging. Both protocols utilized low-field excitation pulses optimal for polarized ^{3}He imaging. The important advantage of radial sequence as compared to FLASH is that it allows performing dynamic imaging of gas inflow with a good temporal resolution, following a single gas injection.

2.2.2. Clinical 1.5 T scanner

The clinical experiments were performed at a Siemens Sonata scanner at 1.5 T (see Fig. 2.10) in collaboration with the team at the John Paul 2nd Hospital in Krakow. A necessary update of the scanner's software and the purchase of a ^{3}He birdcage lung coil from RAPID Biomedicals allowed us to perform ^{3}He experiments at a frequency of 48.5MHz. In order to test the system, a first phantom consisting of a 250 mL vessel filled with 1.363 bar of ^{3}He and 440 mbar of O_2 was realized. A similar phantom was used already in Orsay [Vig03]. Only 14.02 mmol of thermally polarized ^{3}He is sufficient to get an FID from the phantom and the oxygen is used to shorten the longitudinal relaxation time T_1. The theoretical value of T_1 can be calculated from the equation (2.3) [Saa95] and is 5.6 s.

$$\frac{1}{T_1} = 0.448 \pm 0.01\ \mathrm{s}^{-1} \text{ per amagat of } O_2. \qquad (2.3)$$

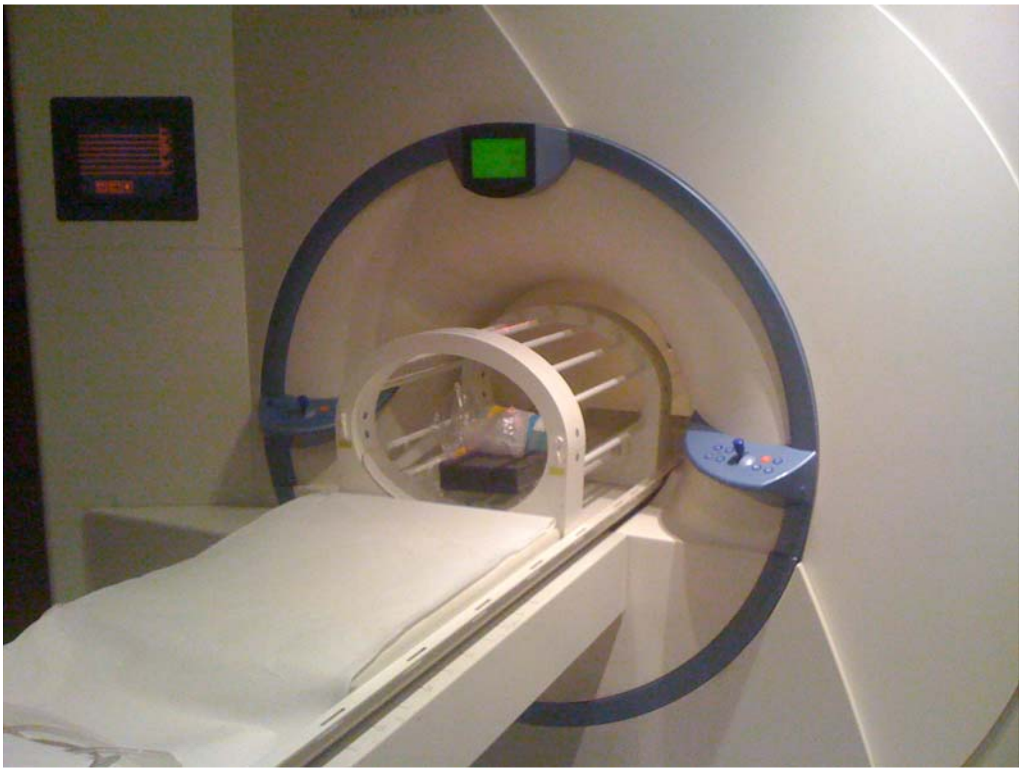

Fig. 2.10. Sonata scanner in John Paul 2nd Hospital with ^{3}He coil from RAPID Biomedical. In the center of the coil, a first phantom (see text) is placed for angle calibration experiment.

Using series of rf pulses with different repetition times from a Siemens spectroscopic sequence adapted for multinuclear experiments, an experimental T_1 of 2.8 s was found and the flip angle calibrated. Gradient recalled echo sequences being the most commonly used sequences in MRI of hyperpolarized nuclei, a multinuclear multi-slice 2D Spoiled Gradient Echo (SPGR) sequence, also known as Fast Low-Angle Shot (FLASH), was written and implemented on the scanner. For this sequence the optimal flip angle can be derived by maximizing the Signal to Noise Ratio (SNR) expression given in equation (2.4) [Lee06].

$$SNR \propto \frac{\sin(\alpha)}{\sqrt{N}} \times \frac{1 - \exp\left(\frac{-\mathrm{N} \times \mathrm{T_R}}{\mathrm{T_1}}\right) \times \cos^N(\alpha)}{1 - \exp\left(\frac{-T_R}{T_1}\right) \times \cos(\alpha)} \tag{2.4}$$

Where N is the number of k-space encoding lines, T_R the repetition time between each rf pulse and T_1 the longitudinal relaxation time in the lungs. This latter is around 20 s for in-vivo conditions [Kau09].

2.3. Results:

2.3.1. ^{3}He production using the table-top polarizer

Thanks to all the improvements described above (optimized guiding field, new laser, optical pumping and storage cells, peristaltic compressor), the table-top polarizer is now able to work in a continuous mode. The new framework gives an easier open access to the elements inside and the possibility to transport the polarizer. The value of polarization inside the storage cell can be deduced thanks to the new calibrated NMR pick-up coils. The system was verified to give a reproducible 30 - 40 % polarization (Fig. 2.11) for an OP pressure between 2.5 and 3 mbar. At this pressure and for a rotation speed of 4 to 5 Hz, the first design of peristaltic compressor has a production rate of 0.8-1 scc/min. The second larger version, working with a peristaltic tube of two times bigger diameter, also appeared to work satisfactorily and reaches 3.5-4 scc/min. As a reference, approximately 10 scc of gas are needed for a single rat lung experiment. This means that within 3 min of compression the necessary volume of ^{3}He can be polarized. For human experiment, the required volume is much higher: around 250 - 300 scc. This is obtained after about 1 h and 15 min of compression.

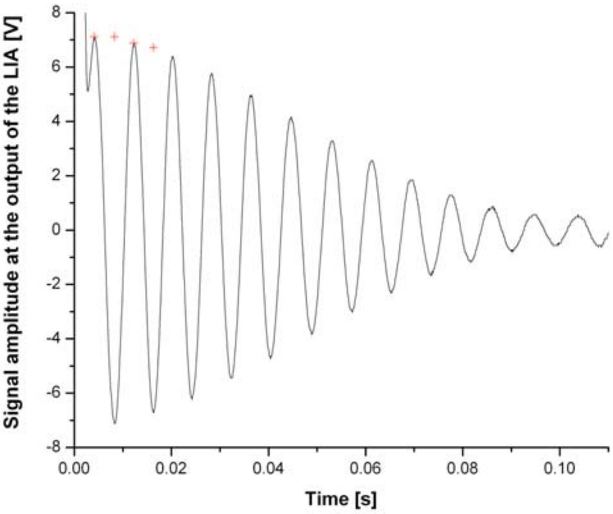

Fig. 2.11. FID signal recorded by the lock-in amplifier during a flip angle calibration and after a compression of polarized ^{3}He inside the small storage cell. The experiment lasted 6 min to reach a pressure of 57.8 mbar. At this pressure, the decay is not exponential and lasts around 100 ms. The starting amplitude was found with a linear fit of the peak to peak analysis of the 2 first oscillations. The flip angle was 45.9 ± 0.5 ° and the polarization 38.7 ± 2 %.

2.3.2. Small animal experiments

Preliminary tests have been performed on a syringe phantom. The first test was made using a spectroscopy sequence to check the increase of total magnetization and compare this value to our previous experiments [Suc05a]. Results showed an increase of a factor of 7 in the total magnetization contained in a 10 mL syringe. The new way to extract the gas from the storage cell was responsible for an additional increase of a factor of 3, which means that new MRI experiments were possible with an at least 20 times higher signal. New radial static and dynamic sequences were first implemented and tested with this phantom (Fig. 2.12). The static radial image is shown on the left. The 2 mm diameter nozzle and the 1 mm thick septum are well visible respectively at the top and the bottom of the image. An artifact inherent to the radial reconstruction is responsible for the white vertical band pattern outside the syringe. On the right side of Fig. 2.12, a series of 10 images obtained using the projection sliding window sequence are presented. The sequence started before ^{3}He entered the syringe, which explains the first 2 empty images of the series. The syringe was completely filled on the 8th image. Then, total magnetization is decreasing due to the relaxation process and the rf pulsing. That is why the image SNR gradually decreases on the 9th and 10th image.

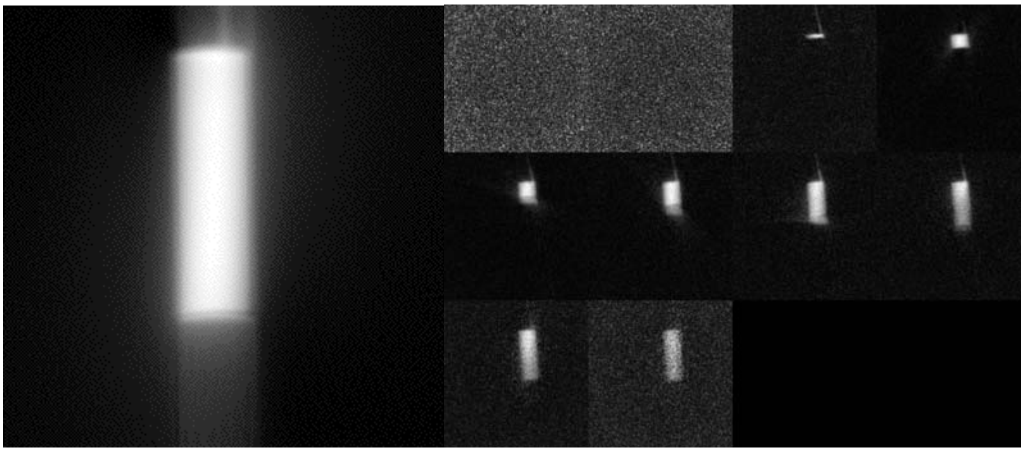

Fig. 2.12. Preliminary tests of the radial sequence made with a syringe phantom filled with ^{3}He in a 0.088 T permanent scanner. Left: static radial 2D projection image acquired with 256 samples and 200 views, 10 cm field of view (FOV), 25 kHz bandwidth, 6.1° flip angle, acquisition time (t_{ac}) of 4 s, TR = 20 ms. Right: dynamic series of radial 2D projection sliding window images with 128 samples and 100 views, 10 cm FOV, 33 kHz bandwidth, 8° flip angle, t_{ac} = 21 s.

These tests were followed by in vivo experiments with rats. Compared to the results previously reported by our group [Suc05] a two-fold increase in spatial resolution and a four-fold increase in the SNR was observed, significantly improving the quality of the static images acquired during breath-hold (Fig. 2.13) as well as the dynamic images representing the gas inflow into the animal's lung (Fig. 2.14).

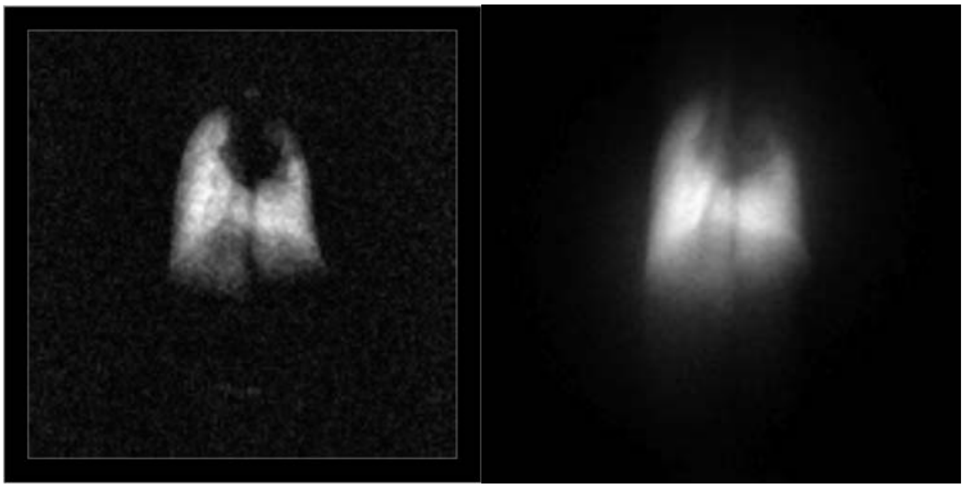

Fig. 2.13. Transverse ^{3}He images of rat lungs in vivo acquired with the (left) FLASH sequence (slice thickness 80 mm, FOV = 80 mm, imaging matrix 128*128, 8° flip angle, 10 kHz bandwidth, no averaging, echo time = 7 ms, repetition time = 32 ms, t_{ac} = 4 s) and the (right) projection radial one (FOV = 80 mm, 128 samples per 200 views, repetition time = 20 ms, t_{ac} = 4 s, 10 kHz bandwidth, flip angle 7°, no averaging).

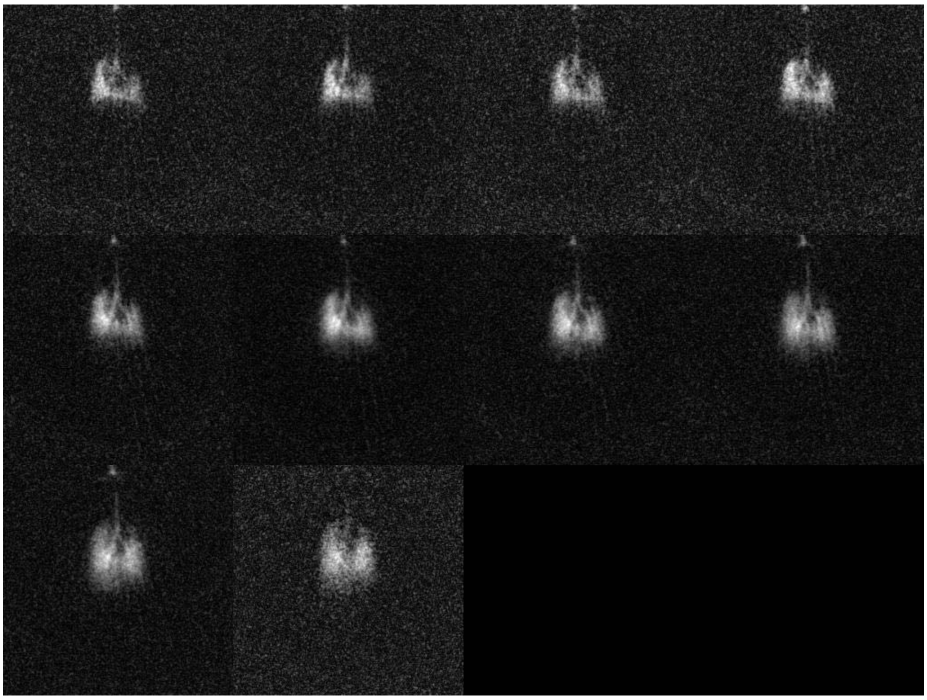

Fig. 2.14. Transverse ^{3}He radial projection sliding windows images of rat lungs in vivo (100 mm field of view, 128 samples and 100 views, 33 kHz bandwidth, flip angle 8°, t_{ac} 20 s).

2.3.3. Human lung images

Preliminary tests were required to validate the sequence. The signal coming from the first phantom described in paragraph 3.2) being too low for an imaging sequence, we decided to optically pump a 11.5 cm long cell of 14 mm inner diameter filled with 128 mbar of ^{3}He directly inside the scanner. The cell had a volume of approximately 20 mL, which corresponds to 2.5 scc but a polarization on the order of 30 % can be obtained at 2 T. The different mechanisms and features of Metastability Exchange Optical Pumping in high field are not the subject of this chapter and are described in § 1.4 and 1.5. A 500 mW laser was tuned at 1083 nm on the f^{2m} pumping line (see notation in § 1.4). After waiting few minutes for the steady state polarization to be reached, the FLASH sequence was successfully tested with this phantom.

Thanks to the new larger design of the peristaltic compressor, few boluses of ^{3}He could be carried to hospital inside the transport box and the storage cell. The polarization process takes 1h to get 240 scc of ^{3}He. The polarized gas was then mixed with N_2 until reaching the atmospheric pressure inside the 1.1 L storage cell. Once in hospital, 81 % of the total gas was extracted to the Tedlar bag previously rinsed with ^{4}He. Lungs of a healthy volunteer were washed with 1 L of clean N_2 before inhalation from the Tedlar bag. The image was taken 1 h after the end of the polarization process. The FLASH sequence was launched directly after inhalation. The field of view was 35*35 cm for a matrix of 64*64. A bandwidth of 16.64 kHz was used with a slice thickness of 20 cm to cover the whole lungs. There was no averaging and the sequence lasted approximately 500 ms (TE = 3.6 ms and TR = 7.5 ms). An 11° flip angle used in the experiment was calculated to be optimal. The result is shown in Fig. 2.15. This image is the first MRI picture of human lungs using hyperpolarized gas made in Poland.

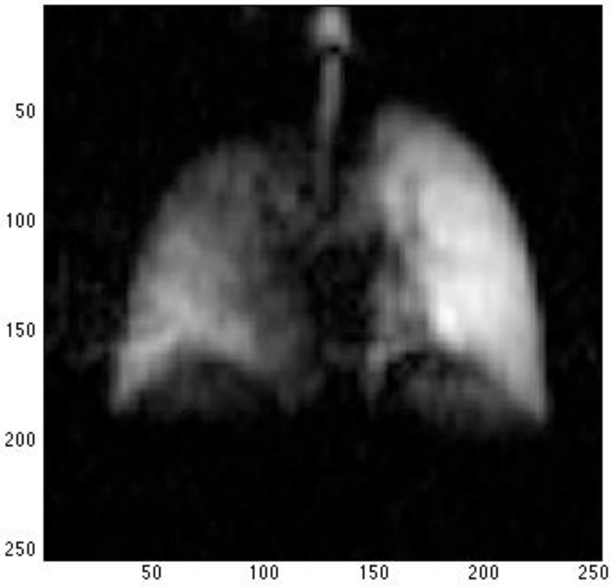

Fig. 2.15. Transverse ^{3}He image of healthy volunteer's lungs using a FLASH sequence (20 cm slice thickness, 35 cm FOV, 64*64 matrix, flip angle: 11°, 16.64 kHz bandwidth, TE = 3.6 ms, TR = 7.5 ms).

2.4. Summary of the low-field polarizer:

Improvements of our table-top polarizer, leading to the efficiency of 3-4 scc/min and a reproducible corresponding polarization of about 30-40 % inside storage cell have been reported in this chapter. The improvements are mainly due to the implementation of a broader bandwidth 10 W laser and a new design of the peristaltic compressor. Thanks to these modifications the magnetization was increased by a factor of 20, which allowed improved FLASH rat lungs pictures to be taken and moreover, to implement radial dynamic and static sequences. These ventilation images show a sufficient resolution and SNR to be used for diagnostic or medical tests. In addition we were also able to polarize a necessary quantity of ^{3}He to take the first picture of human lungs made in Poland. Compared to rat images, the resolution of human lung images is still low. A major issue for this problem is probably the loss of polarization during transportation and extraction.

The losses due to relaxation time inside transport box and storage cell are minimal and can be easily assessed: the exponential decay time T_1 is of the order of 6 h and the transport lasted 1 hour (corresponding to a 15 % loss of magnetization), the losses due to the transfer of storage cell inside transport box were checked to be around 7 % and only 81 % of the gas mixture was compressed inside the Tedlar bag. All these losses together correspond to a total loss of 36 % but the major issue is probably due to the time spent (around 1.5 min) during compression inside the Tedlar bag in the non-homogeneous fringe field of the magnet. Moreover transportation of the bag inside the scanner is probably adding also few losses.

An easy solution to this major loss would be to build a second smaller guiding field close to the magnet for minimizing the losses due to field inhomogeneities during the second compression from storage cell to the Tedlar bag. In the same way the table-top polarizer could also be transported close to magnet in hospital and the gas directly produced few meters away from it. But none of these solutions have been chosen by our group. As it is greatly described in the next chapters and contrary to the other groups, we decided to work on the alternative solution of performing MEOP at higher magnetic field and build a high field polarizer. Previous promising experiments have been done and showed a great increase in production rate efficiency [Col10]. This would solve both problems of transportation and polarization time.

Chapter 3

Systematic studies in high field:

The first experiments of MEOP in high field have been performed at 0.1 T in 2001 [Cou01] and already showed a factor 2 increase in nuclear polarization in a 40.4 mbar cell. First attempt to explain this important improvement was published shortly after [Nac02], and the thesis work of Marie Abboud [Abb05a] was dedicated to extend the field of studies to 1.5 T. Her main results were published in [Abb04, Abb05b], demonstrating the possibility to efficiently obtain polarization on the order of 25 % in cylindrical cells (diameter 5 cm, length 5 cm) filled with 67 mbar of pure ^{3}He. A first crude model of MEOP at 1.5 T was proposed in the corresponding thesis dissertation [Abb05b] but the lack of agreement between experimental results and the computed values from the model was the main motivation for a joint collaboration between Kastler Brossel Laboratory in Paris and our group for deeper investigations. Systematic studies of MEOP were then performed in a wide range of magnetic fields (0.45, 0.9, 1.5, 2 and 4.7 T), pressures (from 1.33 to 267 mbar), discharge conditions, but also with different OP transitions, pump laser bandwidths, intensities and beam shapes. At the beginning of the present work, some preliminary results for 32 and 67 mbar cells (diameter 1.4 cm, length 11 cm) were already published, describing an optical measurement technique of polarization [Suc07] and showing a dramatic increase in polarization [Nik07]. A value of 52 % was obtained at 2 T and at 67 mbar, using what appeared to be the most suitable line for MEOP at high magnetic field: f^{2m}. These systematic studies are now finished and although data have not been fully analyzed yet, an optimization of the laser beam spatial profile has been published in [Doh11a, Doh11b] and a summary of the main results can be found in the thesis dissertation of Anna Nikiel [Nik11]. My contribution to these studies is presented in this chapter and consists of extending the range of magnetic field to 4.7 T and implementing the annular profile shape of the pump beam at 1.5 T.

3.1.Materials and methods:

A schematic of the experimental setup is presented in Fig. 3.1. All optics elements and the bone-shape sealed cell are mounted on an amagnetic plate (Dural) inside the homogeneous area of the magnetic field produced by a superconduting magnet. Electrodes, driven by a radio frequency generator and a high power amplifier, are wrapped around the cell and produce a weak plasma discharge inside the cell. The pump laser beam, parallel to the magnetic field, is circularly polarized by a polarizing beam splitter and a quarter-wave plate. The laser is back-reflected by a mirror to double the efficiency of OP and the transmission is monitored by a photodiode. A longitudinal optical detection method is used to measure the ^{3}He nuclear polarization in the cell during experiments (see § 3.1.4). The probe laser beam is passing through a small aperture diaphragm before being also circularly polarized and delivered to the sealed cell by means of a set of mirrors. Due to experimental restrictions, the beam is actually propagating with a very low angle with respect to the magnetic field axis. The transmission of the probe is also monitored on a second photodiode.

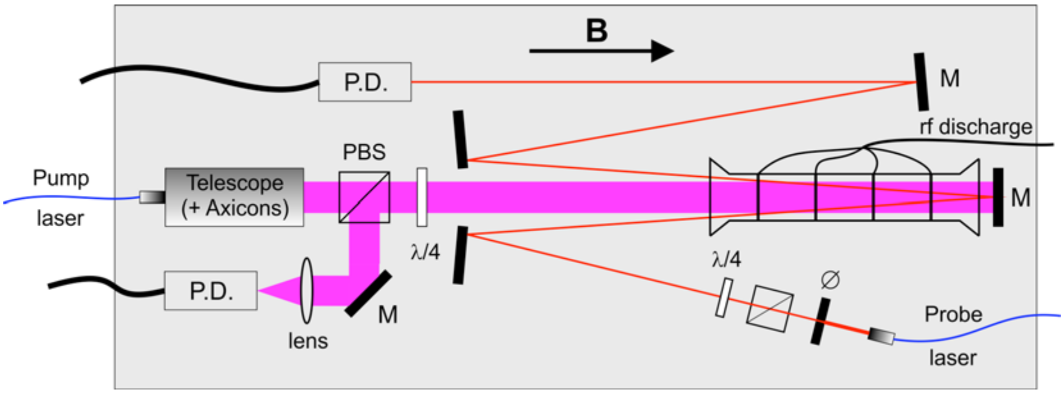

Fig. 3.1. Schematic of the optical setup used for systematic studies at 1.5 and 4.7 T. Probe and pump laser beams are first circularly polarized by a polarizing beam splitter (PBS) and a quarter-wave plate (λ/4). A set of mirrors (M) makes them pass through the OP cell in parallel with the magnetic field (B) before being recorded by two photodiodes (P.D.). The pump laser beam is expanded by a Kepler-like telescope and, in the case of 1.5 T experiments, the shape is reversed by the means of a pair of axicons whereas the probe beam is diaphragmed by a small aperture (∅ ≈ 1.5 mm).

3.1.1. Source of magnetic field

The experiments were performed in two different superconducting magnets (Fig. 3.2). The first one (Magnex Scientific), in which most of the systematic studies have been carried out [Doh11a, Doh11b, Nik07, Suc07], belongs to our group and its field can be varied from 0 to 2 T. Its bore has 30 cm diameter and the inhomogeneities were measured to be on the sufficient order of 2‰ at the location of the optical pumping cell. Field values were measured in a virtual cylinder (diameter 4 cm, length 12 cm) in the center of the magnet, which corresponds approximately to the place where the cell was situated. Experiments at 4.7 T are the results of a collaboration with the Institute of Nuclear Physics, Polish Academy of Sciences, in Krakow, that allowed us to use its Bruker scanner dedicated for animal MRI studies. The bore was smaller (≈ 20 cm) and that is why the optical setup was improved to fit on a 20 * 70 cm plate (see Fig. 3.2). On the other hand, inhomogeneities were much smaller (≈ 2 ppm), due to the high quality standard for MRI.

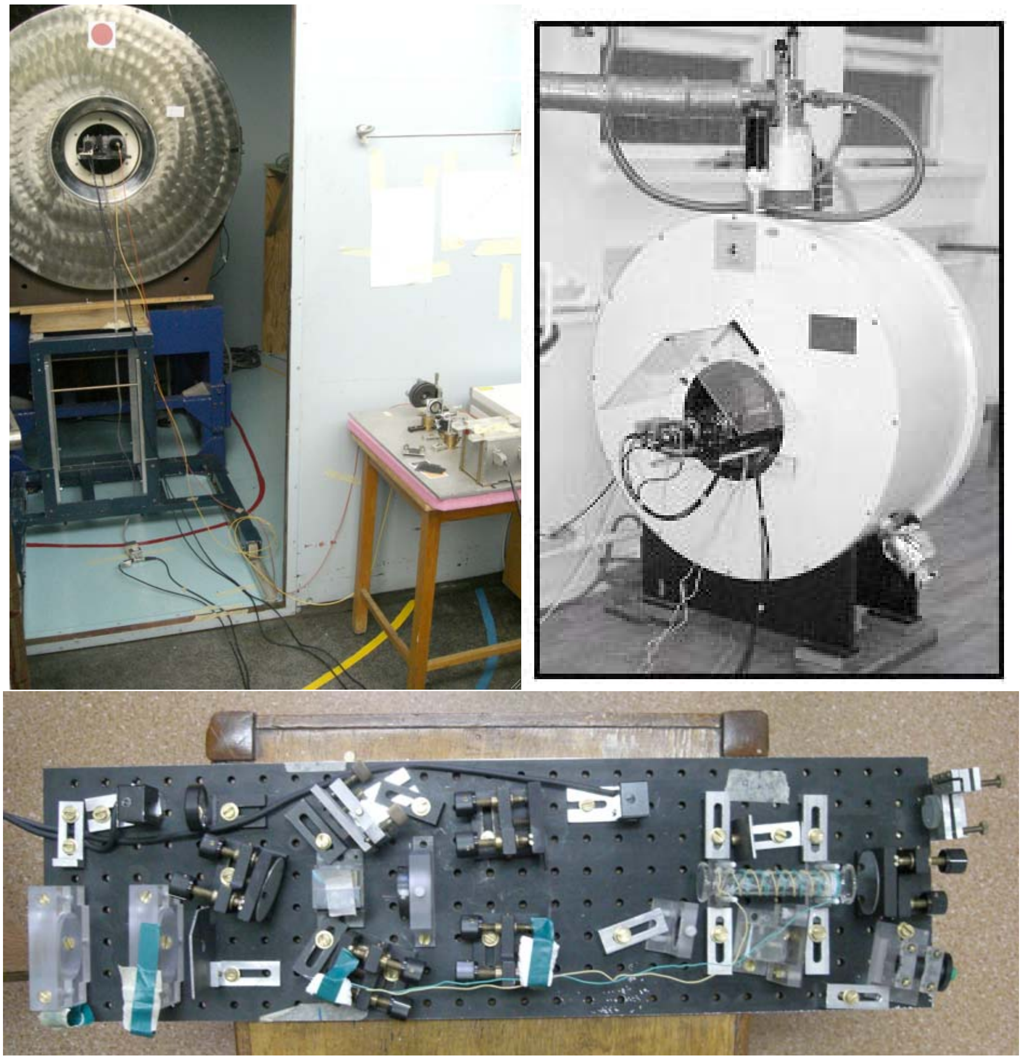

Fig. 3.2. Pictures of the superconducting magnets with the optical setup mounted inside their bore (top) and the optical setup (bottom). Top left: Bruker 4.7 T MRI scanner. The table with probe and pump laser were located outside the Faraday cage. Top right: 2 T Magnex Scientific magnet. Apart from the optical setup, the rest of equipment was situated in a separate room. Bottom: optical plate dedicated to 4.7 T experiments (both probe and pump lasers are absent in the picture).

3.1.2. Optical pumping cells

Six sealed “bone-shaped” cells filled with high purity ^{3}He (inner volume ≈ 20 mL) and made of Pyrex glass were used for the experiments. The length of the cells (11 cm) was chosen with respect to the homogeneous area of the magnetic field in the 1.5 T scanner. Their small inner diameter (1.5 cm) is well suited for creating plasma discharge at relatively high pressures, which results in light absorptance enhancement in comparison with 5 cm diameter cells used in previous studies. Bone-shaped name comes from the optical windows (2.5 cm diameter) connected on both ends. Cells were prepared in Kastler Brossel Laboratory and special care was taken to avoid any impurities that could reduce the lifetime of metastable atoms. Prior to filling procedure, cells underwent a cleaning process consisting of rinsing with proper detergent and deionized water, baking out during several days in a 700 K oven with relatively high vacuum conditions ($P \approx 10^{-8}$ mbar) and with strong rf-discharges in ^{4}He. Once only spectral lines of helium were observable in the plasma fluorescence, they were finally filled with 1.33, 32, 67, 96, 128 and 267 mbar and sealed. These pressures correspond to the pressures measured at room temperature and can slightly increase during experiments while the rf-discharge heats the cell. The plasma discharge was generated by a 2 MHz generator and a 50 W rf power amplifier, supplying two spiral electrodes wired onto the outer surface of the cell tube. It was easier to switch on discharge at high pressures in this configuration rather than in the standard set of circular electrodes. Metastable atoms densities on the order of 10^{10}-10^{11} atoms/cm^3 were obtained.

3.1.3. Pump laser beams

The same source of 1083 nm light as in § 2.1.2 was used for the pump beam. It consists of a broadband (2.1 GHz FWHM) ytterbium fiber laser with 10 W maximum output power. In the case of 4.7 T experiment, the output of the fiber was collimated by an APC collimator (model F220APC, Thorlabs, Newton, New Jersey, USA) and expanded by a Kepler-like telescope (ratio of focal lenses = 7) into a 4.9 mm FWHM Gaussian beam (Fig. 3.3). At 1.5 T, a pairs of axicons (Eksma Optics, Vilnius, Lituania) was added to the telescope to obtain an annular profile whose external diameter was about 30 mm. In order to fit this beam to the internal diameter of our OP cells, an additional telescope with magnification 2.5^{-1} was used. The resulting profile is shown in Fig. 3.3.

The axicon term was suggested for the first time by McLeod in 1954 [McL54] to define refractive or diffractive cylindrically symmetric optical elements and refers in the present dissertation to a conical prism. One specific characteristic of axicon is that the image of a point source turns into a line along the optical axis. That is why it does not have any focal length. A pair of axicons can transform a Gaussian beam into an annular beam without any loss of energy (Fig. 3.4). The axicons used were made of BK7 glass with refractive index 1.57, a diameter of 50.8 mm and a base angle of 10°.

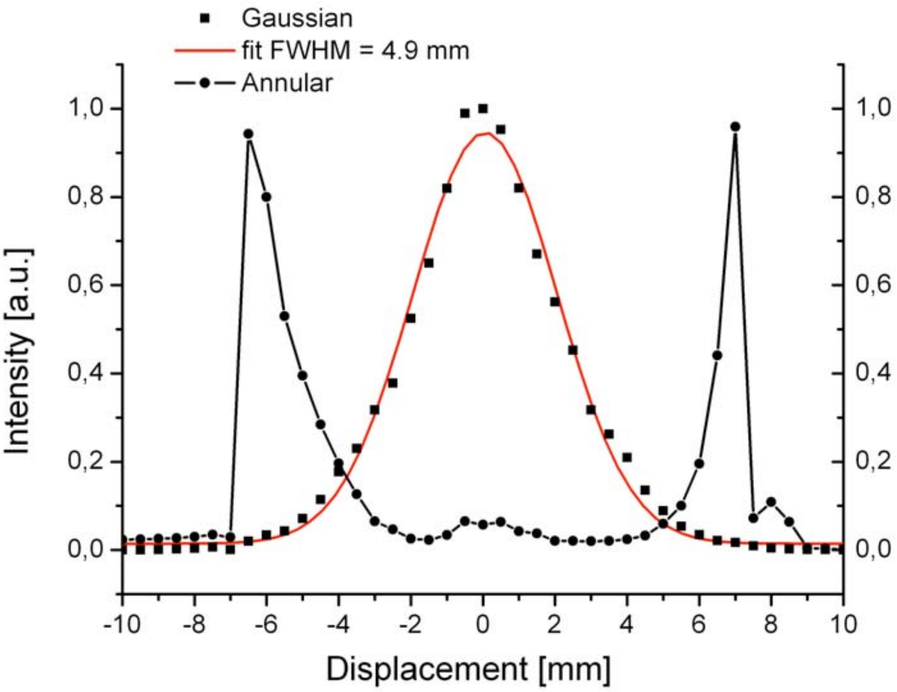

Fig. 3.3. Transverse intensity profiles of the Gaussian (circles) and ring-like beam (squares) generated by the Keopsys laser. Fitting the data to a Gaussian curve gives a 4.9 mm Full Width at Half Maximum (FWHM). The outer diameter of the annular beam could be regulated to fit the diameter of the optical cells (≈ 14 mm) by varying the distance between the two axicons. The reference of the displacement axis is the center of the cell.

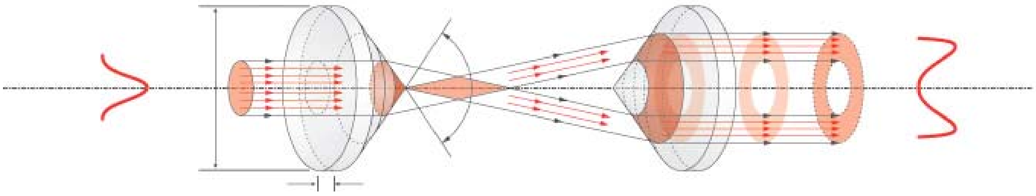

Fig. 3.4. Principle of the Gaussian beam transformation to an annular beam by means of a pair of axicons. The central part of the Gaussian beam is refracted to the external part of a resulting conical beam by the first axicon. The second axicon needs to have the exact same angle as the first one to re-collimate the beam into an annular shape. The angle and the distance between the pair of axicons determine the outer diameter of the beam.

The idea of using axicons for MEOP experiments comes from the absorptance profiles measured as a function of the radial position inside the cell at high magnetic field and high pressure (Fig. 3.5). A broad beam from a DBR laser (FWHM = 10.2 mm) was used for the measurements with a photodiode fixed on a non magnetic displacement system (step 0.5 mm). The absorptance A was calculated as follow:

$$A = \frac{I_1 - I_2}{I_1 - I_0} \tag{3.1}$$

where I_0 is the signal recorded on the photodiode when laser and discharge are switched off (noise signal), I_2 when both laser and discharge are switched on and I_1 when the laser is on and discharge is off (background signal).

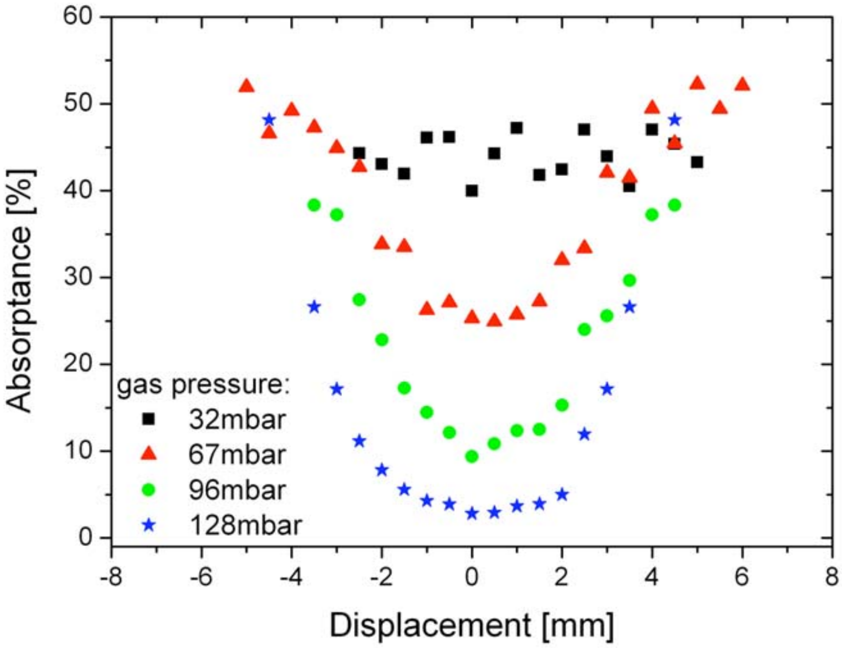

Fig. 3.5. Comparison between laser absorptance profiles collected for various ^{3}He gas pressures. The measurements were done at 2 T.

At 32 mbar, the absorptance is nearly constant everywhere in the cell but as the pressure increases, absorptance dramatically drops at the center of the cell. The absorptance reflects the distribution of metastable atoms in the cell, which in turn are involved in the OP process. It is not surprising to see such results knowing that at high pressures, plasma molecules and metastable atoms are created in the area of high electric field, which means close to the electrodes. The strong magnetic field actually enforces such behavior by adding a force on the moving charges of the plasma. This effect is clearly visible when looking at the light distribution coming from the cell. When pressure increases, the diffusion of metastable atoms is reduced and they loose excitations before diffusing to the center of the cell. If a Gaussian beam is used at high pressure, there is only a partial overlapping of the laser beam with metastable atoms distribution and a large fraction of the pumping laser power is wasted. Therefore, in order to optimize the OP process, a pair of axicons is used to match the plasma distribution. A complete study at 2 T comparing four different laser shapes, among which the annular one, have been published in [Doh11a, Doh11b]. As expected, results showed that the best performance was achieved with the ring-like beam profile at high pressure and a nuclear polarization of 26 % was obtained at 267 mbar.

Unfortunately, the axicons could not be implemented for the 4.7 T experiment due to space restrictions on the optical plate. The pump laser frequency was tuned on f^{2m} transition (see Fig. 1.8 and 1.9) and its power varied from 0.5 to 2 W at 4.7 T and from 0.5 to 5 W at 1.5 T.

3.1.4. Optical measurement of nuclear polarization

The optical detection method relies on the absorption measurement of a weak probe beam and was already fully described in [Suc07]. The main principle is recalled in this subsection but as it will be evoked in § 3.2, the collisional broadening happening at high pressure is responsible for a great change in absorption lineshapes and requires a necessary improvement in data analysis.

Compare to low field longitudinal probe scheme where the nuclear polarization can be inferred from the absorbances ratio of the two components σ^+ and σ^- (§ 2.1.7), it is necessary at high magnetic field to probe two different single transitions for which 2^3S_1 involved sublevels are not affected by the pump laser. When pumping on f^{2m}, the σ^+ probe doublet ($A_2 \rightarrow B_9$ and $A_1 \rightarrow B_{10}$ transitions, see Fig. 1.9) satisfies these requirements. In practice, a second 50 mW DBR diode laser was implemented to produce a weak beam (≈ 100 μW/cm^2) of 1.5 mm diameter to probe the sublevels A_1 (m_F = -3/2) and A_2 (m_F = -1/2). Effect of probe intensity on absorption measurement was introduced in [Cou02]. For the intensity level used in these systematic studies, the optical pumping rate is negligible compared to the metastability exchange collisions rate that tends to impose the spin temperature distribution. Thus, the populations in 2^3S state can be assumed to be unaffected by the probe and the relative ratio of absorptions at the top of the lines is related to the nuclear polarization by the following formula:

$$\left(\frac{A_{-1/2}(M)}{A_{-3/2}(M)}\right)\Big/\left(\frac{A_{-1/2}(M=0)}{A_{-3/2}(M=0)}\right)=\frac{1+M}{1-M} \tag{3.2}$$

where $A_{-1/2}(M{=}0)$ and $A_{-1/2}(M)$ are the absorptions of the transition $A_2 \rightarrow B_9$ before and during optical pumping (see Fig 3.6). The same definition applies for $A_{-3/2}$ and $A_1 \rightarrow B_{10}$ transition.

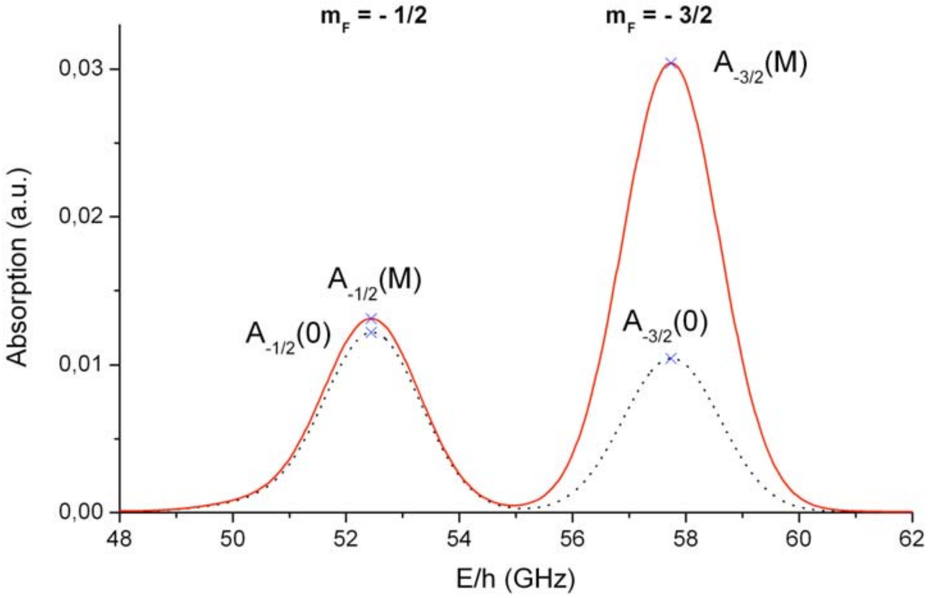

Fig. 3.6. Example of absorption spectra of the σ^+ probe doublet computed by a Fortran program at 1.33 mbar and 1.5 T for M = 0 (dotted line) and M = - 46.1 %. Peaks of the absorption lines are marked with a cross in reference to notation described in text: $A_{-1/2}(M)$…

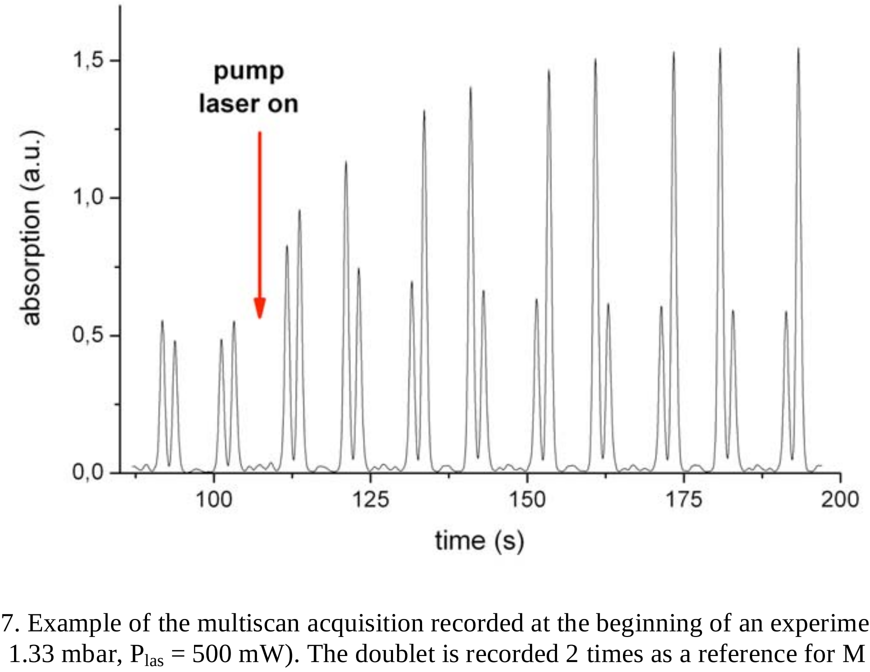

Fig. 3.7. Example of the multiscan acquisition recorded at the beginning of an experiment (B = 1.5 T, P = 1.33 mbar, P_{las} = 500 mW). The doublet is recorded 2 times as a reference for M = 0 before the pump is switched on at t ≈ 110 s. The relaxation decay is not showed for clarity.

At 1.5 and 4.7 T, the two transitions are separated by 5.3 GHz. That is why the laser frequency needs to be continuously swept back and forth over the σ^+ probe doublet by the temperature control of the laser diode. This is done during all the OP and relaxation processes to measure M(t). It takes approximately 10 s to scan one doublet (≈ 1.5 GHz/s) and the resulting data consist of recorded "multiscan" (Fig 3.7). If deducing the nuclear polarization when the stationary value (M_{eq}) is asymptotically reached is straightforward, interpolation between successive measurements during build-up and decay is required. This analysis is automatically performed by a Fortran program (see § 3.2).

3.1.5. Data acquisition

On Fig. 3.8, a block diagram of the data acquisition is presented. To improve sensitivity and separate the resonant atomic response from the infrared stray light background in photodiode signals, the amplitude of the 2-MHz rf voltage applied to the external electrodes was slightly modulated (15 % modulation depth) at 80 Hz for 4.7 T experiments and at 40 Hz at 1.5 T. This induces a slow time variation of the number density of 2^3S atoms in the gas, hence of the transmitted light intensity, that is analyzed using digital lock-in amplifier (Stanford Research Systems SR830, Sunnyvale, CA, USA, LIA3 in Fig. 3.8) for P.D.2 and analog lock-in amplifier (Unipan 232B, Warsaw, Poland, LIA1 in Fig.3.8) for P.D.1. In contrast with [Nik07] and [Suc07] where a similar longitudinal probe beam configuration was used, a double modulation scheme was implemented for the probe acquisition channel to remove any spurious contribution from the transmitted pump light on the P.D.2 signal. In practice, a mechanical chopper was inserted in the probe beam path before its injection into the single-mode fiber, modulating the incident probe power at a frequency of 1 kHz. The signal was analyzed by the lock-in amplifier LIA2 (similar model to LIA3). Six analog signals were recorded (channels 0 to 5) using data logger (National Instruments type 6221, Austin, Texas) interfaced to a personal computer via its PCI port and subsequently processed offline to obtain:

- The average transmitted pump power CH0, provided by the integrator that filters out the modulated part of P.D.1 output voltage.
- The amplitude of modulation of the transmitted probe power CH1, provided by LIA3.
- The amplitude of modulation of the transmitted pump power CH2, provided by LIA1.
- The average transmitted probe power CH3, provided by numerical time integration of the output voltage of LIA2.
- The average transmitted probe power CH4, provided by the integrator that filters out the modulated part of P.D.2 output voltage.
- The transmitted pump power CH5 at the output of P.D.1. This channel has no use in theory but practically it was an alternative channel for CH0 whose integrator appears to have occasionally electronic issue.

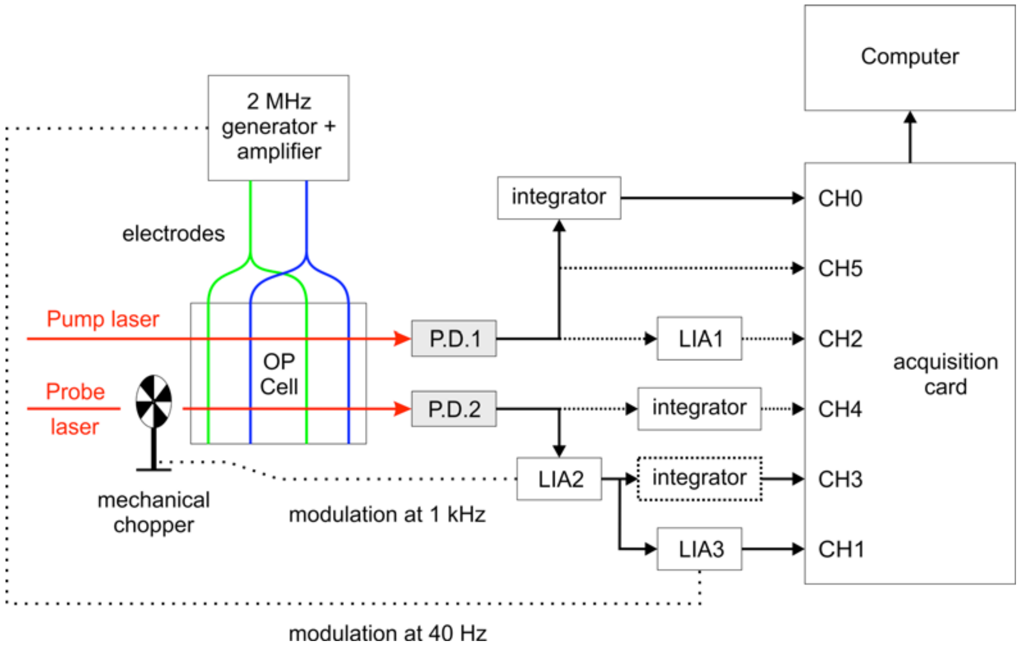

Fig. 3.8. Block diagram of the data acquisition scheme. P.D.1, P.D.2: Photodiodes. LIA1, LIA3 (resp. LIA2): lock-in amplifier for slow (resp. fast) demodulation of the transmitted probe and pump light signals. A tuned transformer (not shown) between amplifier and electrodes was used to obtain high voltage. The dotted arrows represent an update for 1.5 T experiments and channel 5 (CH5), 2 and 4 were not recorded at 4.7 T.

It is important to note that these experimental conditions were unfortunately not matched completely at 4.7 T. Systematic studies at 4.7 T were the first experiments for which double detection scheme was implemented and it was not possible to repeat them. As shown in Fig. 3.8, channels 2, 4 and 5 were not recorded and the integrator of channel 3 was absent. As we will see in § 3.3, it has a small consequence on the data noise level and limits possible interpretation of data analysis.

3.1.6. Experimental procedure

For each pressure (cell), five or six experiments were recorded corresponding to 3 different discharge conditions (weak, moderate and high discharge) and to 3 or 4 pump laser powers (0.5, 1, 2 and 5 W at 1.5 T). Before and after each experiment, the absorption of both probe and pump lasers were measured in low intensity conditions. During the first 30 seconds of the acquisition, the offsets of each channel were recorded using the following procedure:

- pump, probe and discharge switched off for few seconds,
- probe laser on,
- pump laser on but without discharge,
- pump off,
- discharge on and acquisition of the 4 first doublets as a reference at M = 0.

Once the offsets are acquired, pump laser is switched on and optical pumping can start. When M_{eq} is reached (build-up time t_b), the pump laser is switched off and relaxation characterized by decay time T_{decay} occurs. An example of the experimental procedure is shown in Fig 3.9 at 1.5 T, 1.33 mbar and high discharge. It was chosen due to its fast dynamics for clarity but because of strong hyperfine decoupling at 4.7 T, acquisition can last more than two hours in high pressure cells. More explanations about each step of the experimental procedure and what can be derived from them will be given in the next subsection of data analysis.

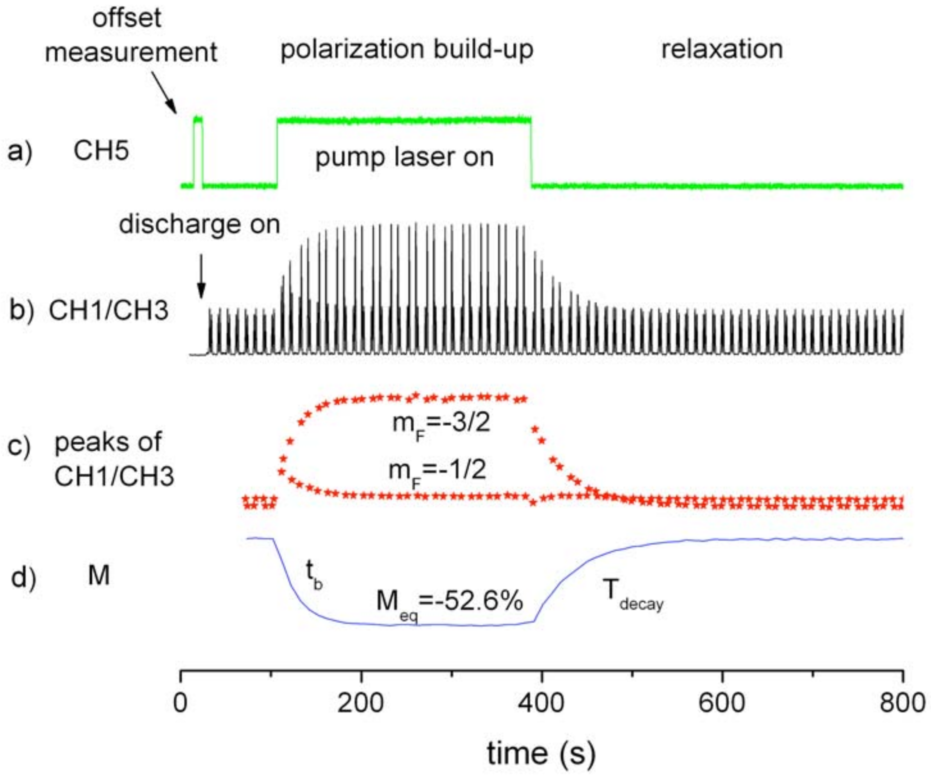

Fig. 3.9. Example of data acquisition a) CH5 recording: the first seconds are dedicated to offset measurement (see text) before OP (pump on) and relaxation (pump off). b) CH1/CH3 is proportional to absorption signal. Example of data analysis c) peaks of absorption lines in CH1/CH3 data. From these peaks (proportional to $A_{-1/2}$ and $A_{-3/2}$), the nuclear polarization can be derived d) Resulting M evolution: build-up process with time constant t_b until steady-state polarization M_{eq} and exponential decay (T_{decay}).

Remark: experimental procedure was a little different at 4.7 T. Photodiode offsets were not recorded at the beginning and the pump and probe absorptions were measured only once before the recording.

3.2. Data analysis:

3.2.1. Pressure broadening

In the absorption spectrum at low pressure, the Doppler broadening is the main contribution to the spectral linewidth. The Doppler width is coming from the thermal motion of the atoms and the resulting line shape is Gaussian, characterized by its full width at half maximum (FWHM): w_G. In helium plasma, a second phenomenon, consisting of atoms collisions with electrons, ions and others atoms, can influence the spectral line shape. This collisional broadening induces a Lorentzian profile, whose FWHM w_L increases linearly with pressure. The resulting shape of absorption lines is then the convolution of a Gaussian and a Lorentzian profile also known as a Voigt profile. Influence of collision broadening on absorption profile of the σ^+ probe doublet at 1.5 T have been computed for different w_L (Fig. 3.10) by a dedicated Fortran program (Voigt.exe) written by Pierre-Jean Nacher from Kastler Brossel laboratory. Voigt profiles for different pressures are compared to a simple Gaussian profile at 313 K (w_L = 0 and w_G = 2.02 GHz) and to a baseline, corresponding to the influence of other lines (mainly f^{2p}, f^{4p}) on the Voigt spectrum. Similar investigations at 4.7 T were performed and will be published soon ([Nik11], in preparation).

Previously reported high-field MEOP results [Abb04, Abb05b, Cou01, Nac02, Nik07, Suc07] have been obtained at moderate pressures ($P \leq 57$ mbar), where the two lines in the probe doublet are well resolved and simple peak height determinations could be used to infer relative populations of the corresponding 2^3S sublevels. As shown on Fig. 3.10 and for the higher pressures considered here, pressure broadening of the 1083 nm transition results in broad Voigt profiles for all hyperfine components such that, for the probe doublet:

1/ the intense f^{4P} and f^{2P} lines induce a slanted baseline;

2/ the two single-component hyperfine lines are no longer well resolved.

These changes in individual line shapes as well as the contribution from overlapping neighboring lines must be taken into account in the quantitative analysis of the measured peak heights and are responsible for the necessary following update of the data analysis.

In a first step, we used the experimental recorded absorption spectra of the probe doublet at M = 0 (first doublets of an experiment, before switching on the pump laser) to deduce the Lorentzian FWHM w_L dependence with pressure. At each pressure, experimental data were compared with spectra computed at different temperatures and pressures. An example at 67 mbar is displayed on Fig. 3.11. The fitting was done manually and special care was taken to obtain not only a good ratio of peak amplitude, but also a good agreement with the baseline on the wings of the doublet and with the minimum value between the two peaks. The compiled data are summarized in Fig. 3.12. Most of the w_G values were found to correspond to an experimental temperature of 40 ± 5 °C except from the 267 mbar cell at 4.7 T that reaches 77 °C. Values exceed room temperature because of the dissipated rf power to sustain the plasma discharge and the largest rf voltages were applied in high pressure cells to obtain stable discharges. Collisional broadening rates were found to be equal to 13.1 ± 1 MHz/mbar at 1.5 T and 12.2 ± 0.2 MHz/mbar at 4.7 T. Knowing exactly the shape of the probe doublet, two Fortran programs described in the next paragraphs were written to correct the nuclear polarization inferred by the measured peak heights analysis.

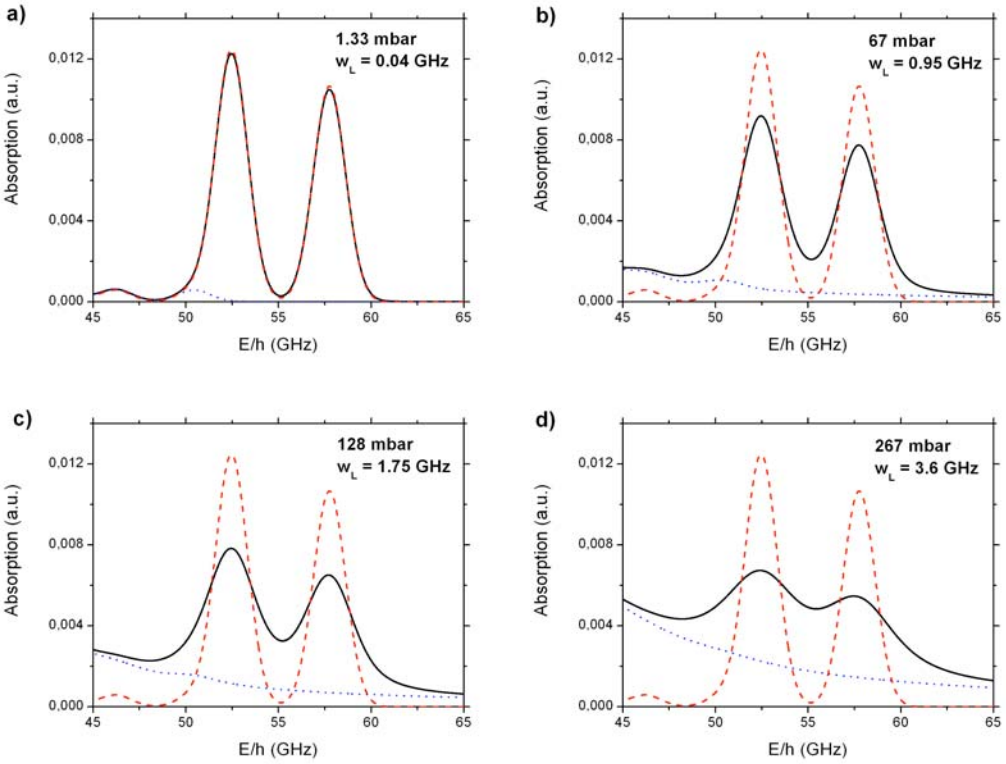

Fig. 3.10. Part of the σ^+ computed absorption spectra at 1.5 T for what was found to match experimental conditions at a) 1.33, b) 67, c) 128 and d) 267 mbar. The corresponding Voigt profiles (solid lines) were generated for T = 40 °C (w_G = 2.02 GHz) and w_L = 0.04, 0.95, 1.75 and 3.6 GHz respectively and are compared with Gaussian profiles (dashed lines) and the baseline contribution to the probe doublet (dotted lines) induced by the nearest transition lines. This baseline is mainly coming from the far wings of the f^{2p} and f^{4p} transitions but also contains two negligible transitions at 46.19 and 50.44 and GHz (see a)). The collision broadening is negligible at a) 1.33 mbar but clearly induces dramatic change in line shape and baseline at higher pressure.

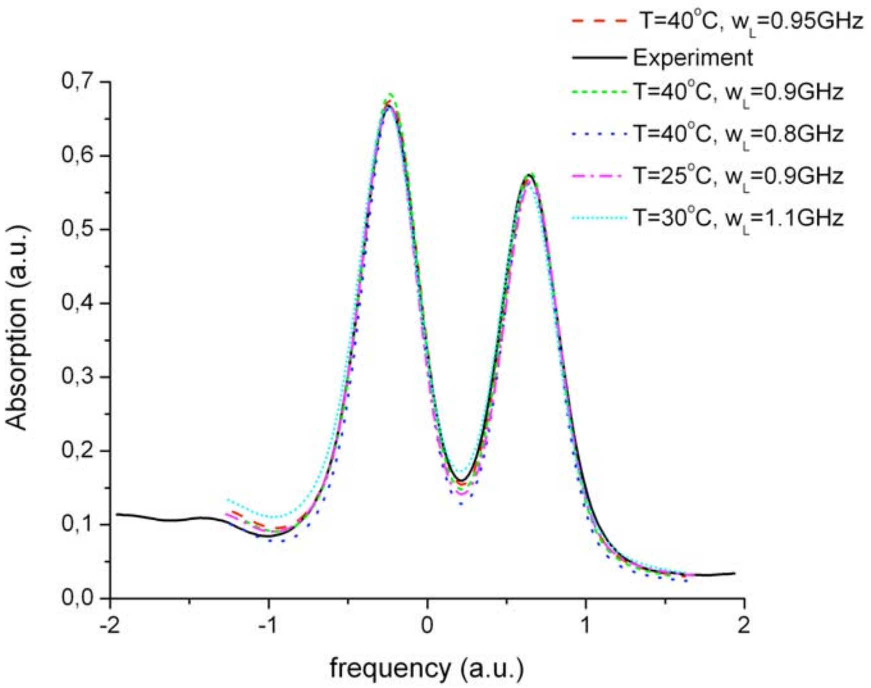

Fig. 3.11. Comparison between experimental σ^+ probe doublet at 67 mbar, M = 0 (solid line) and computed Voigt profiles for different w_G and w_L.

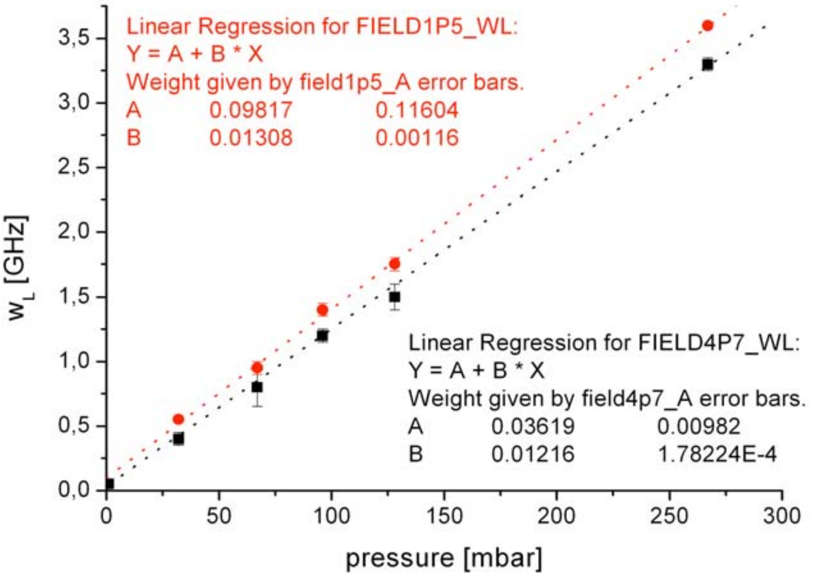

Fig. 3.12. Pressure dependence of Lorentz FWHM w_L of Voigt profiles found to be matching experimental data.

3.2.2. Measurement of apparent polarization M_{ap}

After acquiring one experiment, data analysis starts by exporting the data into a scientific graphing software (Microcal Origin) and checking that each of the six channels gives the expected behavior. Then, a “pick peaks” analysis is performed on the curve CH1/CH3 to get the multiscan peaks height and position. The signal at the output of LIA3, CH1, of the probe photodiode is divided by its integrated input CH3 to take into account for fluctuations of the transmitted intensity. Thus, CH1/CH3 is directly proportional to the probe absorption.

To correct the effect of the slanted baseline induce by f^{2p} and f^{4p} on the peak ratio, Pierre-Jean Nacher developed a new Fortran program called fitpeaksHib.exe. This program needs two input files: the CH1/CH3 time evolution and a second file containing the time at which pump is switched on, which transition is scanned just after, the theoretical ratio of the transition at M = 0 (r_{theo} = 1.1654 at 1.5 T and 1.1067 at 4.7 T) and the times of the absorption peaks. Four outputs files are generated after running the program. M0av.dat gives an average of the four first doublets at M = 0 before the pump laser is switched on. This file is used for the Voigt fitting described in the previous paragraph. In the second file fitHiB_base.dat, the program after having calculated a linear baseline between the edges of each probe doublet, writes down the baseline time evolution and the corrected absorption consisting of input data whose baseline was subtracted. An example of baseline correction at 96 mbar is presented on Fig. 3.13.

A peak fitting of the corrected data is performed around the estimated input time of each peak with a Gaussian shape and resulting fits are written in the third output file fitHiB_fits.dat together with the experimental data. Looking at this file gives a quick overview on whether something wrong happened during the program execution. This fit is also particularly useful when signal has a high noise level (specially at 4.7 T due to poorer acquisition scheme). Finally, the fourth output file fitHiBMst.dat contains values of peak ratios and its inferred apparent polarization M_{ap}. Ratios and M_{ap} are computed at the average time of each pair t_{av}. During OP or decay, the procedure introduced in § 4.3.2 of [Abb05a] is used to correct for the time difference between the peaks in a pair. If we define $S^i_{-3/2}$ and $S^i_{-1/2}$ as the peak heights of the ith doublet recorded at respectively times $t^i_{-3/2}$ and $t^i_{-1/2}$, linear interpolations of $S_{-3/2}$ and $S_{-1/2}$ at t = t^i_{av} can be written:

$$S_{m_F}(t_{av}) = S^i_{m_F} + \frac{t^i_{m_F} - t_{av}}{t^{i+1}_{m_F} - t^i_{m_F}}(S^i_{m_F} - S^{i+1}_{m_F}) \text{ with } m_F = -3/2 \text{ or } -1/2 \qquad (3.3)$$

The linear interpolation is made with the following recorded doublet but can also be done with the previous one. In practice, the average of the two interpolations is used to calculate the experimental ratio of the ith doublet $r^i_{\exp}$ from which M_{ap} is deduced as follow:

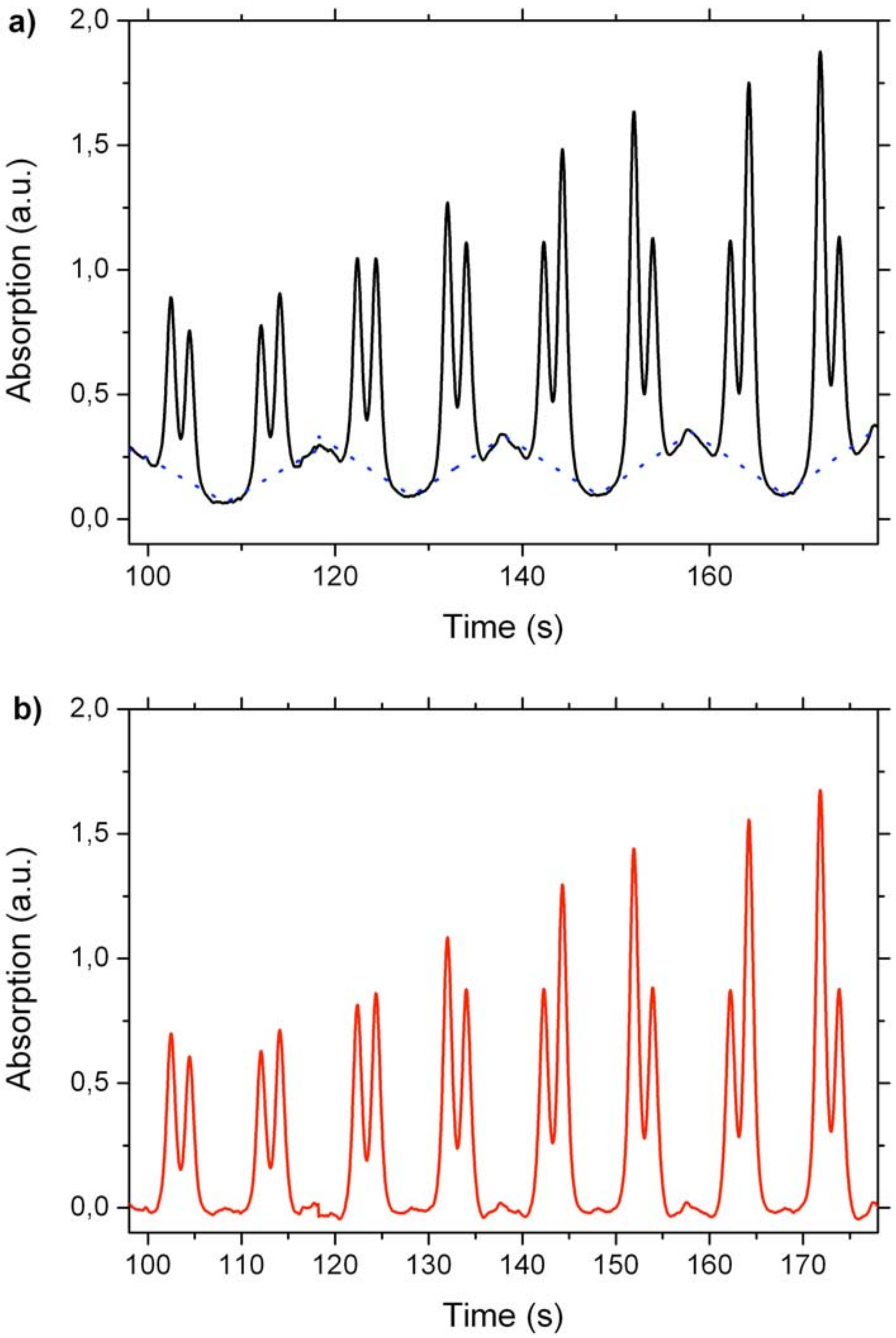

Fig. 3.13. a) Fragment of a recorded multiscan at 96 mbar (solid line) with the baseline computed by the Fortran program (dashed line). The 900 mW pump laser is switched on at t = 118 s. b) Corrected absorption data after subtraction of the baseline.

$$M_{ap}(t_{av}^{i}) = \frac{r_{\exp}^{i}/r_{theo} - 1}{r_{\exp}^{i}/r_{theo} + 1} \tag{3.4}$$

Values of t_{av}^{i}, $r_{\exp}^{i}$ and M_{ap} are not the only output data that can be found in fitHiBMst.dat. In a recent update of fitpeaksHib.exe program, relative density of metastable state $n_m/n_m(0)$ (where $n_m(0)$ is the average value during the four first recorded doublets at M = 0) were added and allow to see the relative evolution of metastable density during OP.

The data analysis is nevertheless not finished yet. M_{ap} is still not the true value of nuclear polarization and an additional correction has to take into account the crosstalk between the two partly resolved doublet lines at high pressure.

3.2.3. Main output parameters

When the two lines are partly resolved, a significant difference exists between the apparent and the actual polarization. In order to find the relation between them, a new option was added to the Voigt.exe program. Knowing w_L and w_G from the experimental data (see § 3.2.1), it is possible with this program to generate a theoretical multiscan with known input polarization decreasing linearly with time from 0 to -1 (Fig. 3.14).

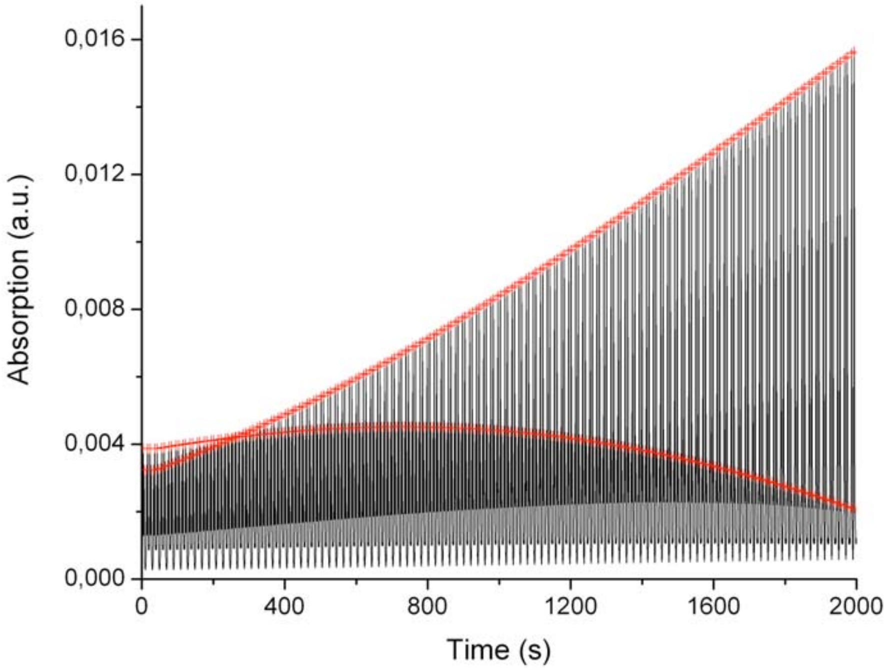

Fig. 3.14. Theoretical multiscan computed by Voigt.exe program and the pick peaks detection (red crosses) for T = 313 K and w_L = 1.4 Ghz. These conditions correspond to the experimental 96 mbar pressure at 1.5 T.

For each pressure and each field, such theoretical spectra were generated and underwent exactly the same data analysis as the one described in § 3.2.2. Thus, the M_{ap} found could be compared with the known input nuclear polarization and a linear fit of $M = f(M_{ap})$ brought us the last missing relation to obtain true M values. An example of such dependence is displayed on Fig. 3.15 for P = 96 mbar and B = 1.5 T.

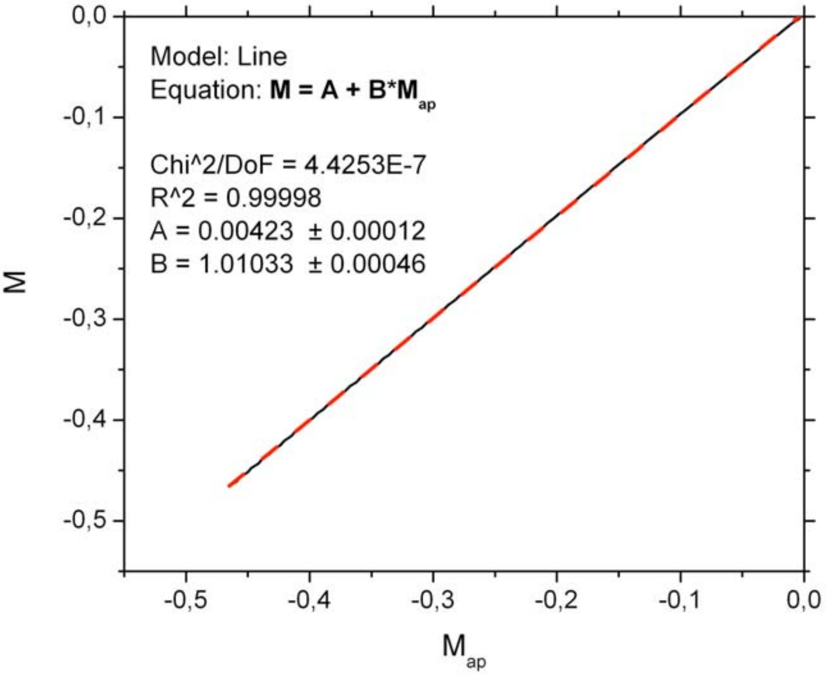

Fig. 3.15. Comparison of Map obtained by analyzing the multiscan of Fig. 3.14 and the real nuclear polarization M given as the input of Voigt.exe program. The relation $M = f(M_{ap})$ (solid line) is drawn only until M = -0.5 (no higher polarization was obtained during experiments at 96 mbar and 1.5 T) and a linear fit (Dashed line) gives us the required relation to deduce M from each experiment at this pressure and field.

At 4.7 T, relative differences between M and M_{ap} typically range from less than 2 % at 32 mbar to 18 % at 267 mbar, with M_{ap} systematically under estimating the actual steady state polarization M_{eq}. These corrections are specific to the 4.7 T field strength and they are observed to be much smaller at 1.5 T for which only a maximum of 0.5 % difference was found at 32 mbar and 1.1 % at 267 mbar. The explanation of this difference is that f^{2P} and f^{4p} transitions lines are closer from the probe doublet at 1.5 T than at 4.7 T, resulting in a stronger slanted baseline at 1.5 T that is fortuitously canceling almost all the effect of the crosstalk between lines in the doublet.

After having corrected and replaced M_{ap} by M in an experiment, it is then possible to plot the evolution of M(t) during optical pumping and decay and to deduce the main output parameters (Fig. 3.16):

- The steady state polarization M_{eq} is asymptotically reached at the end of the optical pumping process when the ME contribution to the time evolution of M is just balanced by the direct relaxation term $-\Gamma_g$ (see equation (1.22)). It is experimentally obtained by fitting M by an exponential decay before the pump is switched off (Fig. 3.16 a)).
- The relaxation time of nuclear polarization T_{decay} in absence of OP but with rf discharge on, is also deduced from an exponential fit of M after the pump laser is switched off (Fig 3.16 a)). This decay is accurately exponential and we define the corresponding decay rate $\Gamma_{decay} = 1/T_{decay}$.
- The build-up time constant t_b is defined as $1/\Gamma_b$ where Γ_b is the build-up rate of the polarization at the beginning of OP. It is calculated by performing a linear fit of $\ln(M-M_{eq})$ during the first seconds of OP (Fig 3.16 b)). The building process being not purely exponential in standard conditions [Bat11a], that is why it is not defined in the same way as T_1 during relaxation.
- M_{tot} is the total magnetization expressed in sccfp (standard cubic centimeter fully polarized). $M_{tot} = M \times V \times P$ with V the volume in mL (20 mL for sealed cell) and P the pressure in Atm.
- R is the production rate (see equation (1.10)).
- P_{abs} is the pump power absorbed at the beginning of OP. It is determined by looking at the difference of transmitted pump signal of CH0 during offset measurement and just after that the OP starts.
- $n_m/n_m(0)$ is the relative density of metastable atoms and is given by fitpeaksHib.exe program in the output file fitHiBMst.dat (see § 3.2.2).
- n_m is the density of metastable state and its calculation is explained in the next paragraph.

3.2.4. Derivation of the density of metastable state n_m

In this subsection, some theoretical considerations on the optical pumping rate and the pump laser transmission will lead to an experimental method of n_m determination from absorption measurements of the weak probe and pump beams performed before and after each acquisition. This method was developed recently by Pierre-Jean Nacher and Geneviève Tastevin in Paris to take into account the pressure broadening and a summary of an internal note written by them during exchanges between our two groups will be given here.

The optical pumping rate assuming a monochromatic transition was given in equation (1.15) of § 1.5.3. Practically, it corresponds to a single frequency probe tuned on C_8 at low field or on the two single transition lines of the σ^+ doublet at high magnetic field and in case of no crosstalk (low pressure limit).

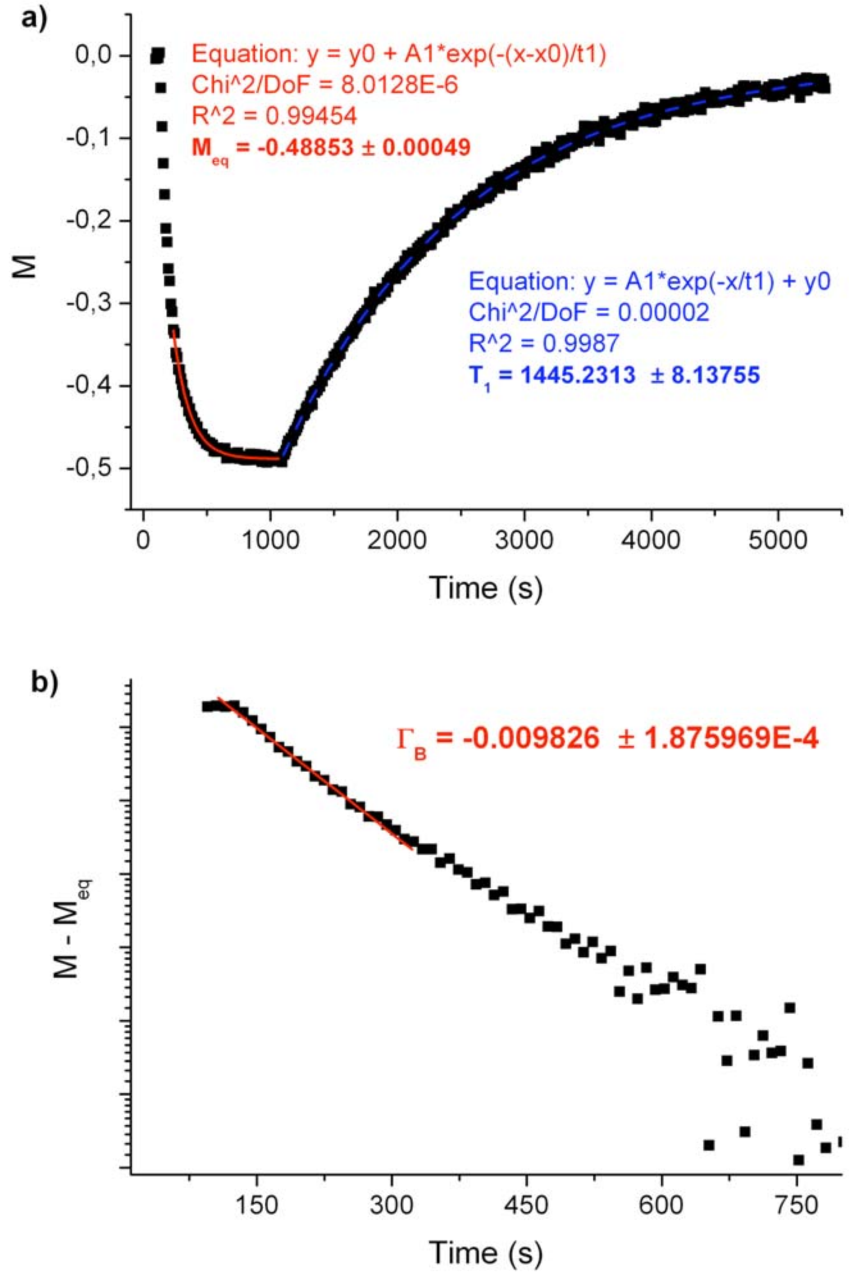

Fig. 3.16. a) Corrected values of nuclear polarization M and its evolution (squares) during one experiment at 96 mbar and 1.5 T with 0.5 W pump laser. The determination of steady state polarization M_{eq} = -48.9 % and the relaxation time T_{decay} = 1445 s is done by fitting an exponential decay of different parts of the curve (red solid and blue dashed lines respectively). b) Determination of the build-up rate Γ_b and time constant t_b = 101.8 s of nuclear polarization (red solid line) by fitting the time evolution of ln(M - M_{eq}) (squares).

In formula 1.15, the mean velocity $\overline{\upsilon} = 2\pi\Delta/\omega_{ij}$ is related to the Doppler width Δ:

$$\Delta = (\omega_{ij}/2\pi)\sqrt{2k_B T/m_{at}c^2} \tag{3.5}$$

where m_{at} is the atomic mass. Δ = 1.1875 GHz at 300K for ^{3}He and the corresponding FWHM $w_G = 2\Delta\sqrt{\ln 2} = 1.9773$ GHz. For the low pressure regime (Γ'/2 << 2πΔ) the integral of equation (1.15) can be easily computed and leads to a Gaussian variation of the average optical transition rate:

$$\overline{\gamma_{ij}} \approx \frac{\sqrt{\pi}\alpha f}{m_e\omega\Delta} T_{ij} I_{las} e^{-((\omega-\omega_{ij})/2\pi\Delta)^2} \tag{3.6}$$

The leading factor in equation (3.6) is:

$$\frac{\sqrt{\pi}\alpha f}{m_e\omega\Delta} = 3.7064 \times \sqrt{300/T} \times 10^3 s^{-1}/(W/m^2) \tag{3.7}$$

In one unit element of volume dV = dS * dz (with S the surface unit element perpendicular to the propagation axis z of the laser), the total number of atoms of the metastable state a_i addressed by the laser is $n_m a_i dV$. The absorbed laser intensity per unit length is then given by:

$$-\frac{dI_{las}}{dz} = \overline{\gamma_{ij}}\hbar\omega n_m a_i \tag{3.8}$$

In a cell with uniform density of metastable state a_i along the beam, the probe intensity exponentially decays with a characteristic absorptance length z_0:

$$I_{las}(z) = I_{las}(0)\exp(-z/z_0) \tag{3.9}$$

and after a total length L_{path} (for instance $L_{path} = 2 * L_{cell}$), the transmission factor is $T_{ra} = \exp(-L_{path}/z_0)$. In the case of our systematic studies at relatively high pressure, n_m is not uniform (see § 3.1.3) and the total transmittance provides an average value of n_m. From equations (3.8) and (3.9) we have:

$$\frac{I_{las}}{z_0} = \overline{\gamma_{ij}}\hbar\omega n_m a_i \tag{3.10}$$

By replacing the optical rate in expression (3.10) and by expressing z_0 with the transmittance, one obtains:

$$n_m = \tilde{n}\frac{-\ln T_{ra}}{L_{path}}\frac{1}{a_i T_{ij}\exp(-u_{ij}^2)} \tag{3.11}$$

$$\text{with } \tilde{n} = \left(\hbar\omega \frac{\sqrt{\pi}\alpha f}{m_e \omega \Delta} \right)^{-1} = 1.47105 \times \sqrt{T/300} \times 10^{15} m^{-2} \tag{3.12}$$

$$\text{and } u_{ij} = \left(\omega - \omega_{ij} \right) / 2\pi\Delta \tag{3.13}$$

If the initial assumption of an isolated transition is not valid, ie whenever several transitions are simultaneously excited from levels A_k with reduced detuning u_{kl} and line intensities T_{kl}, one can generalize equation (3.11):

$$n_m = \tilde{n} \frac{-\ln T_{ra}}{L_{path}} \frac{1}{\sum a_k T_{kl} \exp(-u_{kl}^2)} \tag{3.14}$$

Experimentally, it can correspond to probe scheme on C_9 at low magnetic field or f^2 and f^4 components at high B.

The Voigt.exe program when generating absorption spectrum actually computes the effective weights $\sum a_k T_{kl} \exp(-u_{kl}^2)$ for Doppler and Lorentzian widths. For these computations that do not rely on the low-pressure approximation of equation (3.6), it is convenient to separate equation (1.15) into 2 parts:

$$\overline{\gamma_{ij}} = K \times I_{Voigt} \tag{3.15}$$

$$\text{with } K = \frac{4\sqrt{\pi}\alpha f}{m_e \omega \Gamma'} T_{ij} I_{las} \times \frac{\Gamma'/2}{2\Delta} = \frac{\sqrt{\pi}\alpha f}{m_e \omega \Delta} T_{ij} I_{las} \tag{3.16}$$

$$\text{and } I_{Voigt} = \frac{\Gamma'/2}{2\pi^2\Delta} \int_{-\infty}^{\infty} \frac{e^{-t^2} dt}{\left(\Gamma'/4\pi\Delta \right)^2 + \left(\left(\omega - \omega_{ij} \right) / 2\pi\Delta - t \right)^2} \tag{3.17}$$

$$\text{where } I_{Voigt} \to \exp(-u_{ij}^2) \text{ when } \Gamma' \to 0 \tag{3.18}$$

which is indeed consistent with equation (3.6).

Using the equality $w_L = \Gamma'/2\pi$, the Voigt integral can be finally written:

$$I_{Voigt} = \frac{\sqrt{\ln 2}}{\pi} \frac{w_L}{w_G} \int_{-\infty}^{\infty} \frac{e^{-t^2} dt}{\left(\sqrt{\ln 2} w_L / w_G \right)^2 + \left(2\sqrt{\ln 2} \left(\omega - \omega_{ij} \right) / w_G - t \right)^2} \tag{3.19}$$

In practice, for M = 0, the average metastable density along the probe beam can be obtained using:

$$n_m = \tilde{n}\frac{-\ln T_{ra}}{L_{path}}\frac{1}{S(\omega/2\pi)} \tag{3.20}$$

in which S(ω/2π) is the value of the computed Voigt spectrum (from Voigt.exe program) for the probe frequency ω/2π and $\tilde{n}$ is the temperature-dependent value of equation (3.12). The experimental transmission T_{ra} = 1 – A is measured as described in equation (3.1) of § 3.1.3. For the pump laser, A was measured on the top of the pumping line f^{2m} using a correct set of filters to decrease the intensity to the 0.1 mW/cm^2 limit. For the probe laser, the absorption was generally measured on f^{2p} line but for high discharge conditions and when the transition was saturated, A was taken on the highest transition line of the σ^+ doublet. A summary of the S(ω/2π) values used at 1.5 T for the calculation of n_m is displayed in table 3.1.

Pressure (mbar)	Temperature (K)	w_L (GHz)	$S(f^{2m})$	$S(f^{2p})$	$S(A_2^p)$
1.33	313	0.01	0.18529	0.24692	0.012413
32	313	0.55	0.15771	0.20551	0.01027
67	313	0.95	0.14104	0.18263	0.009188
96	313	1.4	0.1254	0.16261	0.008318
128	313	1.75	0.11511	0.15021	0.007828
267	313	3.6	0.07902	0.11249	0.006739

Table 3.1. Summary of the temperature and w_L used for generating Voigt spectra in Voigt.exe program for the different pressures of the sealed cells. For each spectrum, the S(ω/2π) values required for n_m calculation were measured with a pick peaks analysis on the top of the f^{2m}, f^{2p} and the highest transition of the σ^+ probe doublet (A_2^p).

3.3. Results:

3.3.1. At 4.7 T

As previously evoked in materials and method subsection, the experimental conditions at 4.7 T were poorer than at 1.5 T. Some of the acquisition channels of Fig. 3.8 and the offsets at the beginning of the acquisitions were not recorded, absorption measurement were done only at the beginning of the experiment and the rf discharge was for few cases not stable during all the acquisition that could last longer than 3 hours. That is why few acquisitions of these systematic studies are still the subject of exchanges between our group and Kastler Brossel Laboratory, mostly due to uncertainty on n_m values for the concerned experiments. A joint publication including all the data analysis theory of § 3.2 and complete results at 4.7 T is under finalization and will soon be published [Nik11] but for the present dissertation, only the main parameters M_{eq}, M_{tot}, t_b, T_{decay} and R will be discussed. For each pressure, six experiments were performed consisting of three different discharge conditions and three different pump powers (0.5, 1 and 2 W) realized on one of these three discharges. The sixth acquisition corresponds to an OP experiment on the f^{2p} transition but this case gave lower polarizations and will not be treated in this work. For clarity in data presentation and only for this chapter, the absolute values of M will be presented but no confusion should be done on the fact that the polarizations obtained are actually negative when pumping on f^{2m}.

Typical behavior of optical pumping at high magnetic field is displayed on Fig. 3.17 with influence of plasma characteristic on the left (P_{las} = 0.5 W) and influence of pump power on the right (at the same rf discharge). Fairly long decay times T_{decay} (500 - 2000 s) are obtained at 4.7 T in the high pressure cells in spite

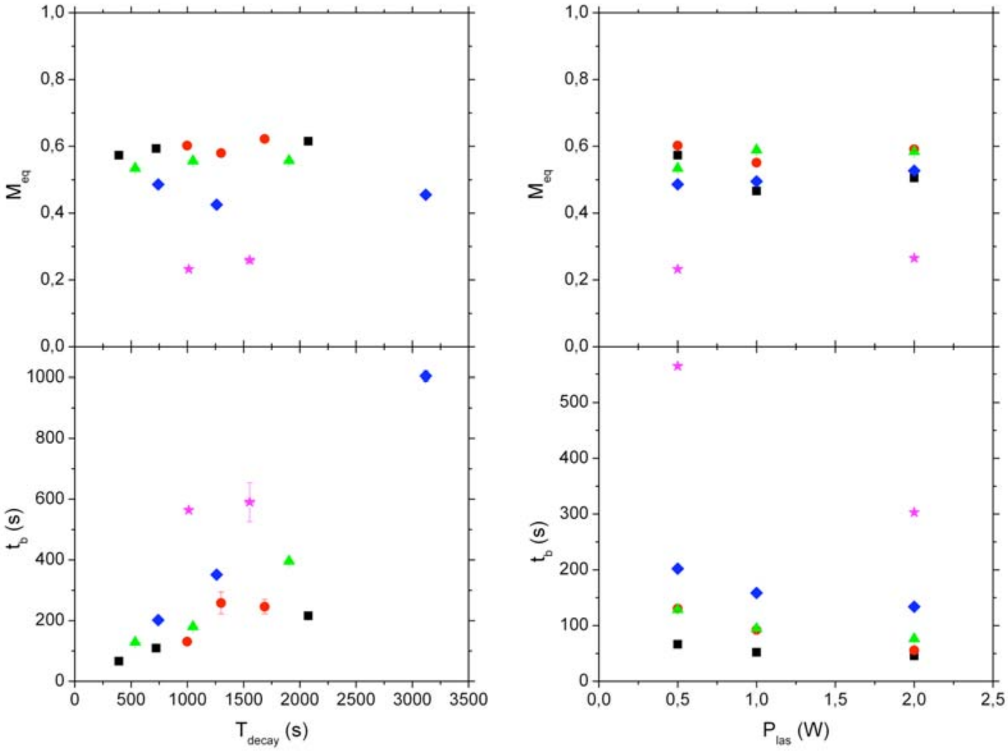

Fig. 3.17. Results obtained for 32 (squares), 67 (circles), 96 (triangles), 128 (diamonds) and 267 mbar (stars). Left: Steady-state polarization M_{eq} and build-up time t_b as a function of T_{decay} (P_{las} = 0.5 W). Right: M_{eq} and t_b as a function of P_{las}. Only three acquisitions were done at 267 mbar due to the difficulty to obtain stable discharges at this pressure.

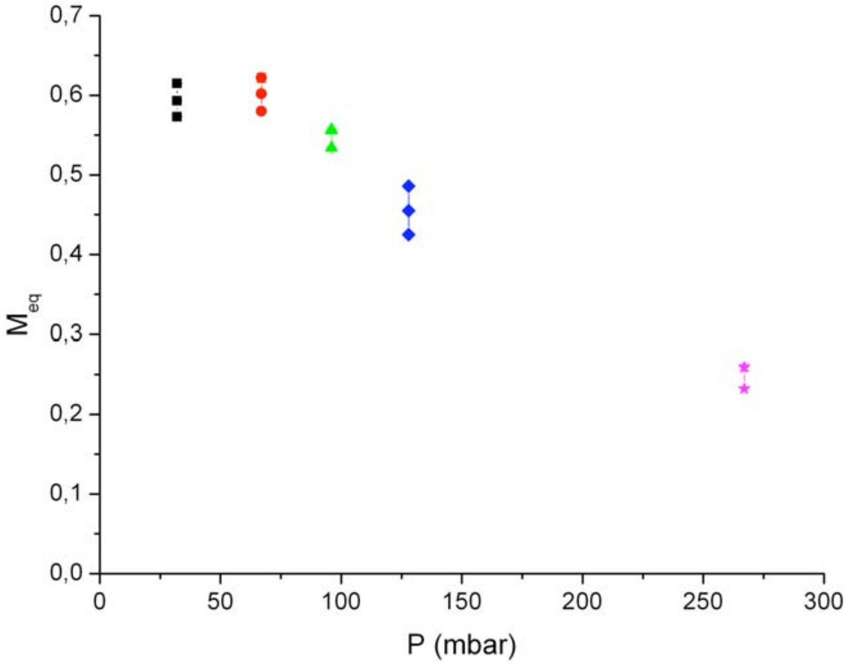

Fig. 3.18. Summary of the steady-state polarization obtained in the different sealed cells and for 500 mW of laser power.

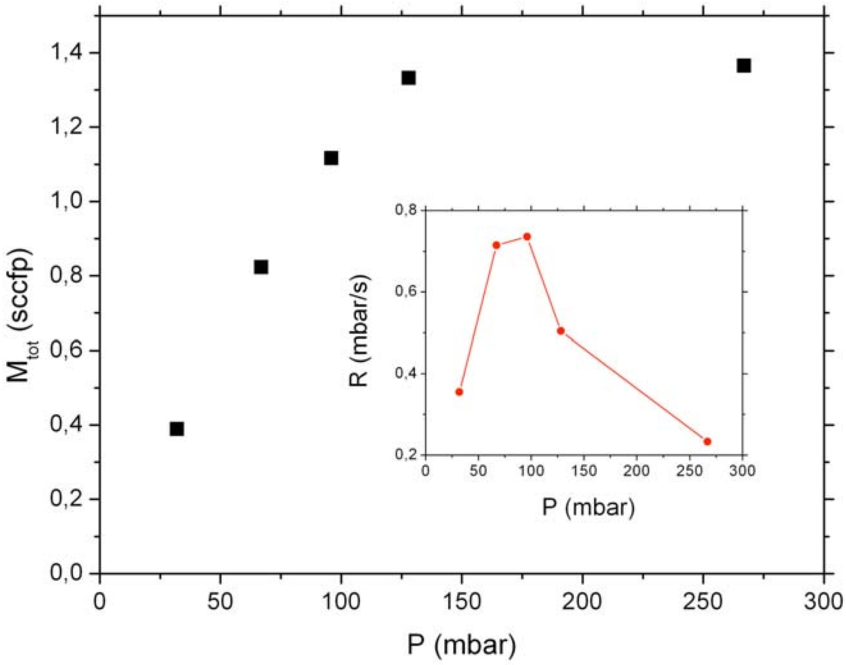

Fig. 3.19. Best values of total magnetization M_{tot} (squares) obtained for each pressure. In comparison, the evolution of the best production rates R is displayed in insert (circles).

of the much higher rf power needed to sustain stable discharges and to reach a significant metastable atoms density. This is similar to what was observed already at 1.5 and 2 T in [Nik07] in the same cells. M_{eq} does not seem to be highly dependent on the discharge intensity although it systematically decreases for really high discharge, when T_{decay} starts to be of the order of t_b. On the other hand and regardless of pressure, t_b increases monotonically with T_{decay}, illustrating a decrease of the metastability exchange collision rate with lower n_m. The range of build-up time values (from 66 s at 32 mbar and high discharge to 590 s at 267 mbar and low discharge) is much higher than in low field standard conditions. A closer look to the 32 and 67 mbar values obtained at 0.5 W shows an increase by a factor of two compared to the values obtained in the same cells at 2 T and by a factor of ten with 0.45 T results [Nik07]. This is a clear effect of hyperfine decoupling happening at high magnetic field and slowing down the transfer of electronic orientation to the nucleus (see § 1.4). The plot on the top right of Fig. 3.17 shows that a laser power of 0.5 W is already sufficient to obtain high nuclear polarization. Increasing P_{las} to 1 W or more does not reach higher polarization (it will be shown in next subsection that it can actually even lower the M_{eq} values), but it is still advantageous for shortening the build-up time.

Let's consider now the results at 0.5 W. On figures 3.18 and 3.19, the evolutions with pressure of the steady-state polarization and total magnetization respectively are displayed. As expected, M_{eq}, although reaching a value of 60 % never obtained at 67 mbar and 26.5 % at 267 mbar, systematically decreases with pressure due to the increase of relaxing collisions (see § 1.3) but the total magnetization M_{tot} shows the opposite tendency. For $P < 96$ mbar, M_{tot} increases fast due to a greater amount of atoms and a polarization quite constant. But for higher pressure, M_{tot} reach a flat plateau around 1.4 sccfp for which the increase of gas number density compensates for the decrease in MEOP polarization. In insert of figure 3.19, a comparison is displayed with production rate values. If R follows the same trend than M_{tot} at low pressure, an additional factor makes it dramatically falls down for $P > 96$ mbar. This factor is the lengthening of build-up time values at high pressure and the fact that the Gaussian beam shape is not suited for high pressure OP. It will be shown in the next subsection that results are different in the case of 1.5 T experiments with the use of axicons (see § 3.1.3).

However, the main motivation for performing these experiments at 4.7 T was not to investigate the production rates and possible applications of MEOP at this field strength, but to complete the systematic studies started in our lab at 0.45 T and to see the influence of the magnetic field on M_{eq} values. In figure 3.20, a summary of this evolution with chosen values of M_{eq} for 32 and 67 mbar cells obtained at fixed pump power (0.5 W) is displayed. After an almost linear increase of the steady state polarization with magnetic field up to 2 T, a plateau is reached and a limiting value of 62 and 60 % for 32 and 67 mbar respectively, is achieved. As shown in insert, the corresponding production rates drops also linearly with B. The linear fits provide the slope values equal to -0.101 and -0.064 mbar/(s*T) for 32 and 67 mbar respectively.

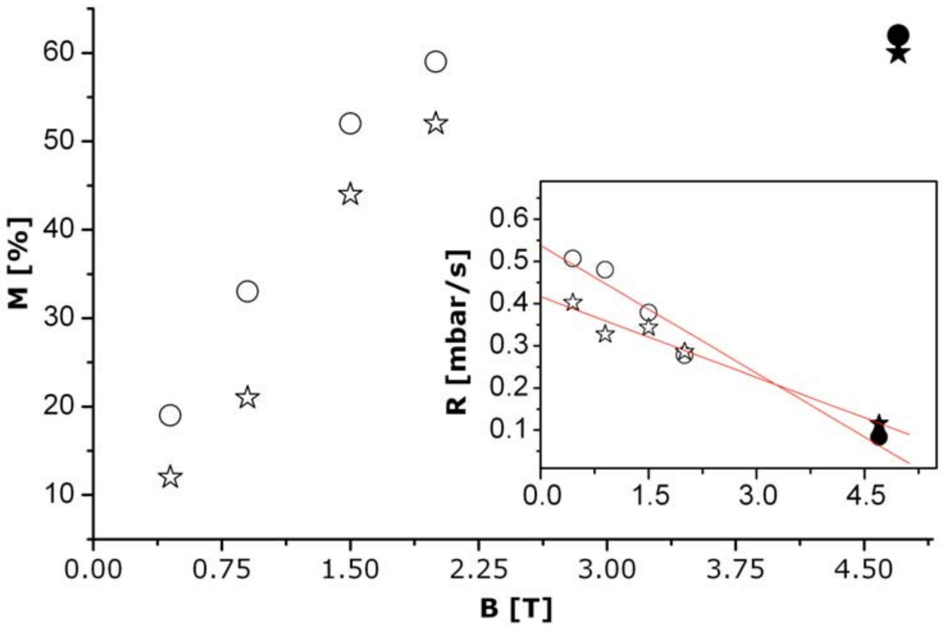

Fig. 3.20. Steady-state polarization M and production rates R (insert) as a function of magnetic field B in the 32 mbar (circles) and 67 mbar (stars) cells at fixed pump laser power (0.5 W) and weak rf discharge. The open and filled symbols represent the data from [Nik07] and from the present work, respectively.

Figure 3.20 illustrates the two positive and negative effects of hyperfine decoupling: M_{stat} increases with B due to the suppression of some relaxation channels but it also slows down the build-up process and limits its efficiency. It is nonetheless important to remark that, although only Gaussian beams of the pump laser were used for data shown on Fig. 3.20, they were produced by different sources that had slightly different linewidths and spatial FWHM. Additional results at 1.33 mbar, n_m values, OP experiments on f^{2p} and additional discussions and comparisons with results obtained at different magnetic fields can be found in complete dissertation of Anna Nikiel [Nik10].

3.3.2. At 1.5 T

In comparison with the results obtained at 4.7 T, the experimental scheme and the data analysis at 1.5 T allow us to describe the MEOP process more deeply and give us a broader range of tools to compare data with the recent model improved during the last years. After a first consideration of the plasma conditions, the main output quantities for a high field polarizer will be discussed. Finally, a closer look at some important parameters will bring us to a comparison, not exhaustive, with results obtained recently at low and high magnetic field.

3.3.2.1. Characterization of the plasma

The characterization of the plasma can be done in the absence of optical pumping light by measuring two parameters: T_{decay} and n_m. When the rf intensity of the discharge is raised up, more power is transferred to the atoms in the sealed cell, resulting in an increase of collisions and atoms in excited states. This leads to a higher density of metastable atoms in the plasma yielding a more effective OP process but it also shortens the decay time of nuclear polarization and consequently M_{eq}. That is why a compromise has to be found and the product n_m*T_{decay} to be maximized.

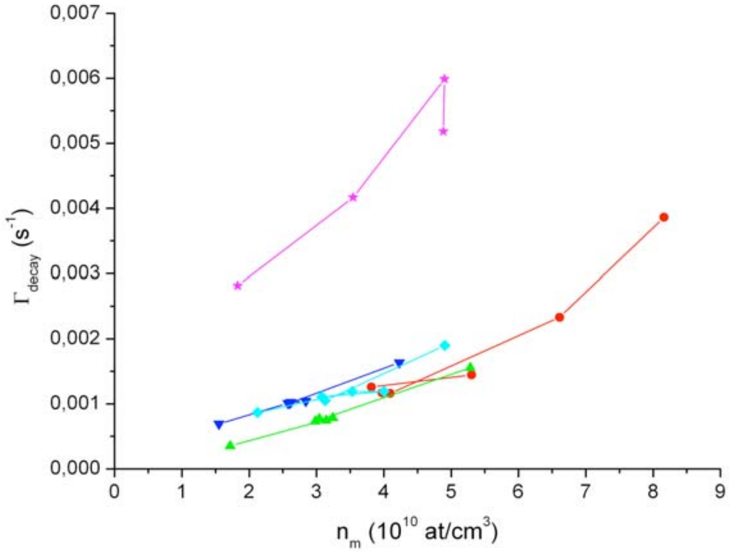

Fig. 3.21. Compiled decay rates $\Gamma_{decay} = 1/T_{decay}$ obtained at 1.5 T in the discharge as a function of metastable densities measured at M = 0 with a weak pump beam before and after experiments. The results are sorted in function of the pressure: 32 mbar (circles), 67 mbar (triangles), 96 mbar (reversed triangles), 128 mbar (diamonds) and 267 mbar (stars).

On figure 3.21, a good correlation can be observed at each pressure between $\Gamma_{decay} = 1/T_{decay}$ and n_m and a systematic increase of the decay rate with n_m. T_{decay} values range from 50 s at 1.33 mbar (not represented on Fig. 3.21) to almost 2800 s, which is the same order of magnitude than at 4.7 T. The surprising short values at 267 mbar compare to the rest of the results come from the fact that we had to use really high intensities to sustain discharge in this cell. The discharge was also not stable in these cases, explaining the non reproducibility of the results between two experiments done almost in the same conditions for the 267 mbar curve. T_{decay} has long been the key parameter that characterized the plasma and determined M_{eq} when only weak sources were available for OP but it is easier now to use n_m to compare experimental conditions between experiments performed at different fields, pressures and by different groups. It is indeed interesting to compare Fig. 3.21 with similar figures obtained at low (Fig. 6.4 and followings of [Bat11b]) and high magnetic field (Fig. 4.8 of [Nik10]). Beside the 267 mbar data points, similar trend is visible and the empiric definition of low and high discharge introduced in these works can be used. If the levels of discharge were experimentally chosen to correspond to three cases (close to ignition voltage, highly visible plasma and intermediate position), it is important to be able to sort these three configurations with a physical quantity. A weak discharge is then labeled by n_m value of the order of 10^{10} at/cm^3 and strong discharge to the level of 5.10^{10} at/cm^3 and above. Due to the ionizing Penning collisions (see § 1.3), n_m stays limited to the level of approximately 10^{11} at/cm^3 and this is also one of the reasons why, comparing metastable densities of different pressures with each other, it appears that the highest pressure does not yield the highest n_m values.

However, in identical plasma conditions, a different value of n_m can be inferred when the pump or the probe light transmission is used, in spite of their comparable path length ($L_{path} = 2*L_{cell}$). On figure 3.22, the n_m values obtained with the probe beam (left) show great discrepancies over the pressure range compare to the n_m deduced from the pump (right). The reason is that, as it was shown in § 3.1.3, the density distribution of metastable atoms is not homogeneous at high pressure. The probe beam is more sensitive to this variation than the pump beam because of its non parallel path with the cell axis (see Fig. 3.1). The probe is averaging the metastable atoms density across the cell by entering from one edge, passing through the center where there is almost no absorptance at high pressure, and going out from the second edge of the cell. This is the reason of really small n_m values obtained for 128 and 267 mbar cells and that is why all results will be discussed in the following by using exclusively the n_m values obtained with the pump absorption measurements that are better suited for describing the OP process.

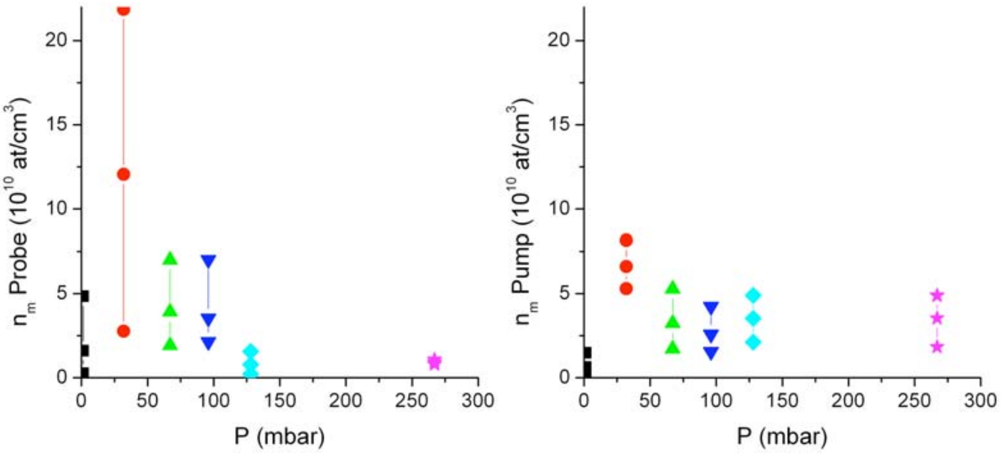

Fig. 3.22. Comparison of metastable atoms density averages along the path of a weak probe beam (left) and a weak pump beam (right) for different pressures. Three different discharges were tested for each pressure.

3.3.2.2. M_{eq}, Γ_b, R, M_{tot}

The main motivation for repeating MEOP studies at 1.5 T was to test the pair of axicons at higher pressure and to find the best parameters and see which efficiency could be expected for building a high field polarizer. This is discussed in details in this subsection.

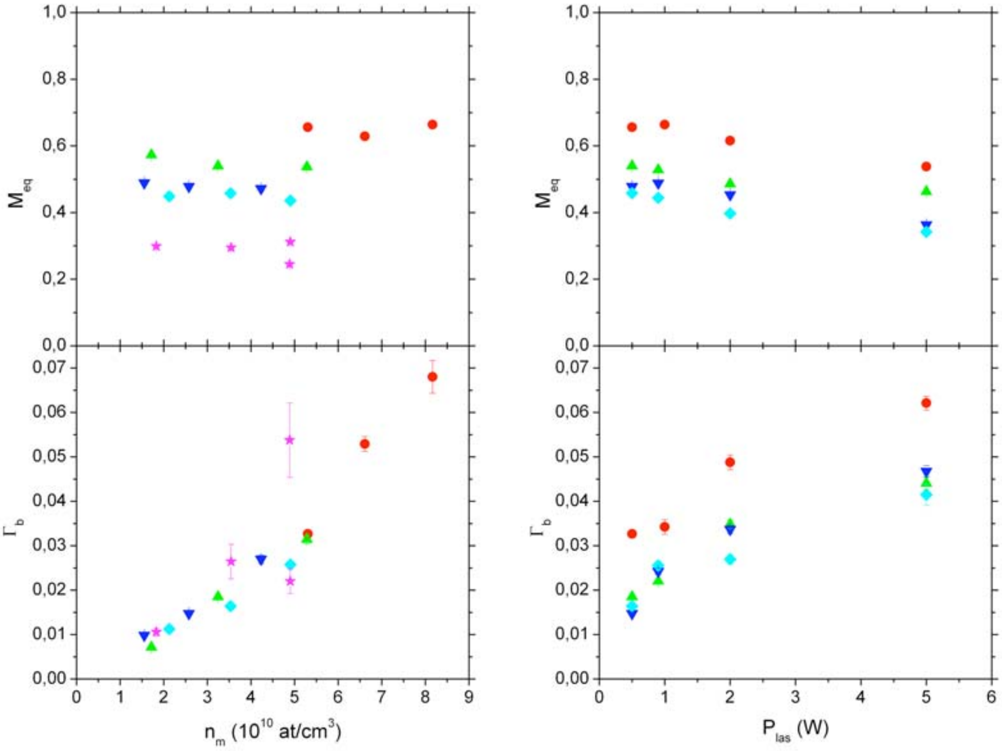

Fig. 3.23. Results obtained for 32 (cirlces), 67 (triangles), 96 (reversed triangles), 128 (diamonds) and 267 mbar (stars). Left: Steady-state polarization M_{eq} and build-up rate Γ_b as a function of n_m (P_{las} = 0.5 W). Right: M_{eq} and Γ_b as a function of P_{las}. The influence of laser power was not performed at 267 mbar due to the difficulty to obtain stable discharges at this pressure.

Figure 3.23 is similar to Fig. 3.17 at 4.7 T except that n_m replaces T_{decay} to characterize the discharge and that Γ_b was preferred to t_b to describe the build-up process. The left bottom graph shows that a strong and similar correlation between Γ_b and n_m exists at all pressures. The build-up rates roughly scale with the metastable density inferred by the pump, as expected, because moderate saturation of light absorption occurs at 500 mW, and this is validating the choice of n_m pump made in the previous paragraph for defining the discharge. The n_m values for the 32 mbar cell show that a strong discharge was always obtained at this pressure and might explain why such important polarization (66.4 %) was obtained (top left). Like for 4.7 T experiments, M_{eq} values is not depending too much on the discharge conditions, although it seems (apart from the 32 mbar cell) to decrease systematically by a few percents for high discharge conditions. But it is not comparable with the loss of polarization inferred when using 5W of laser power (see top right plot of Fig. 3.23). The decrease actually starts already for the 2 W data points but for 5 W, the polarization falls down from 66.4 to 53.8 % at 32 mbar, 54 to 46.3 % at 67 mbar, 48.8 to 36.3 % at 96 mbar and 45.8 to 34.2 % at 267 mbar (for the same discharge condition at each pressure).

On the other hand, using more power increases of course the build-up rate (see correlation on the bottom right plot of Fig 3.23) but the Γ_b values reached are on the same level as the one obtained only by increasing the level of the discharge. And this will be the main conclusion from Fig. 3.23, one should favor high power discharge for building a high-field polarizer rather than using phenomenal laser power. As a last remark on this figure, results of 1.33 mbar cell are not displayed because of systematic inconsistency in the obtained values (long t_b; Γ_b and M_{eq} independent of P_{las}; really small n_m), raising up the question of conception problem with this cell. It is important to notice that it was already the case to some extent at 4.7 T. However, M_{eq}, M_{tot} and R values obtained at this pressure are displayed in the next figures.

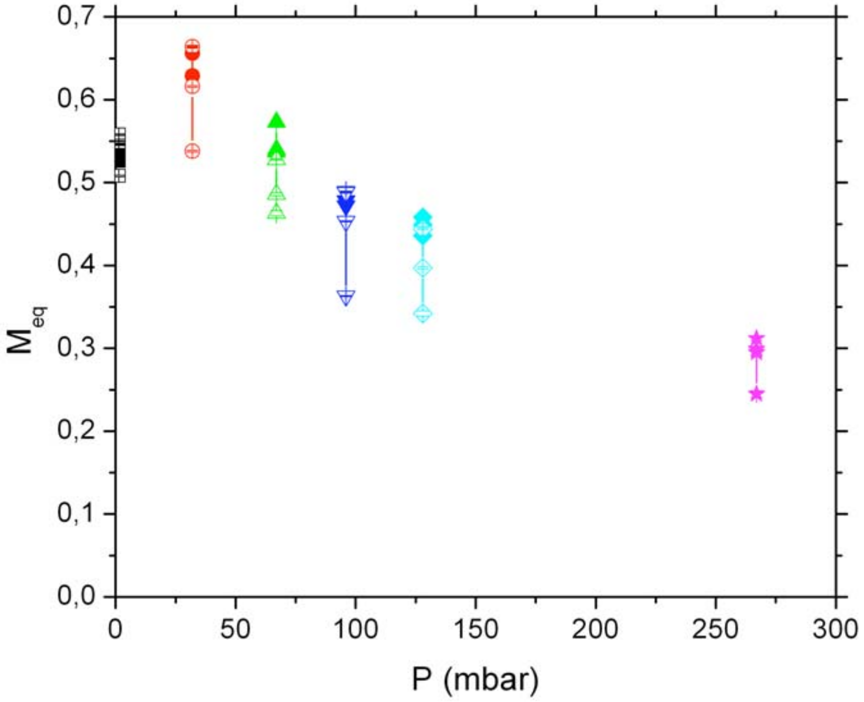

Fig. 3.24. Summary of the steady-state polarization obtained in the different sealed cells. Squares: 1.33 mbar, circles: 32 mbar, triangles: 67 mbar, reversed triangles: 96 mbar, diamonds: 128 mbar and stars: 267 mbar. Filled symbols were obtained with 500 mW of laser power and open symbols with 1, 2 and 5 W.

On Fig. 3.24, a compilation of all steady-state polarizations obtained for each pressure is presented. Compare to the results published in 2007 with a Gaussian beam and a spatial FWHM of 3.2 mm [Nik07], a spectacular 25 % increase of M is demonstrated at 32 (66.4 %) and 67 mbar (57.3 %). Like in Fig. 3.18, M_{eq} decreases with pressure but not as fast as it was at 4.7 T. If steady-state polarizations were higher at 67 and 96 mbar (effect of magnetic field decoupling), it is similar at 128 mbar and yields even higher value of 31.2 % at 267 mbar due to the benefic effect of annular beam shape. On the opposite, M_{eq} obtained at 1.33 mbar shows that the axicons are not suited for optical pumping at low pressure. The benefic effect of using axicons optics can also be seen on the total magnetization and the productions rate compiled on figure 3.25 (left and right respectively). Compare to 4.7 T, M_{tot} does not reach a plateau of 1.4 sccfp at 267 mbar because the increase in ^{3}He density is not completely balanced by a dramatic loss of nuclear polarization anymore.

But the second most important result of this study after the increase of steady-state polarization is the considerably high values of productions rate obtained in the right plot of Fig. 3.25. R is 4 times higher at 32 mbar compare to 4.7 T experiments and 15 times higher at 267 mbar. Two reasons can explain this feature: the hyperfine decoupling slowing down the process at 4.7 T and the use of axicons for 267 mbar cell that allows a perfect matching of annular shape and metastable atoms distribution in the cell, leading to a much more efficient pumping and to shorter build-up times values. Considering that R is only about 0.16 mbar/s in standard conditions, these results show the great potential to perform OP at high magnetic field and high pressure. The expected efficiency inferred from these data is at least ten times better than in low field MEOP, meaning that the same total magnetization inside an OP cell could be reached in a 10 times shorter duration using a higher pressure.

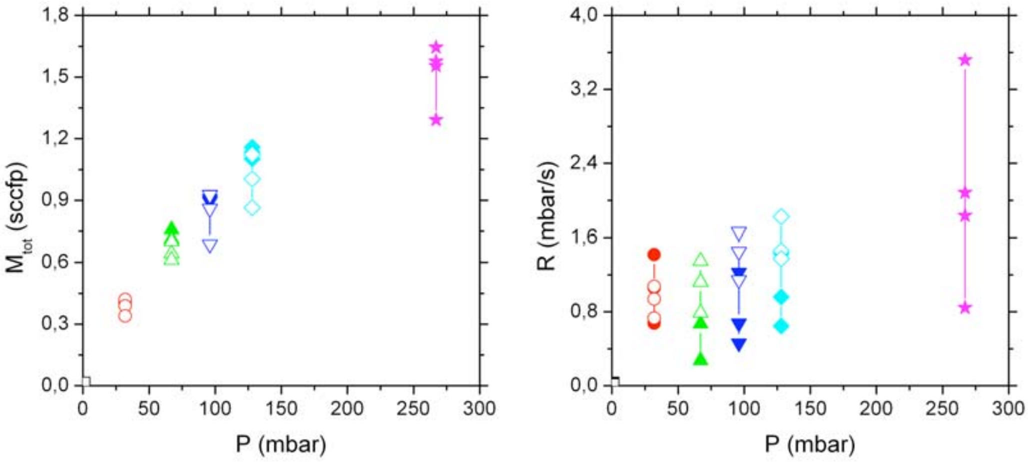

Fig. 3.25. Summary of the total magnetization values (left) and production rates (right) as a function of pressure. Filled symbols were obtained with 500 mW of laser power and open symbols with 1, 2 and 5 W.

The compression factor could also be greatly reduced at 267 mbar and the compression process eased. At last, a selection of the most promising acquisition at each pressure is summarized in table 3.2. A closer look at the build-up time column shows the second benefic effect of axicons evoked earlier, which is keeping a high build-up rate even at high pressure. That is why, contrary to 4.7 T experiment, R is not falling down at high pressure.

Pressure (mbar)	P_{las} (W)	n_m (10^{10} at/cm^3)	t_b (s)	M_{eq} (%)	R (mbar/s)
1.33	2	0.628	48.1 ± 0.6	55.8 ± 0.1	0.015
32	0.5	8.163	14.7 ± 0.8	66.4 ± 0.2	1.417
67	0.5	5.282	31.8 ± 1	53.7 ± 0.1	1.124
96	0.5	4.231	37.1 ± 1.3	47.2 ± 0.1	1.225
128	0.5	4.905	38.8 ± 1.1	43.6 ± 0.1	1.431
267	0.5	4.900	45.4 ± 5.8	31.2 ± 0.0	1.835

Table 3.2. Summary of P_{las}, n_m, t_b, M_{eq} and R for the most interesting data acquisitions obtained at each pressure.

3.3.2.3. Additional considerations and laser-induced relaxation

In this subsection, the behavior of few parameters recently studied and analyzed for the MEOP model developed in low field [Bat11a] will be compared with the present high field results in order to see to which extent this model can be applied to our results.

- **Variation of metastable atoms density $n_m(M)/n_m(0)$**

Variation of n_m during optical pumping was already reported in [Cou02] and it was shown at 1.5 T and for each tested pressure in [Abb05a] that n_m increases with M. It is attributed to the inhibition effect of polarization on Penning collisions. Indeed, the average value of the electronic angular momentum in the 2^3S state $<J^*_z>$ has an influence on the cross section of ionizing Penning collisions in the plasma. More recently, it was shown at low field that n_m exhibits a M^2 dependence during polarization decay (see Fig. 14 of [Bat11a]). Experimentally, it is possible in the absence of OP, when $<J^*_z>$ is coupled to M, to derive the relative variation of $n_m(M)$ from the absorption of a probe beam. In figure 3.26, the $n_m(M)/n_m(0)$ values coming from the output file of fitpeaksHib.exe program is presented for an experiment performed at 67 mbar with 0.5 W laser power.

During polarization decay from 53.7 to 0 %, a significant change of 20 % of n_m values is observed. On the right plot of Fig. 3.26, the M^2 dependence found at low magnetic field is confirmed. The same behavior was checked to agree at all pressures.

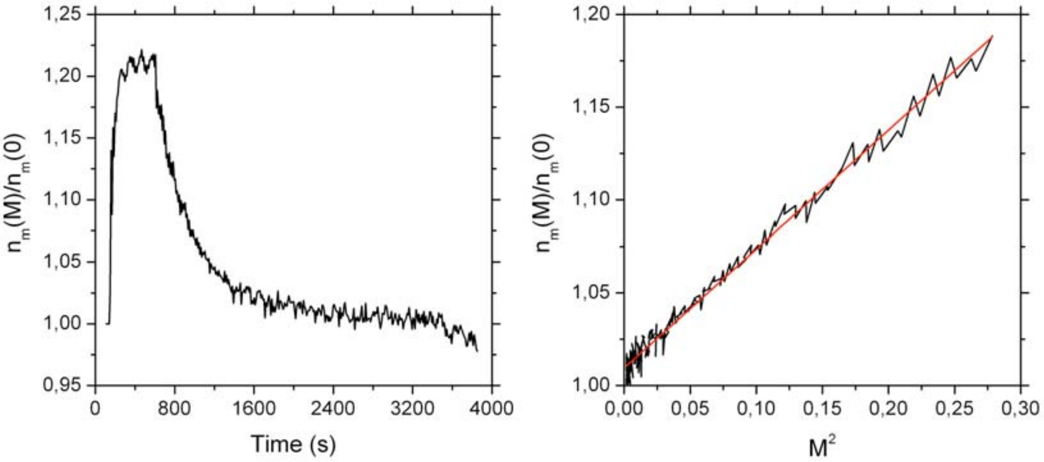

Fig. 3.26. Left: relative variation of n_m during an OP experiment at 67 mbar (the laser is switched off at t = 616 s). Right: M^2 dependence of relative density of metastable atoms for the corresponding experiment with linear fit.

- **Polarization build-up and $t_b(t)$**

When looking at first sight at the evolution of nuclear polarization M(t), one could think of a build-up process purely exponential like for the decay. In reality, it was proved in [Abb05a] that the build-up is more complicated and new tools were developed to study more precisely this feature at low magnetic field [Bat11a]. One of these tools consists of an additional Fortran program fitTbuild10.exe also written by Pierre-Jean Nacher from Kastler-Brossel Laboratory that requires as an input a two columns ASCII file containing the nuclear polarization time evolution during OP. It is generating as outputs, the dM/dt values and the resulting variation of t_b (see Fig. 3.27). The fact that the build-up is actually not exponential could be viewed already on Fig. 3.16 when representing $\ln(M_{eq}-M)$ as a function of time. The natural logarithm of the difference between M_{eq} and M is not purely linear and the build-up time value t_b inferred from a fit at the beginning of this curve and used in the results subsection is in fact $t_b(M=0)$. Looking at dM/dt and $t_b(t)$ in Fig. 3.27 gives more quantitative information about relative value difference in t_b for example. Build-up values clearly increases at the end of the polarization building. This behavior was observed at each pressure during these studies. Remark: in order to avoid confusion, it should be kept in mind that the experiments are different between Fig. 3.16 and 3.27 and that compare to section 3.2, M is here defined as positive (absolute value) as a practical convention.

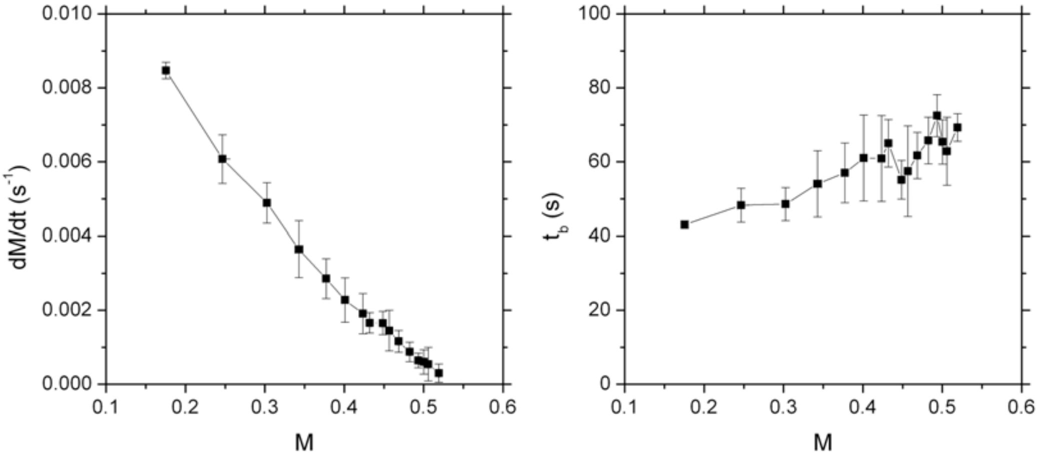

Fig. 3.27. dM/dt (left) and corresponding t_b values (right) given by the fitTbuild10.exe program for a MEOP experiment at 67 mbar and 500 mW pump power.

- **Laser-induced relaxation Γ_L**

Nevertheless, the most important phenomenon recently highlighted in [Bat11a] is the presence of an additional relaxation during OP, dependent on the laser power absorbed by the plasma discharge. This laser-induced relaxation rate Γ_L would be responsible for the systematic inconsistency between M_{eq} theoretical values computed by the MEOP model found in Paris and the experimental results. Theoretical values are obtained with a program based on rate equations similar to the ones presented in the first chapter and the complete detailed model is described in [Bat11b]. Existence of Γ_L was found by comparing the decay rates involved during OP and decay. The decay rate Γ_{decay} in presence of the discharge but in absence of OP is the sum of the intrinsic ground state relaxation rate Γ_g (see equation (1.21)) and the M dependent relaxation rate introduced by the metastability exchange collisions $\Gamma_{ME}(M)$. For a long time, when only weak arc-lamped and diode lasers were used for OP, the total polarization loss rate in the presence of OP Γ_R was found to be in the same order of magnitude than Γ_{decay} and MEOP model agreed with experiments at low magnetic field [Nac85]. But since high power lasers are commercially available, Γ_R is observed to be much larger. That is why Γ_L was introduced and defined by the following equation:

$$\Gamma_R = \Gamma_{decay} + \Gamma_L \tag{3.21}$$

To experimentally assess Γ_R, the following equation of the detailed balance of angular momentum has to be considered:

$$N_g \frac{dM}{dt} + n_m \frac{dM^*}{dt} = \eta\left(\frac{P_{abs}}{h\nu}\right) - N_g \frac{M}{T_{decay}} - n_m \gamma_r^S M^* \tag{3.22}$$

where η is the photon efficiency, defined as the ratio between the number of polarized atoms by the number of absorbed photons. In the formalism used in equation (3.22), the left part represents the stored angular momentum, the first term on the right part is the deposited angular momentum during OP and the two additional terms are the nuclear relaxation loss. As we have $n_m << N_g$, we can neglect the terms linked to 2^3S state and rewrite:

$$N_g \frac{dM}{dt} = \eta \left(\frac{P_{abs}}{h\nu} \right) - N_g \frac{M}{T_{decay}} \tag{3.23}$$

N_g is known from the filling conditions, P_{abs} can be deduced by scaling the channel CH0 with the offsets recorded at the beginning of the acquisition and M(t) is known. Only the quantum efficiency is unknown but it can be measured at the beginning of OP when M = 0:

$$N_g \left. \frac{dM}{dt} \right|_{M=0} = \eta \left(\frac{P_{abs}}{h\nu} \right) \tag{3.24}$$

In practice, the dM/dt values coming from the fitTbuild10.exe program are extrapolated to find the dM/dt(M=0). It was shown that the quantum efficiency is both M and P_{las}-dependent [Bat11a] but as a first approximation, it will be supposed constant in these experiments to determine the order of magnitude of Γ_L.

It was then possible to follow the evolution of the total polarization loss rate Γ_R for few experiments. The induced laser relaxation was then calculated by subtracting Γ_{decay} and resulting Γ_L values are presented in figure 3.28 as a function of the absorbed pump power. Γ_L seem to increase linearly with absorbed power like in low field [Bat11a] but the most important is that these rates are also higher than Γ_{decay} by at least one order of magnitude. It means that the induced laser relaxation is the dominant relaxation during MEOP experiment. It also confirms the tendency previously found at 1.5 T in [Abb05a]. A nice figure summarizing Γ_L obtained in different works can be found in [Bat11a] (Fig. 6.63) and shows that although exceeding Γ_{decay} at high absorbed power, Γ_L values are lower by one order of magnitude in comparison to low field situation.

This laser-induced relaxation is expected to be explained by an OP-induced plasma “poisoning” and for example by metastable $^3He_2^*$ molecules but the first results obtained by Bartosz Glowacz at 32 mbar and at low magnetic field, shows that the 340- fold increase of Γ_L was accompanied by only a 3-fold increase of the $^3He_2^*$ concentration [Glo11]. This excludes these molecules to be the main relaxation mechanism of MEOP in low field but additional investigation needs to be performed at higher field and higher pressures.

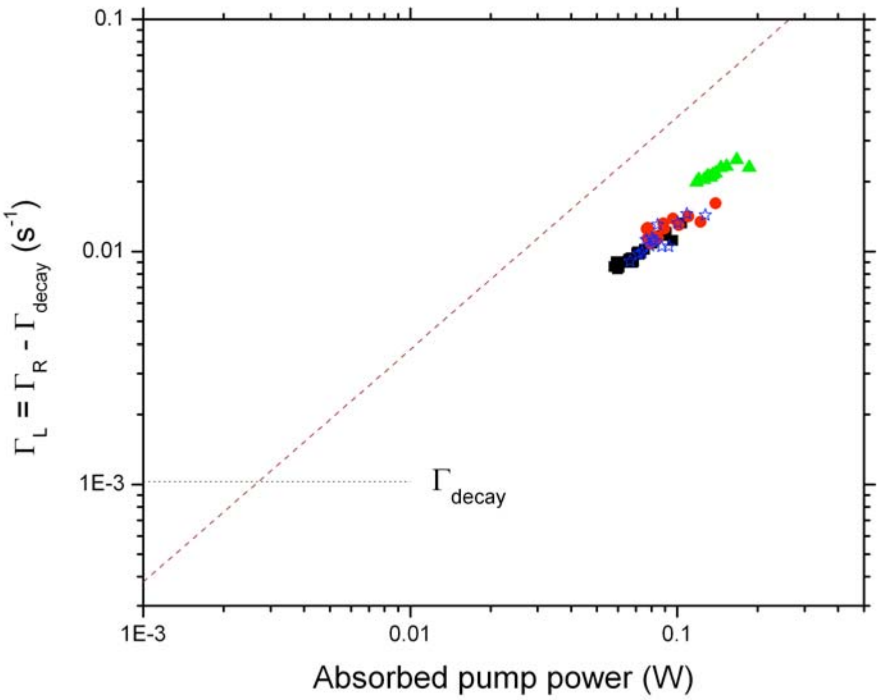

Fig. 3.28. Laser-induced relaxation rate $\Gamma_L = \Gamma_R - \Gamma_{decay}$, during OP experiments performed at 96 mbar (filled symbols) and different laser power (squares: 0.5 W, circles: 0.9 W and triangles: 2W) and 67 mbar with 500 mW (open stars). The horizontal dotted line represents the decay rate found for these experiments and the dashed line whose slope equals 1, a guide for the eye fitting all the values obtained at low magnetic field.

3.4. Outlook of the systematic studies at 1.5 T:

The main M_{eq} and R results of table 3.2 are summarized in figure 3.29. Compared to the one published in 2007, an increase of 25 % have been observed in the steady-state polarization and a factor of at least ten in the production rate compared to the best standard conditions. It also showed that, to increase the efficiency, MEOP should be performed at relatively high discharge and at moderate laser power (1-2 W, depending on the cell length and total absorptance). In order to build a high field polarizer, a compromise has to be found between high M_{eq} (low pressure) and high production rate (high pressure). Usually, the ^{3}He application gives the minimum required M_{eq} value that decides which pressure (or production rate) can be used. In lungs MRI, a reasonably good quality picture can already be taken with 300 mL of ^{3}He polarized at 30 %. But having 60 % polarization of course increases by a factor 2 the SNR or reduces by the same factor the required quantity of a gas that has become rare and expensive. When looking at Fig. 3.29, the best conditions seem to be reached around the pressure of 32 mbar for which surprisingly high R was obtained and for which M_{eq} is still above 60 %.

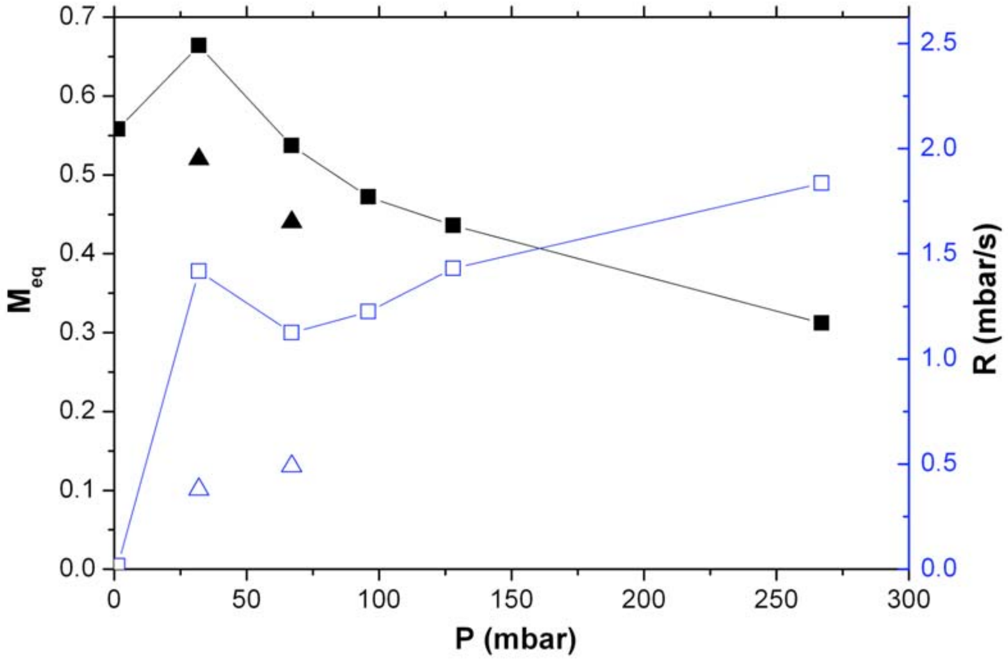

Fig. 3.29. Summary of the M_{eq} (filled symbols) and R (open symbols) obtained at 1.5 T in [Nik07] (triangles) and in the present work (squares).

In these first theoretical considerations, the benefic effect of axicons for a high field polarizer is not really clear. Actually, a comparison of laser shape influence on MEOP experiments was published in [Doh11a] and showed that at 32 mbar and in closed cells, the best configuration is to use a highly expanded beam like for low field conditions, to match a quite homogeneous distribution of metastable atoms in whole cell (see Fig. 3.5). But it will be seen in the next chapter that these expectations based on experimental data obtained in sealed cells could hardly be achieved in an open system and that the axicons were highly needed.

Chapter 4

Building a high field polarizer at 1.5T:

Motivated by the promising results of metastability exchange optical pumping obtained at high magnetic field and presented in the previous chapter, the decision was made to study the feasibility of building a high-field polarizer operating inside the most available MRI scanner at 1.5 T. The main advantage of having such a polarizer is to produce directly on-site the required amount of magnetization for lung magnetic resonance imaging performed shortly after the compression process. Production rates of polarization being higher at high B, the duration of accumulation in the storage cell is expected to be shorter. Moreover, the guiding field is already produced by the scanner and as the polarizer should fit inside its bore, the high field polarizer has to be compact and easy to transport and store. In a first part, preliminary tests with small open cells will be presented. Then, the complete design and construction of the high field polarizer will be detailed before showing the first results and pictures in the last part.

4.1. Preliminary tests in open cells:

4.1.1. Optical pumping cells

To see if the results of chapter 3 were reproducible in an open system and before starting experiments in a clinical environment, four small cells of different shape and diameter were produced by a glass maker, Mr Napiórkowski, from Gdansk. A picture of two of them is displayed in figure 4.1. Two different shapes were used. The first two cells were cylindrical with 11 cm length, 15 and 34 mm inner diameter. They appeared to not work properly because of multiple reflections and diffractions of the laser on the boarder of the optical windows. These windows, polished in our institute, were sent for assembling to Gdansk with the cylindrical body. During this operation, the border of the windows heated by the flame lost their flatness, which explains the optical aberrations. The problem was solved by ordering two new cells with the so-called bone shape used in the previous systematic studies. These two cells had the same length (11 cm) that fits the homogeneous volume of our superconducting magnet and similar diameter: 16 and 31 mm. At the input and output of each cell, valves using Apiezon L grease were tested to be leak tight with a turbomolecular pump.

Fig. 4.1. Picture of two open cells used for preliminary tests inside our superconducting magnet at 1.5 T. The first cell at the bottom of the figure has a cylindrical shape (diameter: 34 mm) whereas the top one has a bone-shape (diameter: 16 mm) and is connected through a glass-metal connection to a turbomolecular pump for cleaning purpose.

All cells underwent the following cleaning procedure:

- Ultrasound (US) bath with hot water + detergent (15’)
- US bath with hot water (two times 8’)
- US bath with gently heated aceton (15’)
- US bath with gently heated isopropanol (15’)
- Rinsing with pure ethanol and dry with nitrogen flow
- Connected to a turbomolecular pump (TMP) and heated during 6 h

Each cell was then connected to a gas handling system with relatively high vacuum ($6.3\ 10^{-8}$ mbar) and to a non magnetic plate inside the 1.5 T magnet.

4.1.2. Experimental procedure and gas handling system

The superconducting magnet producing the guiding field for this experiment was already presented in § 3.1.1 as it was used for the systematic studies at 1.5 T. Each open cell was lying on a similar optical plate as the one shown in Fig. 3.2 and including a pump laser and an optical detection of the nuclear polarization. The main difference of experimental procedure comes from the additional gas handling system (GHS) dedicated to ^{3}He supply and cleaning purpose.

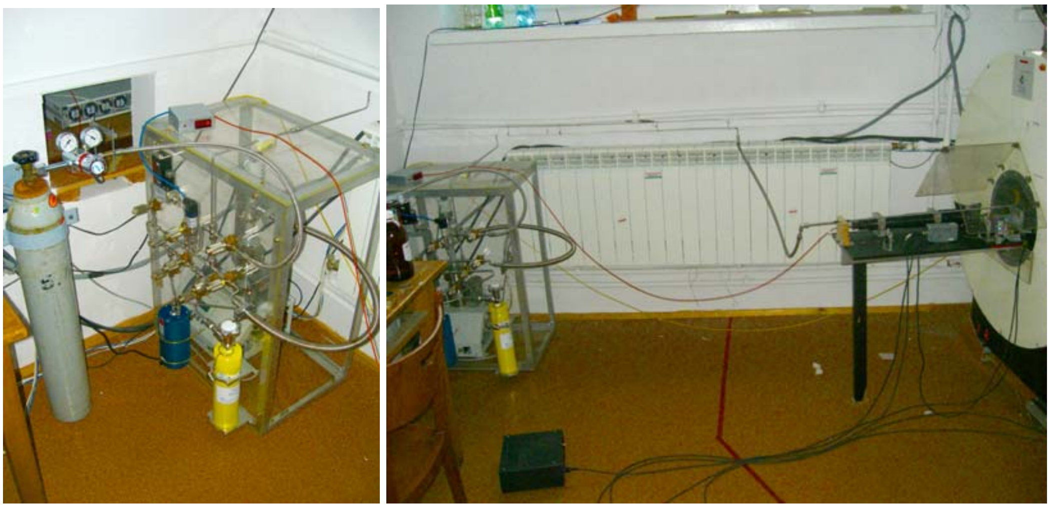

Fig. 4.2. Pictures of the gas handling system (left) used for the OP preliminary experiments in small open cells. On the right, a global picture of the 1.5 T magnet room shows the gas handling system connected to the optical pumping plate inside the magnet with 4 m of rigid (attached to the wall) and flexible non magnetic pipe made of stainless steel.

Most elements of the gas handling system being magnetic (^{4}He bottle, TMP and flow controller), it was located few meters away from the magnet and connected to the OP cell with approximately 4 meters of 6 mm outer diameter electropolished non-magnetic 316/316L stainless steel tube, 316L flexible tube from the FL series of Swagelok (Solon, Ohio, USA) and a metal to glass connection (G304-4-GM3, Cajon, Solon, Ohio, USA), (see Fig. 4.2). The GHS design is very similar to the low field polarizer one with a turbomolecular pump and a ^{4}He bottle for cleaning purpose and the same getter, filter and non magnetic valves. The only differences are a new pressure meter (model PTI-S-AC0-35AS, Swagelok…) and a flow meter (series SLA5800, Brooks Instrument, Hatfield, PA, USA). After building it, the GHS was heated for several hours with a hot air dryer (300 °C) for impurities in the walls of the connection pipes to be vacuumed by the TMP.

4.1.3. Purity issue

The first sign that the results obtained at 1.5 T would be not easily reproduced in open cells was quickly observed even before aligning the lasers, when the first attempts to switch on discharge were made. The plasma aspect inside these open cells was close to the one observed in high pressure sealed cell (at 128 mbar and more) although the pressure was reasonably low (on the order of 10 mbar). On figure 4.3, a picture of such plasma, located only close to the electrodes wired around the walls of the cell, is compared with plasma obtained in sealed cells. Moreover, the plasma color and spectral lines of the light emitted were not purely coming from ^{3}He atoms during the first attempts leading to the conclusion that a serious problem of purity was met. Such features were frequently matched in low field polarizers when a new system is starting to work for the first time or after that a leak has been discovered and repaired. It is thus not really surprising and is usually solved by vacuuming and heating the pipes and by rinsing several times the OP cell with ^{4}He plasma resulting from high power discharge. However, this cleaning process, although reducing greatly the weight of additional transitions in the visible spectrum of the plasma, did not improve the plasma distribution for pressure higher than 5 mbar, even in the case of the open cell with only 14 mm diameter for which getting homogeneous discharge at high pressure is easier.

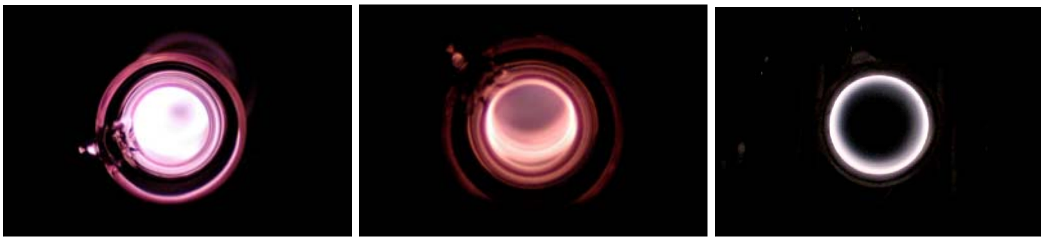

Fig. 4.3. Pictures of the plasma inside sealed cells (diameter 14 mm) at 1.33 mbar (left), 32 mbar (center) and open cell (diameter 31 mm) at 18 mbar (right) after conscientious cleaning process consisting of rinsing several times the cell with high plasma discharges in ^{4}He.

Although the vacuum inside the system seemed satisfactory (on the order of 10^{-7} mbar), the gas handling system was then tested with a helium sniffer leak detector that did not report any leaking issue. Additional cleaning attempts did not reach better plasma behaviors but the presence of impurities is certain. In Fig. 4.3, the pictures on the left and the center show the plasma distribution inside sealed cells filled with highly pure helium after the cleaning process described in § 3.1.2. Bright areas in the plasma indicate the location where radiative cascade contributes to the creation of metastable state. But the actual metastable density distribution results from the balance of creation, diffusion and destruction by various processes. That is why the map of n_m cannot be inferred directly from the plasma brightness. One example is the homogeneous n_m distribution measure in the 32 mbar cell (see Fig. 3.5) although plasma is much brighter closed to the cell walls. It was however not the case for the open cells as absorption measurement will prove it in the next subsection. Impurities in the helium plasma reduce the life time of metastable atoms by destroying them through collisions processes and if the quenching length becomes really small, the brightness tend to match the density distribution, which was the case in the open system. In the low pressure regime (around 1 mbar) of low field polarizer, collisions with impurities are rare and the lifetime of 2^3S atoms is long enough. But when the pressure increases, number of impurities increases and the quenching length is greatly reduced, giving to MEOP experiments a strong dependency upon the purity of the system.

4.1.4. Results

The purity problem was a great concern during these preliminary experiments and led to the conclusion that the pair of axicons had to be used. But the thickness of plasma distribution was so small for P > 5 mbar and with the additional effect of high B that almost no absorptance was measured if the pump or the probe beam was more than 3 mm away from the cell walls. In the probe configuration describe in Fig 3.1, the absorptance of the probe beam was close to be null. That is why the configuration of the optical setup was changed to obtain a better match between metastable atoms and laser path (Fig. 4.4). The probe beam was thus collinear to the magnetic field and passing through the OP cell back and forth on one side, close to the wall. The mirror directing the probe beam in the OP cell was then blocking one side of the pump beam, leading to a C shape.

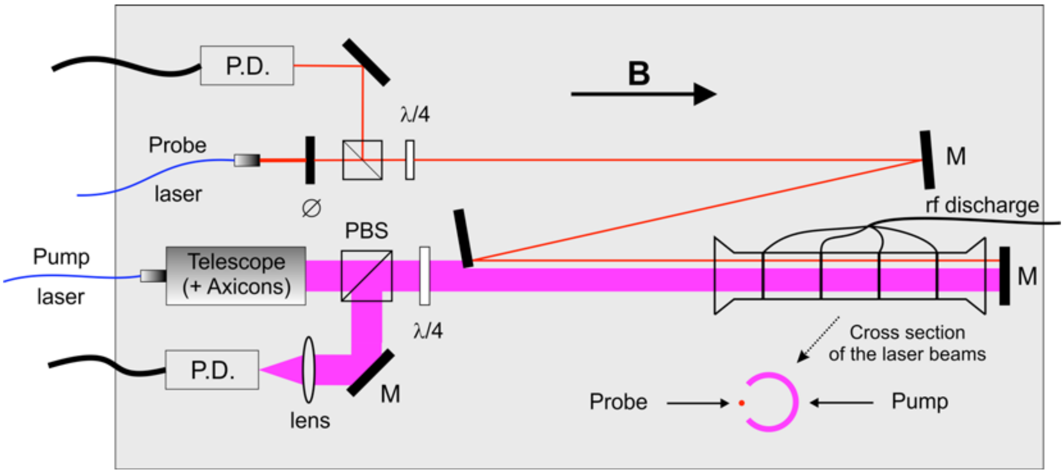

Fig. 4.4. Schematic of the optical setup used for experiments in open cells at 1.5 T. The valves and connection to the GHS are not represented on the scheme. Probe and pump laser beams are first circularly polarized by a polarizing beam splitter (PBS) and a quarter-wave plate (λ/4). A set of mirrors (M) makes them pass through the OP cell in parallel with the magnetic field (B) before being recorded by two photodiodes (P.D.). One part of the annular pump laser beam is blocked by the circular mirror used to transmit the narrow probe beam on the left side of the cell. A resulting C-shape of the pump is obtained.

The first two cylindrical cells were tested with this configuration but as explained in § 4.1.1, the boarder of the windows were not flat enough and many diffractions and reflections disturbed the few recorded acquisitions. That is why two new bone shape cells were ordered. Unfortunately, the 15 mm diameter one appeared to have a very small leak in a connection between one window and the main body. Special low vapor glue dedicated to high vacuum experiment was used but the results were unsatisfactory and the last cell was preferred to perform the experiments. All the M_{eq} and R values of the 31 mm diameter bone shape cell are summarized in Fig. 4.5 and compared to the results obtained in sealed cells.

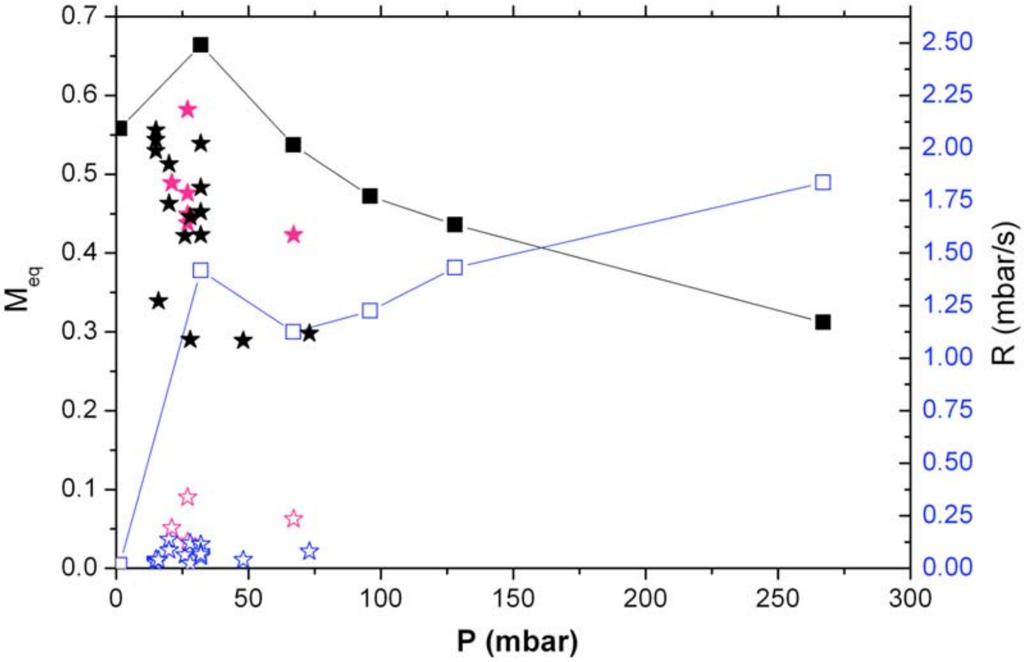

Fig. 4.5. Summary of the M_{eq} (filled symbols) and R (open symbols) obtained at 1.5 T in sealed cells (squares) and in a 31 mm diameter open cell (stars). Results obtained after a conscientious aligning of the beam are highlighted in red.

The results obtained were disappointing and confirmed the presence of impurities. Experiments at pressure higher than 75 mbar could not be performed due to a too small absorption signal of the probe beam yielding to a poor signal to noise ratio of the data. The total probe absorptance at the beginning of the OP P_{abs} showed the same tendency and was only on the level of 1 %. This led to steady state polarizations of only 30 to 50 % around 30 mbar and more dramatically to production rate 10 times lower than the ones obtained in sealed cells. The reasons of these small R values are the much longer build-up times values explained by smaller efficiency (absorptance) and a 5 times larger volume of gas to be polarized (it was 20 mL in sealed cell and around 95 mL in the 31 mm open cell). Thus, t_b could reach 200 s for only 15 to 30 mbar when it was only on the level of 15 s in 32 mbar sealed cell. Finally, a last attempt to perfectly align the pump beam with plasma discharge was made (highlighted in red in Fig. 4.5). It succeeded to increase pump absorptance to more reasonable values (5 to 20 %) and increased both M_{eq} and R values.

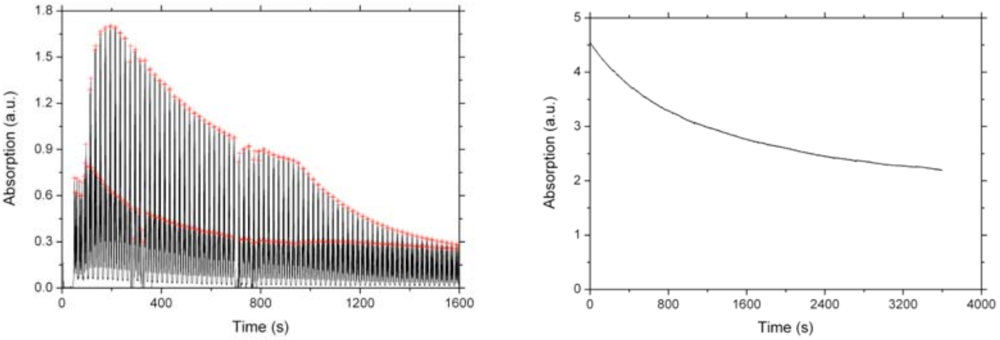

Fig. 4.6. Left: Absorption recorded during a multiscan acquisition of the probe doublet at 27 mbar. The pump laser was switched on at t = 86 s and switched off at t = 940 s. Although the ratios of the peaks induce a nice exponential build-up of the nuclear polarization, the total absorption decreases during the acquisition. Right: Absorption of a weak pump (channel CH0) tuned on f^{2m} transition. The decrease of absorption can not be explained by the OP process because of the small intensity used for this measurement.

The presence of impurities was also clearly visible when looking at the surprising behavior of recorded multiscan acquisitions. The acquisitions performed just after ^{3}He was renewed inside the cell showed trend displayed on the left plot of Fig. 4.6. The absorption decreased with time and eventually reached a more or less stable value for which the next acquisition was performed and gave lower steady-state polarization. It was confirmed with a decrease, sometimes by factor of two between absorption measurements with a weak probe beam before and after acquisitions. On figure 4.6, the worst cases are presented for a better understanding but the decrease of absorption during the duration of the acquisition was fortunately not always so important. The stability of the discharge during experiment was not raising up any question and that is why the most probable explanation is that these experiments are defecting from a problem of design. Having the GHS four meters away from the cell makes the cleaning of 4 mm inside diameter tubes and OP cell harder. When the gas is refreshed, absorptance is higher and acquisitions give reasonable results in the pressure range of 30 to 50 mbar, if the conditions of well aligned laser is matched. But impurities still contained in the walls of long pipes are probably desorbed and mixed with ^{3}He as the time goes on, which explains the decrease in absorptance and lower results.

In conclusion, these preliminary tests, although bringing much worse values of M_{eq} and R, were necessary because they highlighted the most important features to take into account when pumping at relatively high pressure and when building a high field polarizer. It showed that the purity of the system was the most important parameter to improve, that the future GHS system has to be as close as possible from the OP cell, that the axicons should be used, that MEOP should be performed in the pressure range of 20 - 60 mbar with high discharge and that the diameter of the cells should be reduced to improve the plasma density distribution across the cell as the absorptance seems to be the key parameter for an efficient MEOP.

4.2. High field polarizer design:

The systematic studies of the chapter 3 and the first tests in open cells of the previous section brought enough elements to start designing the first prototype of a high field polarizer. In this part of the dissertation, the different considerations and steps of the construction of the polarizer are presented in the chronological way it was achieved. It is starting with a simulation of the production and nuclear polarization that are expected to be achieved, before presenting the compression system chosen for the polarizer, describing in details the main design of the GHS and optical pumping plate and finally, the derivation of capillaries sizes for flow restriction is explained.

4.2.1. Flow considerations and expected production

Two modes of production can be chosen. The first one is called batch mode, consists in filling the OP cells with the desired pressure, optically pumping the ^{3}He until a chosen value of polarization and then compressing the gas into the storage cell, stopping the compressor, filling the cell again etc… It is the method used in Mainz for their large production facility [Bat05, Wol04] and has the advantage of having a fast increase of nuclear polarization during OP because it is averaging the dM/dt until the chosen polarization is reached. However, there are also many disadvantages linked to the compression step that needs to be fast and the frequency at which it should be done due to the number of times valves should be opened and closed. An approximation of the production that can be reached with this mode is given by the total amount of gas contained inside the cell (P*V) divided by $3t_b$ (for $M = 0.95 * M_{eq}$ or by $5t_b$ for $0.99 * M_{eq}$, etc). To this time should be added the time of compression and refilling of the OP cells. This solution seemed not appropriate in a high magnetic field environment where electromagnetic valves cannot be a-priori used and where the manipulator have restricted access to the magnet bore for manually opening and closing the valves.

The second mode that has been selected in this work is the continuous flow mode where the compressor is always running, and the valves from the ^{3}He reservoir to the storage cell remain open. In the following, simple approximations will be made to deduce the expected flow Q and polarization M that can be expected from the results previously obtained in sealed and open cells. As a first approximation, the flow and the steady state polarization in the OP cell will be considered constant and the build-up process purely exponential with a constant time t_b'. To take into account the slowing down of the process described in §

3.3.2.3 and as we want to reach high polarization value, t_b' will be taken equal to 1.4 times the build-up time at the beginning of OP t_b, which is a good average of the experimental results (see Fig. 3.26). In the steady-state situation, the total magnetization produced in a unit of time by OP and expressed in sccfp/min (standard cubic centimeter fully polarized per minute) is carried out by the compressor to the storage cell. We can then write:

$$\frac{dM}{dt}\frac{PV}{T} = QM \tag{4.1}$$

where P is in atm, V in mL, T = 1 (a normal temperature is assumed) and the atomic flow Q in scc/min. In addition, M can be written:

$$M = M_{eq}\left(1-\exp\left(-t/t_b^{'}\right)\right) \Rightarrow \frac{dM}{dt} = \frac{M_{eq}}{t_b^{'}}\exp\left(-t/t_b^{'}\right) = \frac{M_{eq}-M}{t_b^{'}} \tag{4.2}$$

By combining equations (4.1) and (4.2), the following simple equation linking the chosen flow with the cell dimension, build-up time and resulting polarization can be obtained:

$$M = \frac{M_{eq}}{1+\dfrac{Q\times t_b^{'}\times T}{PV}} \tag{4.3}$$

On figure 4.7, the polarization values derived from equation (4.3) and extrapolated from the M_{eq}, t_b, P and V obtained in sealed and open cells are

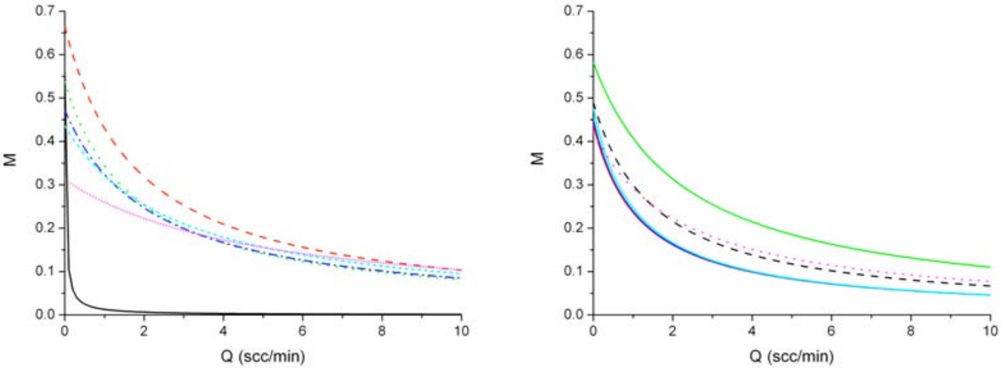

Fig. 4.7. Computed nuclear polarization from Eq. (4.3) as a function of the flow. Left: M inferred from the systematic studies performed at 1.5 T, using a cell volume of 20 mL and from the results of table 3.2 (black solid line: 1.33 mbar, red dashed line: 32 mbar, green dotted line: 67 mbar, blue dash dot: 96 mbar, cyan short dash: 128 mbar, magenta short dot: 267 mbar). Right: M inferred from the open cell data highlighted on Fig. 4.5 and using a volume of 95 mL (solid lines: 27 mbar, dashed line: 21 mbar, dotted line: 67 mbar).

presented. For this simulation, it is assumed that the experimental conditions would be exactly the same in the presence of a constant flow. In practice, it can be matched if well design capillaries are inserted at the input and output of the cell preventing impurities from diffusing from the storage cell to the OP cell and the polarized ^{3}He to diffuse outside the cell. Figure 4.7 shows that, except for the 1.33 mbar sealed cell, the Q-dependence of the polarization is actually not really different when considering sealed and open cells. The polarization at Q = 0 is of course higher in the case of sealed cell but each cell of 11 cm length seems to be able to produce more or less the same magnetization in a flow range of 2 to 10 scc/min. The dramatic effect of impurities that slows down the efficiency is actually hidden by the almost factor 5 difference between the volume of sealed cells (20 mL) and the open cell (95 mL). To fairly compare the two situations, it is better to use a common volume. This is done in figure 4.8 by taking an OP cell volume V of 1L corresponding to approximately 6.5 m of 14 mm diameter (sealed cell) and 1.3 m of 31 mm diameter (open cell).

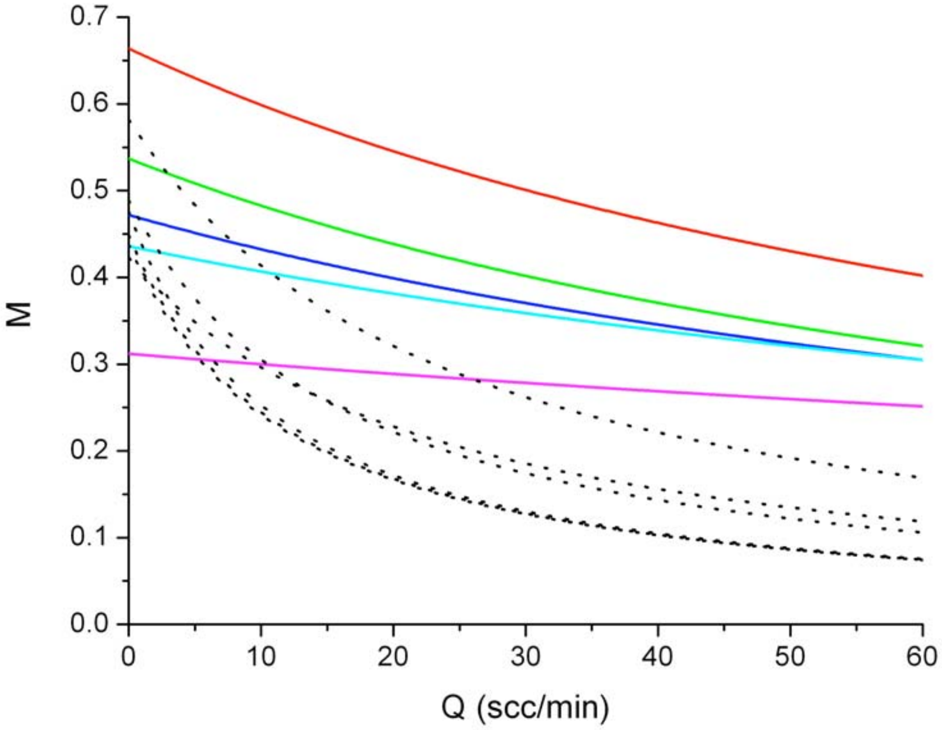

Fig. 4.8. Polarization derived from equation (4.3) with a fixed volume of 1L. Comparison between the closed cell configuration for different pressure (solid lines, values taken from table 3.2, the 1.33 mbar cell is not represented) and the open cell results highlighted on Fig. 4.5 (dotted lines).

The effect of longer t_b values is clearly seen on Fig. 4.8. For open cell simulation, the steady state polarizations are falling down much more rapidly with the increasing flow, reflecting the fact that for higher Q, ^{3}He atoms do not have the time to be fully polarized during their average time spent in the OP cell. This is a disadvantage of using the constant flow mode because, as it can be seen in Fig. 3.26, the magnetization transfer (dM/dt) is less efficient when the steady state polarization chosen during an experiment gets closer to its maximum value M_{eq}. Nevertheless, if the results obtained in sealed cells could be reproduced with a constant flow, Fig. 4.8 shows that only one liter of OP cell could produce 20 scc/min of ^{3}He polarized at 55 %.

As a result of the previous considerations, several decisions were taken for the future design of the polarizer. The first one was to design it for a flow in the range of 10 to 20 scc/min. For lower flow, the time to reach the required amount of ^{3}He for lung imaging would be too long and no real breakthrough would be achieved compare to the low field polarizer. The second one is to perform MEOP at approximately 30 mbar with high discharge and in a cell with approximately 2.4 cm of diameter. The 31 mm open cell showed that it was difficult to obtain homogeneous density of metastable state in such large cell. On contrary, using a 14 mm diameter cell would require a total length of OP cell too important. Finally, and as a first prototype, it was decided to work with a total volume of approximately 1L corresponding to 2.2 m of cell. Thanks to the projection presented in Fig. 4.8 and if the best results obtained in open cells can be repeated (and neglecting the loss due to the compression) a polarization of 30 to 45 % should be obtained with a constant flow of 10 – 20 scc/min.

4.2.2. Compression

For the compression stage, a smaller version of the peristaltic compressor presented in subsection 2.1.5 (see also Fig. 2.6) was used. Its dimensions were chosen to reach a volumetric flow in the experimental range of pressure (20-40 mbar) fitting the chosen value of Q (10-20 scc/min) when running at 3-5 Hz. At this rotational speed, the vacuum reached at the input of the compressor is on the level of 10^{-5} bar for a 1 atm output pressure. This level of vacuum efficiently prevents impurities from diffusing to the OP cell when the output valve is opened at the beginning of an experiment for the first time (and of course in the presence of a capillary at the output of the OP cell). A rotary pump produced a vacuum of the level of 10^{-4} bar inside the body of the peristaltic compressor to prevent the peristaltic tube (Pharmed BPT tube model 06508-17, inside diameter of 6.4 mm) from shrinking. Some tests done while the vacuum was not used inside the compressor or when the compressor was running at lower speed (≈ 1 Hz) showed that the optical pumping cell was then getting dirty (color change of the plasma).

Finding a non magnetic engine for the compressor was more difficult. During a research of pneumatic engine that could satisfy our need (speed: 300 rpm, torque: 0.1-2 N.m), I found an interesting model and asked the company producing it (Globe Airmotors BV, http://www.globe-benelux.nl/) if it was possible to send a list of the materials with which the engine was made. The company answered that a new design was under construction to satisfy the demand for such non magnetic engine but that they needed someone to test it. I accepted it and the engine was first tested inside the superconducting magnet of our institute at 1.5 T to see if it was attracted by the magnetic field and if it was able to drive the compressor in the same conditions outside and inside the magnet. These tests being positive, the engine was then brought inside the MRI scanner in John Paul II hospital in Krakow to study the influence of the presence of the engine inside the scanner on the resonance frequency of small water sample and on the picture of a bigger water sample located at different distances from the engine. Inhomogeneities induced by the engine were about 4.5 ppm at 24 cm from the water sample, 12.7 ppm at 16 cm and 33 ppm at 8 cm. For MEOP, such inhomogeneities are negligible. In systematic studies performed at 1.5 T, the guiding field of the magnet was more inhomogenous (≈ 1000 ppm). On contrary, for MRI experiment, this level of inhomogeneity produces artifacts on the picture (Fig. 4.9, left) and the engine should be at least 50 cm away from the object to be imaged. All the different parts of the compressor were separately tested to see which one was the most perturbing. It appeared to be the stator and rotor ring. This first prototype engine was used anyway because it was fulfilling the experimental requirements and since summer 2010, the engine is commercially available on the main webpage of the company (Fig. 4.9, right). For our experiment, the engine is driven at the input with 2-3 bar of air supplied by an air compressor.

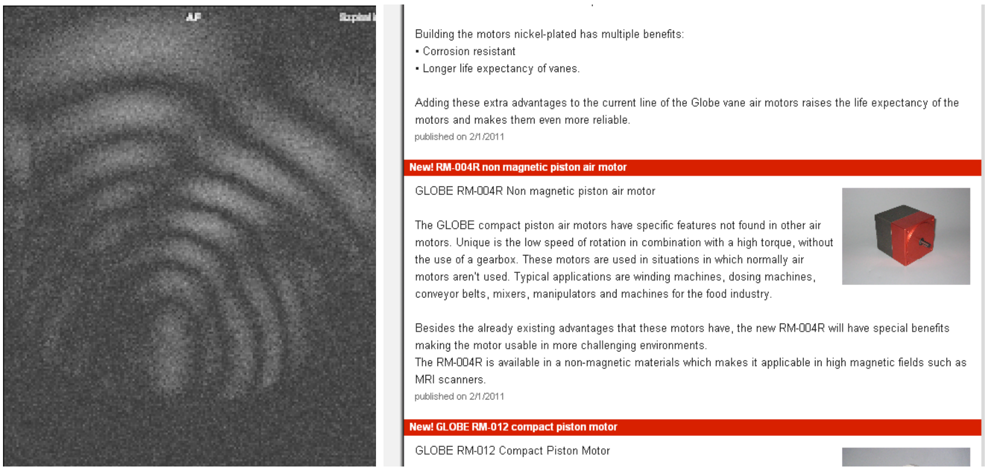

Building the motors nickel-plated has multiple benefits:
- Corrosion resistant
- Longer life expectancy of vanes.

Adding these extra advantages to the current line of the Globe vane air motors raises the life expectancy of the motors and makes them even more reliable.
published on 2/1/2011

New! RM-004R non magnetic piston air motor

GLOBE RM-004R Non magnetic piston air motor

The GLOBE compact piston air motors have specific features not found in other air motors. Unique is the low speed of rotation in combination with a high torque, without the use of a gearbox. These motors are used in situations in which normally air motors aren't used. Typical applications are winding machines, dosing machines, conveyor belts, mixers, manipulators and machines for the food industry.

Besides the already existing advantages that these motors have, the new RM-004R will have special benefits making the motor usable in more challenging environments.
The RM-004R is available in a non-magnetic materials which makes it applicable in high magnetic fields such as MRI scanners.
published on 2/1/2011

New! GLOBE RM-012 compact piston motor

GLOBE RM-012 Compact Piston Motor

Fig. 4.9. Left: artifact produced on a picture (spin-echo sequence) of a 24 cm spherical phantom filled with water when the air motor is located 7 cm from it. Right: part of the main webpage of Globe Airmotor BV company: http://www.globe-benelux.nl/ showing the design of the reversible non magnetic piston air motor, model RM-004R

During the test of the pneumatic engine inside the scanner, the homogeneity of the magnet was checked inside the tube of the scanner. This tube is particularly long compare to different scanners and has a level of inhomogeneity of only 11 ppm in an imaginary rectangular cuboid of 1 m length and 40 cm height and depth centered in the middle point of the magnet.

4.2.3. Design

In figure 4.10, the high field polarizer is schematically described in totality. It consists of three main elements: the optical pumping plate and the gas handling system divided into two parts (the gas inlets system and the cleaning system).

- **Optical pumping plate**

In order to easily have a measurement of the magnetization inside the OP and storage cells, the system was designed to fit inside the birdcage coil dedicated to ^{3}He human lungs MRI (see § 2.2.2 and Fig. 2.10). This condition, together with the homogeneity measurements of the magnetic field inside the scanner evoked in the previous paragraph and showing that the OP cells could be almost one meter long, gave the dimension restrictions for the OP plate. It was decided that three OP cells would have an inner diameter of 24 mm, a length of 80 cm, and would be connected in series on a wooden plate (length: 1.5 m, width: 35 cm). The 70 cm long available space is dedicated to the optics elements.

A 10 W laser from Keopsys (Lanion, France) is located in a safe area of the clinical scanner room, and the 4 m long fiber is connected to a Kepler-like telescope (magnification 2x, Eksma Optics, Vilnius, Lituania) and a new pair of axicons from the same company allowing a tunable diameter of the annular beam from 18 to 28 mm. A first pair of mirrors at 45° regulates precisely the height and inclination of the beam. This latter is divided into three beams by a set of half-wave plates and polarizing beam splitters. Each beam is passing through one cell back and forth thanks to additional mirrors and after having been circularly polarized by quarter-wave plates. It was also possible to use only one beam and guide the light transmitted by the first cell into the second and third cells. But in this case, the circular beam should be neither divergent, neither convergent on a length scale of 6 m. It was experimentally really difficult to achieve due to optics imperfections. Moreover, it was shown in the conclusion of chapter 3 that a pump power of 3 W per cell would be largely sufficient. The transmitted light of the laser at the output of the second and third cell is focused and monitored with two lenses and photodiodes.

Forty circular electrodes are wired around each cell with a space of about 2 cm between them. Previous experiments in our laboratory showed that this configuration was more efficient than the spiral one for generating a dense plasma inside the 24 mm diameter cells. The generator and amplifier of the systematic studies in sealed cells are used to create a 1 MHz rf discharge inside the second and third OP cells. A GW Instek (model GFG 3015) generator (1 MHz) with a 100 W wide band amplifier is dedicated to the first cell. It is then possible to have two different regimes of discharge between the 1st and the 2nd and 3rd cells.

Between the 1st and 2nd cells, a smaller wooden plate (12 * 60 cm) is fixed on the main one. The peristaltic compressor, the pneumatic engine and the 500 mL storage cell (Sample flask with glass piston and plain side arm, model SFB/500/G, Aimer Products Ltd, Enfield, England) are mounted on this plate. When the compression is finished, the plate can be easily disconnected from the

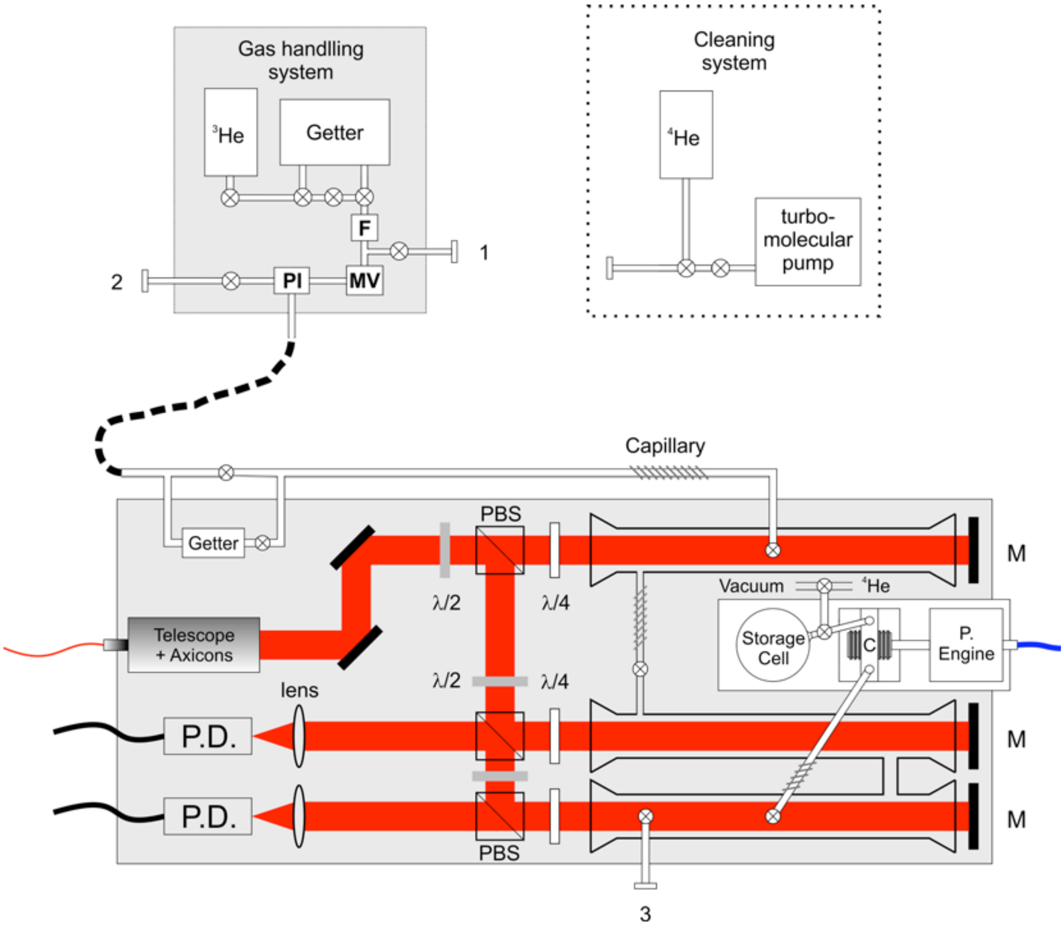

Fig. 4.10. Scheme of the high field polarizer: the optical pumping plate (bottom, 1.5 m * 35 cm) is connected permanently using a flexible pipe to the gas handling system (top left) supplying high purity ^{3}He through a getter, a 50 μm filter (F), a fine metering valve (MV), a pressure meter (PI), and an additional getter located as close as possible from the three OP cells (diameter: 24 mm, length 80 cm) mounted in series. Three capillaries are inserted for flow restrictions at the input of the first cell, between the first and the second cell and at the output of the third one. The laser beam, expanded by a Kepler-like telescope and whose annular shape is created by a pair of axicons, is divided into three beams by a set of half-wave plates (λ/2) and beam splitters (PBS). Each beam is being circularly polarized and aligned with each cell by a set of quarter-wave plates (λ/4) and mirrors (M) and the transmissions of the second and third beam are recorded by two photodiodes (P.D.). The peristaltic compressor (C), driven by a pneumatic engine (P. engine), compresses the gas from the third cell to the storage cell. These three elements are mounted separately on a smaller plate (60 * 12 cm) that can be disconnected easily from the main optical pumping plate when the compression is finished and the polarizer remove from the scanner. When the polarizer is not used, it is connected in a separate room to a cleaning system (top right) consisting of a turbomolecular pump and a ^{4}He bottle. The cleaning system can be connected at three different locations labeled 1, 2 and 3 on the figure.

main one and stays inside the scanner when the polarizer is taken out from its tube to let a patient go in. Connections between output of the 3rd cell, compressor and storage cell are made from Pharmed BPT tube of different diameters and the design is similar to the low-field polarizer one (see Fig. 2.1). A vacuum membrane pump and a bottle of ^{4}He are located far from the scanner and connected to the storage cell through longs pipes for washing it between experiments and mixing ^{3}He before compression inside a Tedlar bag.

At the entrance of the first OP cell, a capillary is used, after the 2nd getter and the metal-glass connection, to restrain the back diffusion of ^{3}He to the metallic pipe during the constant flow mode. A second capillary between 1st and 2nd cell has the same effect and allows having two different conditions of discharge in the three cells. At the output of the third cell, a last capillary prevents impurities from the peristaltic compressor to contaminate the cells.

- **Gas handling system**

The gas handling system was built on a separate and compact Plexiglas plate (≈ 60 * 50 cm). It is reduced as its minimum to be as close as possible from the OP plate and limits the purity issue of the 4.1 subsection. It consists of a non magnetic ^{3}He bottle, the same getter, 50 μm filter and valves as the ones used for the GHS of the low-field polarizer. The pressure meter of the open cells preliminary experiments was kept. On the contrary, the flow meter working with electromagnetic valves was replaced for a fine metering valve (model SS-SS2-D-VH, Swagelok) needed to reduce the pressure inside the getter (≈ 1 bar) to the required one inside the OP cells. The connection with the OP plate is made with a new 61 cm long flexible tube made of 321 stainless steel (model 321-4-X-24DFR, Swagelok) as we thought the previously used flexible tube was mainly responsible for the impurities in the open cell experiment. Finally, an additional compact getter (model MC1-902F, SAES Pure Gas, Lainate, Italy) was inserted on the OP plate, before the metal glass connection and as close as possible from the entrance of the 1st cell.

All the elements were checked to be safe when used in high field environment and only the 1st getter is slightly magnetic (1.4 ppm change of Larmor frequency at 40 cm from a small water sample).

- **Cleaning system**

A second part of the GHS, dedicated to cleaning purpose and consisting in a TMP and a ^{4}He bottle was built separately in a storage room close to the MRI scanner. When the polarizer is not used, it is connected to this cleaning system through a KF 16 flange adaptor. There are three locations where the cleaning system can be connected, labeled “1, 2 and 3” on figure 4.10. “1” is dedicated to the cleaning of the GHS and was used mainly after its construction was finished. Usually, the cleaning system is connected in parallel to “2” and “3”. When it is necessary, OP cells are filled with ^{4}He at low pressure, and strong discharge is applied through the rf electrodes before vacuuming the cells with the TMP.

4.2.4. Choice of the capillaries

The choice of the dimensions of capillaries inserted in the different parts of the polarizer results from a good combination between a negligible back diffusion of ^{3}He and an acceptable pressure drop. It is assumed that the compressor speed is regulated in such a way that the flow Q is constant and in the 10 to 20 scc/min range and that the pressure at the output of the fine metering valve (measured by a pressure meter) is also constant and in the 20 to 40 mbar range. The back diffusion is neglected if the average speed of helium inside the capillary is much higher than the mean free diffusion length divided by the transit time of atoms in the capillary.

Let's consider first the free diffusion coefficient of ^{3}He: D. In [Tas05], it is given by:

$$D = 1.967 \times \left(\frac{T}{300}\right)^{1.71} / P \tag{4.4}$$

where D is in cm^2/s if T is in K and P in atm. In a three dimensions problem, the main distance over which a particle will have diffused from its starting point during a time t is then:

$$\bar{x} = \sqrt{6Dt} \tag{4.5}$$

In addition, the mass flow Q_m can be written:

$$Q_m = u\rho S \tag{4.6}$$

where u is the average speed of the gas, ρ, the mass density and S the cross section. Equation 4.6 can then be rewritten to give the velocity of the gas in the capillary:

$$u = \frac{Q}{4.6507 \times d_t^2 \times P} \tag{4.7}$$

u is in m/s if Q is in scc/min, the diameter of the tube d_t in cm and P in mbar. For a diameter of 1.6 mm, equation (4.7) gives a mean velocity u of 8.40 m/s for Q = 20 scc/min and P = 20 mbar (case 1) and 2.10 m/s for Q = 10 scc/min and P = 40 mbar (case 2). The average time spent by the gas when going through 7 cm of such capillary is then 8.3 ms in first case and 33 ms in 2nd case. During this time, the average free diffusion length from Eq. (4.5) is 2.23 cm (case 1) and 3.14 cm (case 2) at 300 K. This length is at least two times lower than the length of the capillary, which is safe. Moreover, in this crude model, we considered the free diffusion in an open 3 dimensions system, which gives an order of magnitude but is actually not realistic. The mean free path inside a small diameter tube is lower and as a comparison we have $\bar{x} = \sqrt{2Dt}$ for a one dimensional diffusion problem.

It can then be concluded that negligible back diffusion will occur with such capillary.

Remark: the same calculations can be done inside the 2.4 cm diameter OP cells. For Q = 15 scc/min and P = 30 mbar, u ≈ 2 cm/s. It means that helium atoms spend on average 40 s in each cell. During this time, the mean free path is approximately 1.3 m showing that there is a total mixing of atoms inside OP cells.

Before validating the capillary dimensions, the pressure drop ΔP introduced by them should be checked. The following calculation is largely inspired from a private communication from Pierre-Jean Nacher who is finalizing an article on a wider subject. For this derivation, the first parameter that should be calculated is the Reynolds number R_e:

$$R_e = \frac{\rho u d_t}{\Xi} \tag{4.8}$$

where Ξ is the viscosity of ^{3}He (≈ 20 μPa.s at 300 K). In the experimental range of flow and diameter, R_e is around 1.5, which is much lower than the critical value 2000 for which flow becomes turbulent. In consequence, the flow regime is always laminar and the pressure drop is then proportional to:

$$\delta P \propto \frac{Q}{C} \tag{4.9}$$

where C is the fluid conductance. The expression of C depends on a second parameter, the Knudsen number $K_n = \lambda / d_t$, where λ is the mean free path:

$$\lambda = \frac{\Xi}{P}\sqrt{\frac{\pi}{2}\frac{R_g T}{M_m}} \tag{4.10}$$

with the gas constant R_g and the molar mass M_m. At room temperature:

$$K_n = \frac{0.192}{P \times d_t} \tag{4.11}$$

if P is in mbar and d_t in mm. In our case (P = 20 mbar), this gives $K_n = 0.006 < 0.01 \Rightarrow$ we are in the hydrodynamic regime and a simple expression of C is given by:

$$C = \frac{\pi}{128}\frac{d_t^4 P}{\Xi L_c} \tag{4.12}$$

where L_c is the length of the capillary (7 cm). Equation 4.9 can then be integrated along the capillary to get the final formula giving the pressure drop between input and output pressures:

$$P_{in}^2 - P_{out}^2 = \frac{256\Xi}{\pi}\frac{QL_c}{d_t^4} \qquad (4.13)$$

For an input pressure of 30 mbar and a flow of 15 scc/min measured on the pressure meter, the pressure inside the first OP cell is then 29.3 mbar, 28.5 mbar in the 2nd and 3rd cells and 27.7 mbar at the input of the compressor. In conclusion, the total pressure drop is negligible and has not impact on the compressor flow. The three capillaries have the dimensions discussed in this subsection: length 7 cm and diameter 1.6 mm.

4.3. Results:

4.3.1. Cleaning and first tests with ^{4}He

It took around 6 months to complete the construction of the gas handling system and the polarizer. While the OP cells were being finalized in Gdansk, the GHS was cleaned up to the metal glass connection by connecting the cleaning system in the output “1” of Fig. 4.10 and heating the tubes with a hot air dryer. The OP cells, after being mounted on the wooden plate with holders made of Plexiglas, were connected together by a local glass blower. Optics was then fixed on the plate and the laser beam was aligned with the three cells (Fig. 4.11).

Fig. 4.11. Picture of the OP plate of the high field polarizer during construction. On the foreground, the pair of axicons is mounted on Plexiglas holders. Non magnetic holders were ordered for mirrors, half and quarter-wave plates and polarizing beam splitter. The peristaltic compressor can be seen on the background. All the system fits inside the birdcage coil.

Non magnetic holders were then built by our workshop to hold and protect the fragile connection between the gas handling system and the cells. The cleaning process of the cells could then start and lasted almost one month and a half (see Fig. 4.12). During the first week, the cells were vacuumed (10^{-8} mbar) and heated to 100°C using a heating tape. The second step consisted in sustaining high plasma discharge inside 20 mbar of ^{4}He during 2-3 hours and vacuuming with a turbomolecular pump until $\approx 10^{-8}$ mbar. This step was repeated in average two times per day and during almost one month, until only the spectral lines of ^{4}He could be visible in the emitted light from the plasma. All the cleaning process needed to be unfortunately repeated (but for a shorter time) because the glass connection between 2nd and 3rd cell cracked.

Fig. 4.12. Cleaning process of the OP cells. Left: A heating tape (100°C) was wired around each cell while a vacuum was produced by a TMP. The aluminium foil visible on the picture keeps the heat close to the glass. Right: Plasma discharge with 20 mbar of ^{4}He. The shape of the plasma is made of rings close to each electrode.

When the system started to be operational, preliminary experiments were performed with ^{4}He. During these experiments, the compressor was tested for different OP pressures, rotational speeds and the predicted flows of 10-20 scc/min were obtained. The capillaries were also checked to be well designed. At the beginning of an experiment, the absorption of the pump laser was measured. The peristaltic compressor was then switched on for 5 min to reach a good level of vacuum at the output of the third cell before opening this latter and regulating a desired pressure at the input with the fine metering valve. After accumulation in the storage cell, the valve of the third cell was closed, the compressor switched off and absorption was checked again. It showed that if the pressure in the OP cells is at least 30 mbar when opening the cell, neither change of color of the plasma, neither differences between absorption before and after experiments were observed, which means that no impurities is contaminating the cell. After these successful tests, the polarizer was brought inside John Paul 2nd hospital in Krakow.

4.3.2. Characterization inside the MRI scanner

Three people are required to transport the polarizer from the storage room to the scanner. It is also possible to use a hospital bed dedicated for patient. In that case, two people can handle it but all the electronics for discharge, pressure meter, laser and oscilloscope for photodiodes need to be brought before in a safe location of the scanner room. All the process takes at least 30 min. Two pictures of the polarizer being inside the scanner are displayed on figure 4.13. The optical detection with a probe laser was not implemented due to a lack of space on the optical plate and because of the complexity of bringing additional lock-in amplifiers, laser, integrators, photodiodes and oscilloscope in a clinical environment already full with electronics for discharge, air compressor, vacuum pumps and bottle of helium. The measurement of nuclear polarization inside the OP cells is thus an important quantity missing for the full characterization of the polarizer but M can be assessed inside the storage via the ^{3}He coil. It also gives a signal proportional to the polarization inside the OP cells although the low filling factor for the cells and a not homogeneous flip angle map over the cells longer than the coils result in non reproducible values. This method was still used to compare the magnetization value changes when pumping with different laser powers and discharge levels.

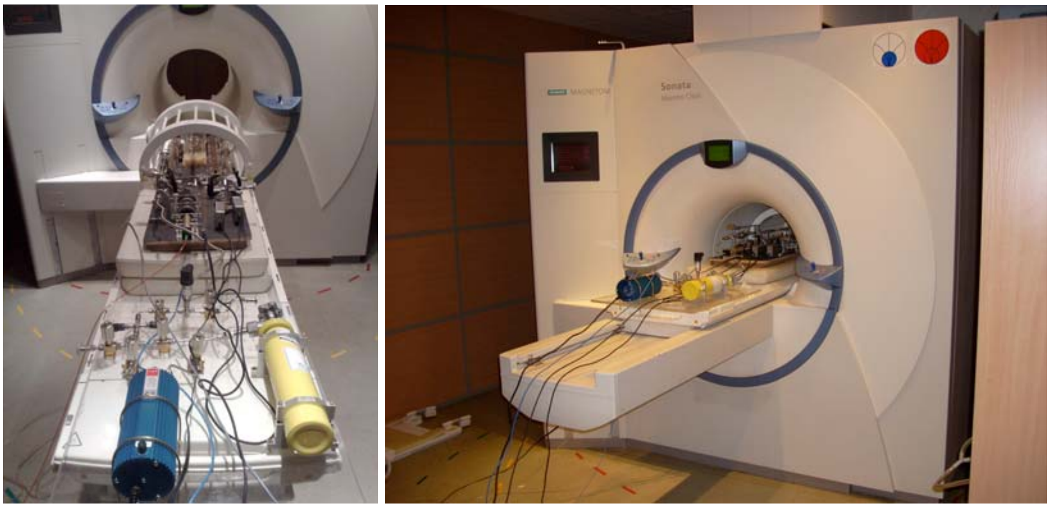

Fig. 4.13.Pictures of the high field polarizer outside (left) and inside the MRI scanner (right). The storage cell is in the center of the birdcage coil and the GHS is located at the bottom of the bed allowing access for a regulation of the flow during accumulation.

At the beginning of each experiment, the frequency of the laser can be tuned to the f^{2m} transition by looking with an oscilloscope at the transmission of the beam on the 2nd and 3rd cell. A comparison of the FID signal amplitudes acquired by the scanner showed that without flow and for each cell, the highest amplitudes were reached when pumping with a moderate discharge and a pump power of 1-2 watt in each cell. But to reduce the build-up time, so important during constant flow experiment, the following experimental conditions are used. Two different levels of discharge are applied between the first cell and the two next ones. In the first cell, the discharge is much stronger and the pump power is about 3 W allowing a faster pumping but a moderate polarization M_{eq1}, where M_{eq1} is the steady-state polarization of the gas inside the first cell without flow. To get an idea of t_b, the first cell was closed and evolution of the transmission of the pump beam in the first cell was observed with an additional photodiode. With such conditions, t_b was approximately 10-15 s. During constant flow, the gas arrives inside the second cell with already a “pre-polarization” quickly reached in the first cell. In the second and third cells, the discharge is lower and only 1.5 W is used per cell. The polarization of the gas is then improved to a certain fraction of M_{eq2} ($M_{eq2} > M_{eq1}$) depending on the flow but with a lower production rate R than in the first cell (the build up time inside the 2 last cells being about 25-30s). The total laser power used is then 6 W divided into three beams by the half-wave plates and beam splitters.

Unfortunately, the fiber of our laser broke during the first accumulations and the laser was replaced by a similar one (10 W, Keopsys) but having a problem of polarization maintaining inside the fiber. In consequence, the total power was still 8 W but the power in each cell was fluctuating a lot and could not be controlled anymore.

4.3.3. First accumulations and calibration of polarization

The calibration of the polarization inside the storage cell was done by using a thermally polarized phantom as a reference. The phantom is the one used for the flip angle calibration and described in § 2.2.2. A comparison between the FID signals coming from the phantom and the storage cell after accumulation of polarized ^{3}He was made on the same day, with the exact same location inside the coils, the same NMR sequence and flip angle. To increase the SNR of the signal from the first phantom, the signal was averaged 60 times with a repetition time of 25 s that is approximately 5 times the longitudinal relaxation time T_1 inside the phantom. The difference in size between the storage cell (500 mL, 10 cm diameter) and the phantom (250 mL, 8 cm diameter) was neglected, meaning that the filling factor was supposed to be the same. To increase the accuracy of the measurement, the signals were processed from the raw data with a Matlab program in the frequency domain. A Fourier transformation (FT) of the absolute value of the time domain signals gives the NMR spectra presented on figure 4.14. To reduce the influence of the noise, the signal was integrated only under the peaks. A comparison of these integrals and the corresponding pressures and volumes gave the nuclear polarization inside the storage cell during this experiment (34.7 %). An additional FID was taken before with a small flip angle (3.5 °) when the OP plate was still inside the scanner. This FID was always measured in the same conditions for each experiment of compression, which allowed us to deduce the polarization inside the storage cell for each accumulation performed.

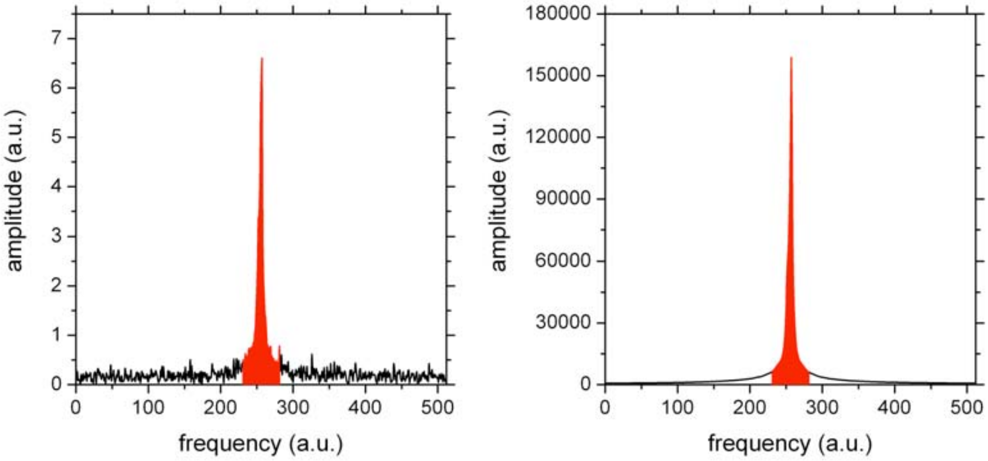

Fig. 4.14. FT of the absolute value of the FID signal (512 samples, 10 kHz bandwidth) obtained in the thermally polarized phantom (left, M = 3.892 10^{-6}, P*V = 329.7 ± 7 scc, flip angle: 61.6 °) and the storage cell for the calibration experiment (right, P*V = 79,2 scc, flip angle: 61.6 °). A comparison of the integrated signal under the peak (area in red under the curve) gave a polarization of 34.7 ± 1.5 %.

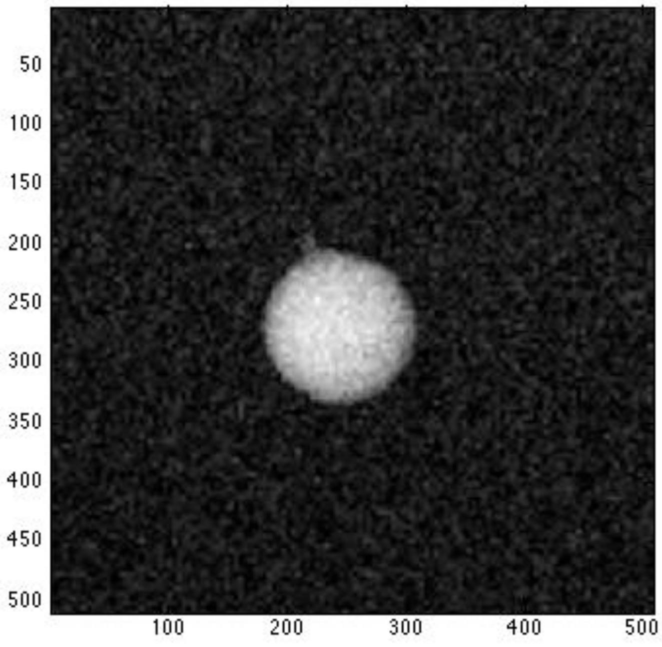

Fig. 4.15. Image of the 500 mL storage cell on the OP plate and filled with 165.6 mbar of ^{3}He polarized at 23.9 % (resolution: 128*128, FOV: 400*400 mm, slice thickness: 20 cm, TR: 8 ms, flip angle: 5.6°, t_{ac} = 1 s, no average). Image reconstructed with Matlab with a bilinear interpolation and no filter.

In total, nine accumulations were performed ranging from 29 scc for flow tests to 493 scc for lung imaging experiment. It showed that, as expected increasing the flow reduces the polarization inside the storage cell. On average, a polarization of 33 % for a 15 scc/min flow was obtained. The best M value (44.8%) was obtained for a flow of 8 scc/min. During some of the tests, the decay time inside the storage cell was measured to be $T_1 = 208 \pm 8$ min and the flash sequence was tested on the storage cell (Fig. 4.15), showing that the lungs MRI could be performed on healthy volunteer.

4.3.4. Lungs MRI

Three accumulations of approximately 500 scc (1 atm) were made with an average flow of 12.5 scc/min (40 min). After compression, the polarization is checked with a NMR sequence and ^{4}He is mixed with ^{3}He until an absolute pressure of 2.4 Bar. The storage cell is then closed, the peristaltic compressor is disconnected from the output of the 3rd OP cell and OP plate is taken out from the scanner while the storage cell stays inside with the compressor and pneumatic engine. A healthy volunteer is then introduced inside the scanner and the gas being over the atmospheric pressure is released from the storage cell to a 1L Tedlar bag previously rinsed and pre-filled with ^{4}He.

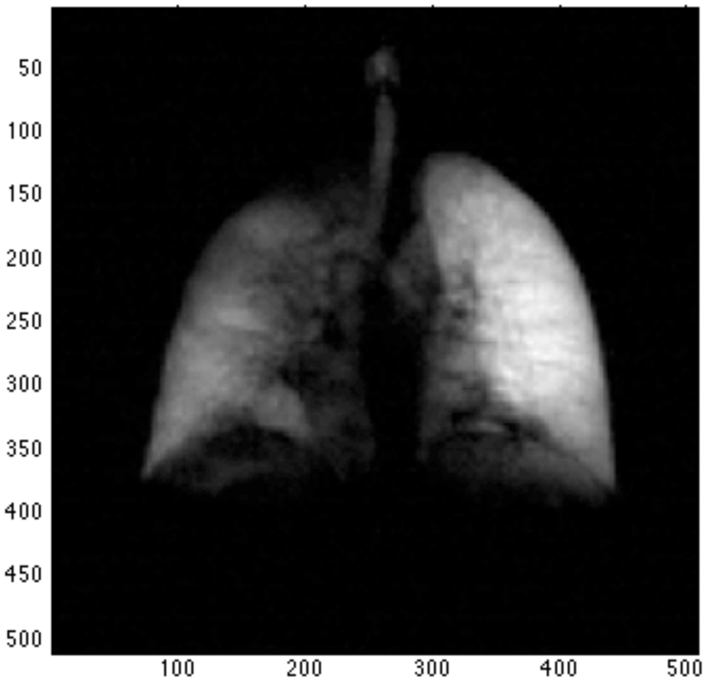

Fig. 4.16. ^{3}He (272 scc at 20.8 ± 1%) coronal image of the lungs of a healthy volunteer using a FLASH sequence (20 cm slice thickness, 38 cm FOV, 128*128 matrix, flip angle: 8.6°, bandwidth per pixel 260 Hz, TE = 3.7 ms, TR = 7.9 ms, SNR = 56.3).

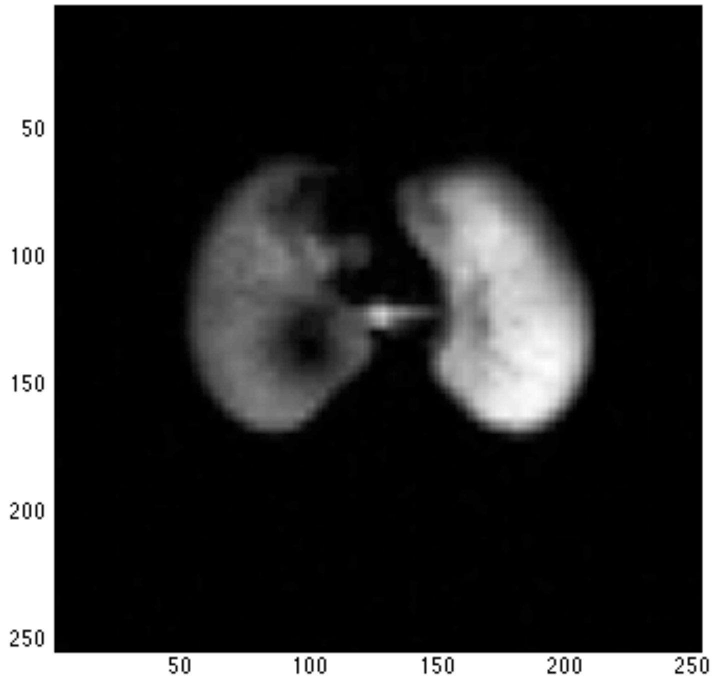

Fig. 4.17. ^{3}He (150 scc at 20.8 ± 1%) transversal image of the lungs using a FLASH sequence (5 cm slice thickness, 38 cm FOV, 64*64 matrix, flip angle: 12.2°, bandwidth per pixel 260 Hz, TE = 3.7 ms, TR = 7.9 ms, SNR = 64.6).

The decay time T_1 inside the Tedlar bag was measured to be longer than 1 h 30. When the sequence is ready, the patient is breathing a volume of ^{4}He from a different bag to wash his lungs from paramagnetic oxygen and then the mixture of ^{3}He-^{4}He. The sequence lasts 1 s per slice for a resolution of 128 lines limiting the apnea in our experiments to only 3 s in the worst case. After the first sequence, the gas left inside the storage cell (almost half) can be “re-compressed” to the Tedlar bag for a second or the same patient. During recompression, it was checked that the polarization losses due to the peristaltic compressor are negligible. On figure 4.16, 4.17 and 4.18, images performed during two accumulations (the third one did not work due to an artifact) are presented. These pictures were reconstructed from the raw data with a Matlab program. Bilinear interpolation was used but no filter. Except a small asymmetry between right and left lung due probably to a coupling problem between Siemens system and coil from RAPID Biomedical, the quality of the pictures is much better than the one obtained with the low-field polarizer (Fig. 2.15). The trachea and the first branches are clearly visible on these ventilation maps of the lungs and the SNR was calculated with Matlab, showing high values up to 65.

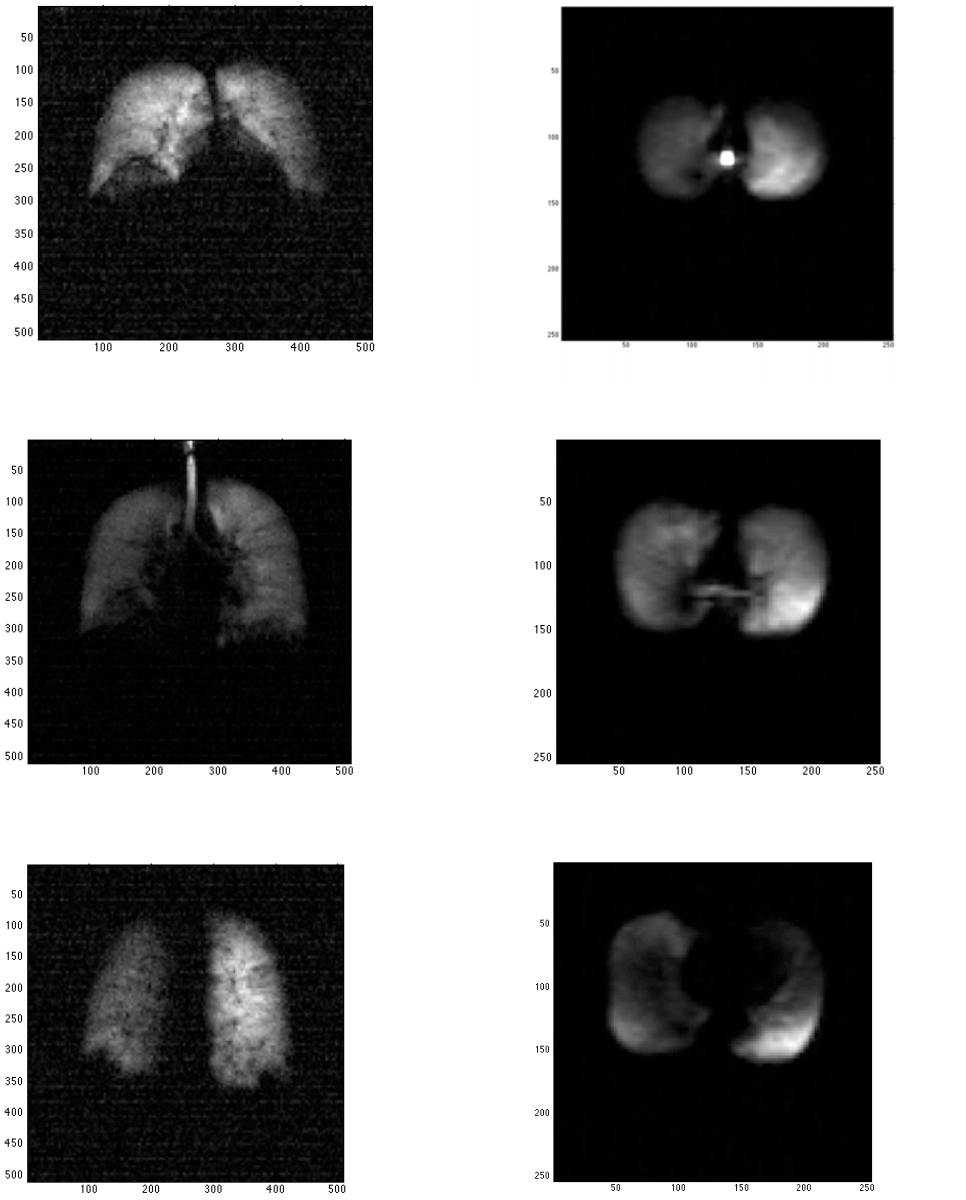

Fig. 4.18. Left: ^{3}He (285 scc at 32.2 ± 1.5%) coronal image of the lungs of a second healthy volunteer using a multi-slices FLASH sequence (5 cm slice thickness, 38 cm FOV, 128*128 matrix, flip angle: 8.6°, bandwidth per pixel 260 Hz, TE = 3.7 ms, TR = 24 ms). Top to bottom: from chest to the back (SNR: 11.2, 14.4 and 11.6 respectively). Right: ^{3}He (161 scc at 32.2 ± 1.5%) transversal image of the lungs using a multi-slices FLASH sequence (5 cm slice thickness, 38 cm FOV, 64*64 matrix, flip angle: 12.2°, bandwidth per pixel 260 Hz, TE = 3.7 ms, TR = 24 ms). Top to bottom: From head to belly (SNR on the lungs: 51.6, 67 and 44.1 respectively). The SNR of the top right picture in the trachea is actually almost 230.

4.4. Summary of the high-field polarizer:

In this chapter, it has been proven that a high-field polarizer can be built, work in-situ and produce enough gas for high quality ventilation lung imaging. Although the results are clearly below the expected values obtained in sealed cells due to a purity problem, the results seem to match with a relatively good agreement the simulation done with small open cells in paragraph 4.2.1. Due to a lack of time and a broken laser at the end of this work, the characterization could not be fully achieved. This polarizer should be considered as a first prototype and some necessary upgrade involving laser protection, reinforcement of the glass connections that cracked a couple of times and a more automated system for controlling valves and flow while running should be implemented for a commercial application. However, the polarizer still showed a factor 4 increase in gas production compared to the low-field polarizer, reaching flows of 15 scc/min of ^{3}He hyperpolarized to a similar polarization of 30 to 40%. Compare to this latter and other production system, another benefic aspect is that the gas is produced directly in-situ and that negligible losses thus occur until the lungs MRI experiments. It explains the difference between the qualities of the lungs images obtained with both polarizers although the amounts of ^{3}He were similar. The time was missing to repeat lungs imaging but it should be stressed that the quality can be still improved easily by compressing all polarized gas from the storage cell into the Tedlar bag, which would allows to reduce slice thickness and increase number of slices.

At last, another benefic advantage of this polarizer is the relatively low cost to produce it compare to high technology system developed in Mainz recently. It cost approximately 65,000 euro for which half is coming from the laser and the turbomolecular pump. The main inconvenient for the potential production of this polarizer is coming from the global ^{3}He shortage whose price, compared to its availability, has been increased dramatically in these last five years and that is why it was not included in the above cost study.

Conclusions

For many years, polarized ^{3}He has been used in many domains of physics. One of them is to use it as a contrast agent for magnetic resonance imaging of the respiratory airways. Lungs MRI has made significant progress in the last few years reaching the step of clinical applications for the early detection of respiratory diseases such as COPD, cystic fibrosis, asthma… The present work is focused on one polarization technique of ^{3}He called metastability exchange optical pumping. This process has been well known since several years and the main features and equations of a recent complete model were recalled in the first theoretical chapter. The theory was transferred to experience with the realization of a low field table-top polarizer whose initial design was completely changed to copy the one made in Paris. Thanks to the implementation of a new 10 W laser, but also a 50 cm long optical pumping cell and a new design of the peristaltic compressor, the polarizer has a typical production of 3 to 4 scc/min for a reproducible polarization on the order of 30 to 40 % inside the storage cell, which makes it a good facility for lungs MRI in small animals. Thanks to this new polarizer, new in-vivo images of rat lungs were made showing a two-fold increase in spatial resolution and a four-fold increase in signal to noise ratio. Moreover, new dynamic radial images were performed. However, it also showed the limits of the method when experimenting human lungs MRI. These limits are mainly a high compression factor and a low production rate due to the pressure conditions ($\approx$ 1 mbar) at which standard optical pumping is performed.

One possibility to go beyond these limitations is to optically pump ^{3}He at higher pressure and at high magnetic field. In this work was presented my contribution to the systematic studies of MEOP begun earlier between the group of Tomasz Dohnalik and Pierre-Jean Nacher in these non standard conditions. Thanks to the benefic effect of hyperfine decoupling occuring at high magnetic field (> 0.1 T) that suppresses some of the polarization relaxation channels, it is possible to obtain high value of nuclear polarization at higher pressure, which increases the efficiency of the method. The systematic studies presented in this dissertation were performed at 1.5 and 4.7 T with 20 mL sealed OP cells over a wide range of pressure (from 1.33 to 267 mbar), discharges conditions but also laser power and beam shapes. At 4.7 T, a comparison of the results with those obtained earlier by Anna Nikiel at lower magnetic fields showed that the reachable steady state polarization increases with B until a plateau at 60 % for 32 and 67 mbar. But it also highlighted a negative effect of the hyperfine decoupling inducing longer build-up process and thus lowering the production rate at a given pressure.

At 1.5 T, which, regarding to the previously obtained polarization and production rate values, looks like a good choice for performing MEOP, the implementation of a pair of axicons reversing the standard Gaussian beam to an annular beam resulted in a 25% increase of polarization values at 32 and 67 mbar, yielding 66.4 and 57.3% respectively. Even more interestingly, the production rates reached are 10 times higher than the ones obtained in the best standard conditions and a polarization of 31% was still acquired at 267 mbar. The fact that MEOP is being more efficient at higher pressure with the annular shape of the pumping beam is coming from the inhomogeneous distribution of metastable states atoms inside the OP cell. A higher density is located close to the electrodes where metastable atoms are created and whose diffusion to the center of the cell is reduced by the increasing number of collisions due to high pressure. It is then not surprising to reach a more efficient pumping when the shape of the beam match exactly the distribution of 2^3S atoms from which the gas is optical pumped. In addition, results at 1.5 T showed a good agreement with the MEOP model recently updated at low magnetic field. One of the main conclusions is the confirmation of the presence of a laser-induced relaxation previously observed in standard conditions for high absorbed laser power. This relaxation is the major factor limiting MEOP but its physical origins has not been discovered yet. However, the relaxation rates found in this work seems 10 times lower than in low field conditions and agree with the values previously obtained by Marie Abboud.

Nevertheless, the spectacular increase of both steady-state polarization and production rate was the main motivation for studying the feasibility of building a high-field polarizer working inside the most widespread available scanner at 1.5 T and producing directly onsite required boluses of polarized ^3He for human lungs MRI. After preliminary tests in small open cells that unfortunately showed a dramatic decrease of the production rate due to a purity issue, a relatively low-cost, compact and non magnetic high field polarizer was built. It is consisting of three 80 cm long OP cells (diameter: 24 mm) connected in series to an input gas handling system and to an output peristaltic compressor driven by a new design of a pneumatic engine. The production matches the simulations done with the preliminary tests and it takes about 40 min to compressed 500 mL of ^3He ($M \approx 33\%$) to the atmospheric pressure with an optical pumping pressure of approximately 25 mbar. The main advantages of this polarizer are the four times higher production, its cost compared to other high production systems and the fact that the gas is produced in-situ, which is reducing the loss due to transportation. Unfortunately, the time was missing to make easy update of this first prototype. An optical detection of the polarization inside each OP cell would be necessary to fully understand the limitations and to improve flow and output polarization. It would be also worth trying to reduce again impurities in the system by implementing for example a non relaxing additional getter at the output of the 3rd OP cell. Anyway, this prototype works and was validated with the acquirement of high SNR human lung images. It proved that it is possible to hyperpolarize ^{3}He at high magnetic field and high pressure in an open system and is opening the way of a more automated and commercial system that could reach higher flow with more optical pumping cells connected together.

In conclusion, since my arrival in Krakow, two ^{3}He polarizers have been built: a low-field polarizer dedicated to small animal experiments whose results are comparable to the standard table-top polarizers and the first high-field polarizer ever built yielding the first good quality images of ^{3}He human lung ventilation done in Poland. The two polarizers have similar values of polarization (30 to 40%) but the high-field one produces the gas 4 times faster. Thus, our group has now the tools required to perform pre-clinical research on lungs MRI. The only concern is the rarity of ^{3}He at the moment. That is why the recycling of the gas, as few other groups do it already, should be soon implemented. An alternative is also being brought by the construction of a ^{129}Xe polarizer, which gives the hope that simultaneous and comparative experiments of ^{129}Xe and ^{3}He will be possible in a near future.

References

[Abb04] Abboud M., Sinatra A., Maître X., Tastevin G., Nacher P.J., *High nuclear polarization of ^{3}He at low and high pressure by metastability exchange optical pumping at 1.5 tesla*, Europhysics Letters **68**, 2004, pp. 480-486.

[Abb05a] Abboud M., *Pompage Optique de l'Hélium-3 à forte pression dans un champ magnétique de 1.5 T*, Dissertation to get the grade of Docteur de l'université Paris VI, Paris, 2005, available online at http://tel.archives-ouvertes.fr/tel-00011099.

[Abb05b] Abboud M., Sinatra A., Tastevin G., Nacher P.J., Maître X., *Metastability Exchange Optical Pumping of Helium-3at High Pressures and 1.5 T: Comparison of Two Optical Pumping Transitions*, Laser Physics **15**, 2005, pp. 475-479.

[Alb94] Albert M.S., Cates G.D., Driehuys B., Happer W., Saam B., Sringer C.S. Jr, Wishnia A., *Biological magnetic resonance imaging using laser-polarized ^{129}Xe*, Nature **370**, 1994, pp. 199-201.

[And59] Anderson L.W., Pipkin F.M., Baird J.C., *N^{14}-N^{15} Hyperfine Anomaly*, Physical Review **116**, 1959, pp. 87-98.

[And05] Andersen K.H., Chung R., Guillard V., Humblot H., Julien D., Lelièvre-Berna E., Petoukhov A., Tasset F., *First results from Tyrex, the new polarized-^{3}He filling station at ILL*, Physica B **356**, 2005, pp. 103-108.

[Ant93] Anthony P.L., Arnold R.G., Band H.R., Borel H., Bosted P.E., Breton V., Cates G.D., Chupp T.E., Dietrich F.S., Dunne J., Erbacher R., Fellbaum J., Fonvieille H., Gearhart R., Holmes R., Hughes E.W., Johnson J.R., Kawall D., Keppel C., Kuhn S.E., Lombard-Nelsen R.M., Marroncle J., Maruyama T., Meyer W., Meziani Z.E., Middleton H., Morgenstern J., Newbury N.R., Petratos G.G., Pitthan R., Prepost R., Roblin Y., Rock S.E., Rokni S.H., Shapiro G., Smith T., Souder P.A., Spengos M., Staley F., Stuart L.M., Szalata Z.M., Terrien Y., Thompson A.K., White J.L., Woods M., Xu J., Young C.C., Zapalac G., *Determination of the neutron spin structure function*, Physical Review Letters **71**, 1993, pp. 959-962.

[Ban10] Bannier E., Cieslar K., Mosbah K., Aubert F., Duboeuf F., Salhi Z., Gaillard S., Berthezène Y., Crémillieux Y., Reix P., *Hyperpolarized 3He MR for Sensitive Imaging of Ventilation Function and Treatment Efficiency in Young Cystic Fibrosis Patients with Normal Lung Function*, Radiology **255**, 2010, pp. 225-232.

[Bat05] Batz M., Baeßler S., Heil W., Otten W., Rudersdorf D., Schmiedeskamp J., Sobolev Y., Wolf M., *^{3}He Spin Filter for Neutrons*, Journal of Research of the National Institute of Standards and Technology **110**, 2005, pp. 293-298.

[Bat11a] Batz M., Nacher P.-J., Tastevin G., *Fundamentals of metastability exchange optical pumping in helium*, Journal of Physics: Conference Series **294**, 2011, pp. 012002.

[Bat11b] Batz M., *Metastability exchange optical pumping of ^{3}He gas up to 30mT: Efficiency measurements and evidence of laser-induced nuclear relaxation*, Dissertation zur Erlangung des Grades Doktor der Naturwissenschaften am Fachbereich Physik der Johannes Gutenberg-Universität in Mainz, 2011, available online at http://tel.archives-ouvertes.fr and http://archimed.uni-mainz.de from October 2011 on.

[Bec94] Becker J., Heil W., Krug B., Leduc M., Meyerhoff M., Nacher P.J., Otten E.W., Prokscha Th., Schearer L.D., Surkau R., *Study of mechanical compression of spin-polarized ^{3}He gas*, Nuclear Instruments and Methods in Physics Research A **346**, 1994, pp. 45-51.

[Bec98] Becker J., Bermuth J., Grossmann T., Heil W., Hofmann D., Leduc M., Otten E.W., Rohe D., Surkau R., *Interdisciplinary experiments with polarized He-3*, Nuclear Instruments and Methods in Physics Research A **402**, 1998, pp. 327-336.

[Bec99] Becker J., Andresen H.G., Annand J.R.M., Aulenbacher K., Beuchel K., Blume-Werry J., Dombo T., Drescher P., Ebert M., Eyl D., Frey A., Grabmayr P., Grossmann T., Hartmann P., Hehl T., Heil W., Herberg C., Hoffmann J., Kellie J.D., Klein F., Livingston K., Leduc M., Meyerhoff M., Moller H., Nachtigall C., Natter A., Ostrick M., Otten E.W., Owens R.O., Plutzer S., Reichert E., Rohe D., Schafer M., Schmieden H., Sprengard R., Steigerwald T., Steffens K.H., Surkau R., Walcher T., Watson R., Wilms E., *Determination of the neutron electric form factor from the reaction He-3(e,e'n) at medium momentum transfer*, The European Physical Journal A **6**, 1999, pp. 329-344.

[Bee03] Van Beek E.J.R., Schmiedeskamp J., Wild J.M., Paley M.N.J., Filbir F., Fichele S., Knitz F., Mills G.H., Woodhouse N., Swift A., Heil W., Wolf M., Otten E., *Hyperpolarized 3-helium MR imaging of the lungs: testing the concept of a central production facility*, European Radiology **13**, 2003, pp. 2583-2586.

[Bee04] Van Beek E.J., Wild J.M., Kauczor H.U., Schreiber W., Mugler J.P. 3rd, de Lange E.E., *Functional MRI of the Lung Using Hyperpolarized 3-Helium Gas*, Journal of Magnetic Resonance Imaging **20**, 2004, pp. 540-554.

[Big92] Bigelow N.P., Nacher P.J., Leduc M., *Accurate optical measurement of nuclear polarization in optically pumped ^{3}He gas*, Journal de physique II **2**, 1992, pp. 2159-2179.

[Bou60] Bouchiat M.A., Carver T.R., Varnum C.M., *Nuclear polarization in He^3 gas induced by optical pumping and dipolar exchange*, Physical Review Letters **5**, 1960, pp. 373-375.

[Cho03] Choukeife J., Maitre X., Nacher P.J., Tastevin G., *On-site production of hyperpolarized helium-3 gas for lung MRI*, Proceedings of the 11th ISMRM Scientific Meeting & Exhibition, July 10–16, 2003, Toronto, Canada, Abstract ISSN 1524-6965, pp. 1391.

[Cho09] Cho A., *Physics. Helium-3 shortage could put freeze on low-temperature research*, Science **326**, 2009, pp. 778-779.

[Col63] Colegrove F.D., Schearer L.D., Walters G.K., *Polarization of He^3 by optical pumping*, Physical Review **132**, 1963, pp. 2561-2572.

[Col10] Collier G., Nikiel G., Palasz T., Suchanek M., Glowacz B., Wojna A., Olejniczak Z., Dohnalik T., *Metastability Exchange Optical Pumping of ^{3}He at 1.5 T for an in-situ polariser*, Poster presented in JCNS Workshop on Modern Trends in Production and Applications of Polarized ^{3}He, 2010, Munich, available online: http://flux.if.uj.edu.pl/posters/Munich2010.pdf.

[Con97] Constantinesco A., Choquet P., Wioland M., Leduc M., Nacher P.J., Tastevin G., *L'IRM des gaz rares hyperpolarisés: une concurence future pour la médecine nucléaire ?*, Médecine nucléaire **21**, 1997, pp. 285-292.

[Cou01] Courtade E., *Pompage optique de l'hélium dans des conditions non-standard*, Dissertation to get the grade of Docteur en science de l'université Paris XI, Orsay, 2001, available online at http://tel.archives-ouvertes.fr/tel-00001447.

[Cou02] Courtade E., Marion F., Nacher P.J., Tastevin G., Kiersnowski K., Dohnalik T., *Magnetic field effects on the 1083 nm atomic line of helium*, The European Physical Journal D **21**, 2002, pp. 25-55.

[Den06] Deninger A., Heil W., Otten E.W., Wolf M., Kremer R.K., Simon A., *Paramagnetic relaxation of spin polarized* ^{3}He *at coated glass walls*, The European Physical Journal D **38**, 2006, pp. 439-443.

[Doh11a] Dohnalik T., Nikiel A., Palasz T., Suchanek M., Collier G., Grenczuk M., Glowacz B., Olejniczak Z., *Optimization of the pumping laser beam spatial profile in the MEOP experiment performed at elevated* ^{3}He *pressures*, The European Physical Journal Applied-Physics **54**, 2011, pp. 20802.

[Doh11b] Dohnalik T., Nikiel A., Palasz T., Suchanek M., Collier G., Grenczuk M., Glowacz B., Olejniczak Z., *Optimization of MEOP experiment performed at elevated* ^{3}He *pressures*, Europhysicnews **42/3**, 2011, pp. 12.

[Dri07] Driehuys B., Walker J., Pollaro J., Cofer G.P., Mistry N., Schwartz D., Johnson G.A., ^{3}He *MRI in Mouse Models of Asthma*, Magnetic Resonance in Medicine **58**, 2007, pp. 893-900.

[Dup71] Dupont-Roc J., Leduc M., Laloë F., *New value for the Metastability Exchange Cross Section in Helium,* Physical Review Letters **27**, 1971, pp. 467-470.

[Ebe96] Ebert M., Grossmann T., Heil W., Otten E.W., Surkau R., Thelen M., Leduc M., Bachert P., Knopp M.V., Schad L.R., *Nuclear magnetic resonance imaging with hyperpolarized helium-3,* The Lancet **347**, 1996, pp. 1297-1299.

[Eck92] Eckert G., Heil W., Meyerhoff M., Otten E.W., Surkau R., Werner M., Leduc M., Nacher P.J., Schearer L.D., *A dense polarized* ^{3}He *target based on compression of optically pumped gas*, Nuclear Instruments and Methods A **32**, 1992, pp. 53-65.

[Fal96] Mac Fall J.R., Charles H.C., Black R.D., Middleton H., Swartz J.C., Saam B., Erickson C., Happer W., Cates G.D., Johnson G.A., Ravin C.E., *Human lung air spaces: potential for MR imaging with hyperpolarized He-3,* Radiology **200**, 1996, pp. 553-558.

[Gas03] Gast K.K., Puderbach M.U., Rodriguez I., Eberle B., Markstaller K., Knitz F., Schmiedeskamp J., Weiler N., Schreiber W.G., Mayer E., Thelen M., Kauczor H.U., *Distribution of ventilation in lung transplant recipients: evaluation by dynamic* ^{3}He*-MRI with lung motion correction*, Investigative Radiology **38**, 2003, pp. 341-348.

[Gen93] Gentile T.R., McKeown R.D., *Spin-Polarizing* ^{3}He *nuclei with an arc-lamp-pumped neodymium-doped lanthanum magnesium hexaluminate laser*, Physical Review A **47**, 1993, pp. 456-467.

[Gen01] Gentile T.R., Rich D.R., Thomson A.K., Snow W.M., Jones G.L., *Compressing Spin-Polarized* ^{3}He *with a Modified Diaphragm Pump*, Journal of Research of the National Institute of Standards and Technology **106**, 2001, pp. 709-729.

[Gen03] Gentile T.R., Hayden M.E., Barlow M.J., *Comparison of metastability-exchange optical pumping sources*, Journal of the Optical Society of America B **20**, 2003, pp. 2068-2074.

[Glo11] Glowacz B., *Detection of metastable* He^{*}_{2} *molecules in helium plasma*, Dissertation to get the grade of Doctor in physics in Jagiellonian University of Krakow and in Université Paris VI of Paris, 2011.

[Her08] Hersman F.W., Ruset C.R., Ketel S., Muradian I., Covrig S.D., DIstelbrink J., Porter W., Watt D., Ketel J., Brackett J., Hope A., Patz S., *Large production system for hyperpolarized ^{129}Xe for human lung imaging studies*, Academic Radiology **15**, 2008, pp. 683-692.

[Hie10] Hiebel S., Großmann T., Kiselev D., Schmiedeskamp J., Gusev Y., Heil W., Karpuk S., Krimmer J., Otten E.W., Salhi Z., *Magnetized boxes for housing polarized spins in homogeneous fields*, Journal of Magnetic Resonance **204**, 2010, pp. 37-49.

[Hus05] Hussey D.S., Rich D.R., Belov A.S., Tong X., Yang H., Bailey C., Keith C.D., Hartfield J., Hall G.D.R., Black T.C., Snow W.M., Gentile T.R., Chen W.C., Jones G.L., Wildman E., *Polarized ^{3}He gas compression system using metastability-exchange optical pumping*, Review of Scientific Instruments **76**, 2005, pp. 053503.

[Hut11] Hutanu V., Meven M., Masalovich S., Heger G., Roth G., *3He spin filters for spherical neutron polarimetry at the hot neutrons single crystal diffractometer POLI-HEiDi*, Journal of Physics: Conference Series **294**, 2011, pp. 012012.

[Ire07] Ireland R.H., Btagg C.M., Mc Jury M., Woodhouse N., Fichele S., van Beek E.J.R., Wild J., Hatton M.Q., *Feasibility of image registration and intensity-modulated radiotherapy planning with hyperpolarized helium-3 magnetic resonance imaging for non-small-cell lung cancer*, International Journal of Radiation Oncology*Biology*Physics **68**, 2007, pp. 273-281.

[Iof11] Ioffe A., Babcock E., Pipich V., Radulescu A., *Wide-angle polarization analysis with ^{3}He for neutron scattering instrumentation at the JCNS*, Journal of Physics: Conference Series **294**, 2011, pp. 012013.

[Jon00] Jones G.L., Gentile T., Thompson A.K., Chowdhuri Z., Dewey M.S., Snow W.M., Wietfeldt F.E., *Test of ^{3}He based neutron polarizers at NIST*, Nuclear Instruments and Methods in Physics Research A **440**, 2000, pp. 772-776.

[Kas50] Kastler A., *Quelques suggestions concernant la production et la détection optique d'une inégalité de population des niveaux de quantification spatiale des atomes. Application à l'expérience de Stern et Gerlach et à la resonance magnétique*, Le Journal de hysique et le Radium **11**, 1950, pp. 255-265.

[Kau09] Kauczor H.U., *MRI of the lung*, Springer, Heidelberg 2009, pp. 36-56.

[Kob99] Kober F., Koenigsberg B., Belle V., Viallon M., Leviel J.L., Delon A., Ziegler A., Décorps M., Journal of Magnetic Resonance **138**, 1999, pp. 308-312.

[Kou05] Koumellis P., van Beek E.J., Woodhouse N., Fichele S., Swift A.J., Paley M.N., Taylor C.J., Wild J.M., *Quantitative analysis of regional airways obstruction using dynamic hyperpolarized ^{3}He MRI-preliminary results in children with cystic fibrosis*, Journal of Magnetic Resonance Imaging **22**, 2005, pp. 420-426.

[Kri11] Krimmer J., Heil W., Karpuk S., Otten E.W., Salhi Z., *Polarized ^{3}He targets in medium energy physics at MAMI*, Journal of Physics: Conference Series **294**, 2011, pp. 012015.

[Lar91] Larat C., *Laser LNA de puissance ; Application au pompage optique de l'hélium-3 et des mélanges hélium-3/hélium-4*, Dissertation to get the grade of Docteur en science de l'université Paris VI, Paris, 1991, available online at http://tel.archives-ouvertes.fr/tel-00011879.

[Lee06] Lee R.F., Johnson G., Grossman R.I., Stoeckel B., Trampel R., McGuinness G., *Advantages of Parallel Imaging in Conjunction With Hyperpolarized Helium-A New Approach to MRI of the Lung*, Magnetic Resonance in Medicine **55**, 2006, pp. 1132-1141.

[Lor93] Lorenzon W., Gentile T.R., Gao H., McKeown R.D., *NMR calibration of optical measurement of nuclear polarization in ^{3}He*, Physical Review A **47**, 1993, pp. 468-479.

[McL54] McLeod J.H., *The Axicon: A New Type of Optical Element*, Journal of the Optical Society of America **44**, 1954, pp. 592-592.

[Mey94] Meyerhoff M., Eyl D., Frey A., Andresen H.G., Annand J.R.M., Aulenbacher K., Becker J., Blume-Werry J., Dombo T., Drescher P., Ducret J.E., Fischer H., Grabmayr P., Hall S., Hartmann P., Hehl T., Heil W., Hoffmann J., Kellie J.D., Klein F., Leduc M., Möller H., Nachtigall C., Nachtigall C., Ostrick M., Otten E.W., Owens R.O., Plützer S., Reichert E., Rohe D., Schäfer M., Schearer L.D., Schmieden H., Steffens K.H., Surkau R., Walcher T., *First measurement of the electric formfactor of the neutron in the exclusive quasielastic scattering ofp olarized electrons from polarized ^{3}He*, Physics Letters B **327**, 1994, pp. 201-207.

[Mor97] Moreau O., Cheron B., Gilles H., Hamel J., Noël E., *Magnétomètre à ^{3}He pompé par diode laser = Laser diode pumped ^{3}He magnetometer*, Journal de physique III **7**, 1997, pp. 99-115.

[Mue01] Mueller R.M., *The Yb fiber laser for metastable ^{3}He optical pumping at Jülich*, Physica B **297**, 2001, pp. 277-281.

[Nac85] Nacher P.J., Leduc M., *Optical pumping in ^{3}He with a laser*, Journal de Physique **46**, 1985, pp. 2057-2073.

[Nac99] Nacher P.J., Tastevin G., Maitre X., Dollat X., Lemaire B., Olejnik B., *A peristaltic compressor for hyperpolarized helium*, European Radiology **9**, 1999, pp. B18.

[Nac02] Nacher P.J., Courtade E., Abboud M., Sinatra A., Tastevin G., *Optical pumping of helium-3 at high pressure and magnetic field*, Acta physica polonica B **33**, 2002, pp. 2225-2235.

[Nac03] Nacher P.J., *Peristaltic compressors suitable for relaxation-free compression of polarized gas*, United State patent n°US6655931B2, 2003.

[New93] Newbury N.R., Barton A.S., Cates G.D., Happer W., Middleton H., *Gaseous ^{3}He-^{3}He magnetic dipolar spin relaxation*, Physical Review A **48**, 1993, pp. 4411-4420.

[Nik07] Nikiel A., Palasz T., Suchanek M., Abboud M., Sinatra A., Olejniczak Z., Dohnalik T., Tastevin G., Nacher P.J., *Metastability exchange optical pumping of ^{3}He at high pressure and high magnetic field for medical applications*, The European Physical Journal Special Topics **144**, 2007, pp. 255-263.

[Nik10] Nikel A., *Polaryzacja ^{3}He w warunkach rozerwania sprzezenia struktury nadzubtelnej*, Dissertation to get the grade of Doctor in physics in Jagiellonian University of Krakow, 2010.

[Nik11] Nikel A., Collier G., Glowacz B., Palasz T., Suchanek M., Olejniczak Z., Tastevin G., Nacher P.J., Dohnalik T., *Metastability exchange optical pumping of ^{3}He at elevated pressure at 4.7 T*, in preparation (2011).

[Rab07] Rabe K.F., Hurd S., Barnes P.J., Buist S.A., Calverley P., Fukuchi Y., Jenkins C., Rodriguez-Roisin R., van Weel C., Zielinski J., *Global strategy for the diagnosis,* *management, and prevention of chronic obstructive pulmonary disease: GOLD executive summary*, American Journal of Respiratory and Critical Care Medicine **176**, 2007, pp. 532-555.

[Saa95] Saam B., Happer W., Middletown H., *Nuclear relaxation of 3He in the presence of* O_2, Physical review A **52**, 1995, pp. 862-865.

[Sch69] Schearer L.D., *Ion polarization via Penning collisions with optically pumped metastable helium*, Physical Review Letters **22**, 1969, pp. 629-631.

[Sch06a] Schmiedeskamp J., Heil W., Otten E.W., Kremer R.K., Simon A., Zimmer J., *Paramagnetic relaxation of spin polarized* ^{3}*He at bare glass surfaces*, The European Physical Journal D **38**, 2006, pp. 427-438.

[Sch06b] Schmiedeskamp J., Elmers H.J., Heil W., Otten E.W., Sobolev Y., Kilian W., Rinneberg H., Sander-Thömmes T., Seifert F., Zimmer J., *Relaxation of spin polarized* ^{3}*He by magnetized ferromagnetic contaminants*, The European Physical Journal D **38**, 2006, pp. 445-454.

[Sto96a] Stoltz E., Villard B., Meyerhoff M., Nacher P.J., *Polarization analysis of the light emitted by an optically pumped* ^{3}*He gas*, Applied Physics B **63**, 1996, pp. 635-640.

[Sto96b] Stoltz E., Meyerhoff M., Bigelow N., Leduc M., Nacher P.J., Tastevin G., *High nuclear polarization in* ^{3}*He and* ^{3}*He-*^{4}*He gas mixtures by optical pumping with a laser diode*, Applied Physics B **63**, 1996, pp. 629-633.

[Suc05a] Suchanek K., Cieslar K., Olejniczak Z., Palasz T., Suchanek M., Dohnalik T., *Hyperpolarized* ^{3}*He gas production by metastability exchange optical pumping for magnetic resonance imaging*, Optica Applicata **35**, 2005, pp. 263-276.

[Suc05b] Suchanek M., Cieslar K., Palasz T., Suchanek K., Dohnalik T., *Magnetic Resonance Imaging at low magnetic field using hyperpolarized* ^{3}*He gas*, Acta Physica Polonica A **107**, 2005, pp. 491-506.

[Suc07] Suchanek K., Suchanek M., Nikiel A., Palasz T., Abboud M., Sinatra A., Nacher P.J., Tastevin G., Olejniczak Z., Dohnalik T., *Optical measurement of* ^{3}*He nuclear polarization for metastable exchange optical pumping studies at high magnetic field*, The European Physics Journal Special Topics **144**, 2007, pp. 67-74.

[Sur97] Surkau R., Becker J., Ebert M., Grossmann T., Heil W., Hofmann D., Humblot H., Leduc M., Otten E.W., Rohe D., Siemensmeyer K., Steiner M., Tasset F., Trautmann N., *Realization of a broad band neutron spin filter with compressed, polarized* ^{3}*He gas*, Nuclear Instruments and Methods in Physics Research A **384**, 1997, pp. 444-450.

[Swi05] Swift A.J., Wild J.M., Fichele S., Woodhouse N., Fleming S., Waterhouse J., Lawson R.A., Paley M.N., van Beek E.J., *Emphysematous changes and normal variation in smokers and COPD patients using diffusion* ^{3}*He MRI*, European Journal of Radiology **54**, 2005, pp. 352-358.

[Tal11] Talbot C., Batz M., Nacher P.J., Tastevin G., *An accurate optical technique for measuring the nuclear polarisation of* ^{3}*He gas*, Journal of Physics: Conference Series **294**, 2011, pp. 012008.

[Tas04] Tastevin G., Grot S., Courtade E., Bordais S., Nacher P.J., *A broadband ytterbium-doped tunable fiber laser for* ^{3}*He optical pumping at 1083 nm*, Applied Physics B **78**, 2004, pp. 145-156.

[Tas05] Tastevin G., Nacher P.J., *NMR measurements of hyperpolarized ^{3}He gas diffusion in high porosity silica aerogels*, The Jounal of Chemical Physics **123**, 2005, pp. 064506.

[Thi07] Thiel T., Schnabel A., Knappe-Grüneberg S., Stollfuß D., Burghoff M., *Demagnetization of magnetically shielded rooms*, Review of Scientific Instruments **78**, 2007, pp. 035106.

[Via99] Viallon M., Cofer G.P., Suddarth S.A., Möller H.E., Chen X.J., Chawla M.S., Hedlund L.W., Cremillieux Y., Johnson G.A., *Functional MR microscopy of the lung using hyperpolarized ^{3}He*, Magnetic Resonance in Medicine **41**, 1999, pp. 787-792.

[Vig03] Vignaud A., *Influence de l'intensité du champ magnétique sur l'imagerie RMN des poumons à l'aide d'hélium-3 hyperpolarisé*, Dissertation to get the grade of Docteur en science de l'université Paris XI, Orsay, 2003, pp. 85, available online at http://tel.archives-ouvertes.fr/tel-00003668/en/.

[Wal62] Walters G.K., Colegrove F.D., Schearer L.D., *Nuclear polarization of He^3 gas by metastability exchange with optically pumped metastable He^3 atoms*, Physical Review Letters **9**, 1962, pp. 439-442.

[Wal97] Walker T.G., Happer W., *Spin-exchange optical pumping of noble-gas nuclei*, Reviews of Modern Physics **69**, 1997, pp. 629-642.

[Wal11] Walker T.G., *Fundamentals of Spin-Exchange Optical Pumping*, Journal of Physics: Conference Series **294**, 2011, pp. 012001.

[Wil97] Wilms E., Ebert M., Heil W., Surkau R., *Polarimetry on dense samples of spin-polarized ^{3}He by magnetostatic detection*, Nuclear Instruments and Methods in Physics Research A **401**, 1997, p. 491-498.

[Wol04] Wolf M., *Highest He-3 nuclear spin polarization production by metastable exchange pumping*, Dissertation zur Erlangung des Grades Doktor der Naturwissenschaften am Fachbereich Physik der Johannes Gutenberg-Universität in Mainz, 2004, available online at http://ubm.opus.hbz-mrw.de/volltexte/2005/655/.